

**INTERPOLATION AND EXTRAPOLATION
OF SCATTERING RESULTS OF A
CANONICAL GEOMETRY**

A THESIS

SUBMITTED TO THE DEPARTMENT OF ELECTRICAL AND

ELECTRONICS ENGINEERING

AND THE INSTITUTE OF ENGINEERING AND SCIENCES

OF BILKENT UNIVERSITY

IN PARTIAL FULFILLMENT OF THE REQUIREMENTS

FOR THE DEGREE OF

MASTER OF SCIENCE

By

Mehmet R. Geden

May 2002

I certify that I have read this thesis and that in my opinion it is fully adequate, in scope and in quality, as a thesis for the degree of Master of Science.

Dr. Levent Gürel(Supervisor)

I certify that I have read this thesis and that in my opinion it is fully adequate, in scope and in quality, as a thesis for the degree of Master of Science.

Prof. Dr. Ayhan Altıntaş

I certify that I have read this thesis and that in my opinion it is fully adequate, in scope and in quality, as a thesis for the degree of Master of Science.

Assoc.Prof. Orhan Arıkan

I certify that I have read this thesis and that in my opinion it is fully adequate, in scope and in quality, as a thesis for the degree of Master of Science.

Asst.Prof. Vakur B. Ertürk

Approved for the Institute of Engineering and Sciences:

Prof. Dr. Mehmet Baray
Director of Institute of Engineering and Sciences

ABSTRACT

INTERPOLATION AND EXTRAPOLATION OF SCATTERING RESULTS OF A CANONICAL GEOMETRY

Mehmet R. Geden

M.S. in Electrical and Electronics Engineering

Supervisor: Dr. Levent Gürel

May 2002

It is well-known that calculation of scattered fields at high frequencies is consuming too much CPU time and memory allocation. The exponential model is used to predict the high frequency values in the radar cross section (RCS) calculation. The Prony's and Matrix-Pencil methods are presented to extract the parameters of exponential model. In particular, the Matrix-Pencil method is modified to increase the efficiency. Both methods are applied to a reference scatterer (a perfect electrically conducting sphere). Also, a new modelling scheme is proposed using the Legendre-basis functions. This approach is tested in the calculation of the bistatic RCS values.

Keywords: Matrix-Pencil method, RCS, extrapolation

ÖZET

KURALSAL BİR GEOMETRİNİN SAÇINIM SONUÇLARININ İTERPOLASYON VE EKSTRAPOLASYONU

Mehmet R. Geden

Elektrik ve Elektronik Mühendisliği Bölümü Yüksek Lisans

Tez Yöneticisi: Dr.Levent Gürel

Mayıs 2002

Saçınım alanların hesaplamalarının çok fazla bilgisayar süresini ve hafızasını meşgul ettiği bilinen bir gerçektir. Bu tezde, üstel fonksiyonlar kullanılarak yüksek frekanslarda radar kesit alanı (RKA) modellenmiştir. Prony ve Matris-Pencil yöntemleri kullanılarak üstel modelin parametreleri hesaplanmıştır. Özel olarak, Matris-Pencil yeterliliğini arttırmak için in değişiklikler yapılmıştır. Her iki yöntemde saçınım çözümlerinde referans kabul edilebilecek bir cisme (tam iletken bir küreye) tatbik edilmiştir. Üstel yöntemlerden farklı olarak Legendre fonksiyonların baz olarak kullanıldığı yeni bir yöntemde önerilmiştir. Bu yöntem bistatik RKA hesaplamalarında test edilmiştir.

Anahtar kelimeler: Matris-Pencil, RKA, açılal ekstrapolasyon.

ACKNOWLEDGMENTS

I gratefully thank my supervisor Dr. Levent Gürel for his supervision, guidance, and suggestions throughout the development of this thesis.

I would like to thank Dr. Orhan Arıkan and Prof. M.İrşadi Aksun for their helpful suggestions on my thesis.

Contents

1	Introduction	1
2	Scattering by a Conducting Sphere	5
2.1	Scattered Electric Field Solutions	5
2.2	Far-Field Observations	11
2.3	Radar Cross Section	13
2.4	Choice of the Number of Terms in Series Summation	15
2.5	Calculation of RCS by Using Scattered Electric Fields	16
2.6	Induced Current Distribution of the PEC Sphere	18
3	Prony's Method	23
3.1	Simultaneous Exponential Parameter Estimation	24
3.2	Original Prony Concept	26
3.3	Least-Squares Prony's Method	28
3.4	Application of Prony's Method	31

4	Matrix-Pencil Method	37
4.1	Relation between the Prony's and Matrix-Pencil Method	41
4.2	Applications of the Matrix-Pencil Method	44
4.2.1	Natural Matrix-Pencil Method	44
4.2.2	Choice of the Parameters in the Matrix-Pencil Method . . .	53
4.2.3	Elimination of the Growing Exponentials	54
4.2.4	Generation of the Residues with the New Set of Exponentials	56
5	Multi-Scale Matrix-Pencil Method	58
5.1	Employing E_{θ}^s, E_{ϕ}^s Components in the RCS Estimation	63
5.2	Application of Multi-Scale Matrix-Pencil Method to E_{θ}^s, E_{ϕ}^s Com- ponents	65
5.3	Matrix-Pencil Method with Asymptotic RCS Values	68
5.4	Applications of the Matrix-Pencil Method to Surface Currents . . .	71
5.5	Comparisons with Other Extrapolation Techniques	76
6	Angular Extrapolation of the Induced Currents	78
6.1	Calculation of RCS with the Integration of the Surface Currents . .	84
7	Conclusions	93
A	Appendix	95
A.1	Singular Value Decomposition	95

A.2 Legendre Polynomials	97
A.3 Derivative Operator of Spherical Bessel and Hankel Functions . . .	99
A.4 Projections and Least Square Solution	100
A.5 Composite Simpson's Double Integral	102

List of Figures

1.1	Modeling an RCS signal $x[k]$ as the response of a linear shift invariant filter to an input $v[k]$. The goal is to find the $H(z)$ coefficients that make $\hat{x}[k]$ as close as possible to $x[k]$	2
2.1	Uniform plane wave incident on a conducting sphere	6
2.2	The number of series is shown between $a/\lambda = 0$ and $a/\lambda = 2$. $[0, 2]$ interval is divided 100 points with sampling period $T_s = 0.02$	15
2.3	Normalized radar cross section for a conducting sphere as a function of its radius ($\theta = \pi, \phi = \phi$).	16
2.4	Normalized monostatic radar cross section for a conducting sphere as a function of its radius. The RCS values are plotted in the logarithmic scale.	17
2.5	Induced current distribution on the surface of the sphere. The radius of the sphere $a = \lambda/2$. The resultant surface current is calculated ($\mathbf{J} = (J_\theta ^2 + J_\phi ^2)^{1/2}$)	20
2.6	Induced current distribution of the sphere when the radius (a) is equal to 2λ . The resultant surface current is calculated ($\mathbf{J} = (J_\theta ^2 + J_\phi ^2)^{1/2}$)	21

2.7	Induced current distribution when $a = 10\lambda$. The dark and light region can be seen easily. The magnitude of the resultant current is calculated. $ \mathbf{J} = (J_\theta ^2 + J_\phi ^2)^{1/2}$	21
2.8	Induced Surface Current Distributions at $a = 10\lambda, J_\theta $ and $ J_\phi $ and its phases. The plot curves, 181×361 sampled matrix is used on the surface of the sphere	22
3.1	Application of the Prony's method to monostatic RCS results $M = 7, N = 100, T_s = 0.02$, Samples are taken from the interval= $[0.02, 2]$	31
3.2	Application of the Prony's method to monostatic RCS results. The number of exponentials is increased to $M = 10$	32
3.3	Application of the Prony's Method to monostatic RCS results $M = 15, N = 100, T_s = 0.02$, Sampling interval= $[0.02, 2]$	33
3.4	Application of the Prony's method to monostatic RCS results $M = 20, N = 100, T_s = 0.02$, Sampling interval= $[0.02, 2]$	34
3.5	The maximum number of exponentials are used in the Prony's Method. $M = \max(49), N = 100, T_s = 0.02$, Sampling interval= $[0.02, 2]$	35
3.6	Extrapolation of RCS values in the frequency dimension. The parameters are solved with Prony's method. $M = 15, N = 80, T_s = 0.02$, Sampling interval= $[0.02, 1.6]$	36
4.1	Application of the Matrix-Pencil method to monostatic RCS results $M = 15, N = 100, T_s = 0.02$, Sampling interval= $[0.02, 2]$	44

4.2	Extrapolation of the monostatic RCS values with Matrix-Pencil method. $M = 15$, $N = 80$, $T_s = 0.02$, Sampling interval= $[0.02, 1.6]$. Extrapolation is performed until $a/\lambda = 2$. . .	45
4.3	Extrapolation of the monostatic RCS values with using less sampled data. The number of exponentials (M) is still 15, $N = 41$, $T_s = 0.02$, Sampling interval= $[0.02, 1.2]$	46
4.4	Application of the Matrix-Pencil Method to monostatic RCS results $M = 20$, $N = 41$, $T_s = 0.02$, Sampling interval= $[0.02, 1.2]$. .	47
4.5	The extrapolation is extended up to $a/\lambda = 10$. Application of the Matrix-Pencil Method to monostatic RCS results $M = 20$, $N = 41$, $T_s = 0.02$, Sampling interval= $[0.02, 1.6]$	48
4.6	The error values are shown at the bottom plot with logarithmic scale. Application of the Matrix-Pencil Method to monostatic RCS results $M = 20$, $N = 81$, $T_s = 0.02$, Sampling interval= $[0.4, 1.6]$	49
4.7	Application of the Matrix-Pencil Method to monostatic RCS results $M = 35$, $N = 81$, $T_s = 0.02$, Sampling interval= $[0.4, 1.6]$. . .	50
4.8	The maximum number of exponentials is used ($M = 40$). Application of the Matrix-Pencil Method to monostatic RCS results , $N = 80$, $T_s = 0.02$, Sampling interval= $[0.02, 1.6]$	51
4.9	Flowchart of the Matrix-Pencil algorithm.	53
4.10	Growing exponentials present in Fig. 4.7 are plotted separately. . .	55
4.11	The elimination of the growing exponentials from monostatic RCS results with $M = 35$, $N = 81$, $T_s = 0.02$ and sampling interval= $[0.4, 2]$	56

4.12	Generation of the residues with the new set of exponentials with $M = 40, N = 81, T_s = 0.02$ and sampling interval= $[0.4, 2]$	57
4.13	Flowchart of the elimination of the growing exponentials.	57
5.1	Sampling procedure of the Multi-scale GPOF	58
5.2	Flowchart of the Multi-scale GPOF	60
5.3	Multi-scale Matrix-Pencil Method with RCS values $M = 40, N = 61, T_s = 0.02$, Sampling interval= $[0.4, 2]$	62
5.4	Employing E_θ^s, E_ϕ^s Components in the RCS Estimation $M = 15, N = 41, T_s = 0.04$, Sampling interval= $[0.4, 2]$	64
5.5	Employing E_θ^s, E_ϕ^s Components in the RCS Estimation $M = 40, N = 81, T_s = 0.02$, Sampling interval= $[0.4, 2]$	65
5.6	Employing E_θ^s, E_ϕ^s Components in the RCS Estimation also the Growing exponentials are eliminated $M = 40, N = 81, T_s = 0.02$, Sampling interval= $[0.4, 2]$	66
5.7	Synthesized Flowchart of the Multi-scale Matrix-Pencil method	67
5.8	Employing E_θ^s, E_ϕ^s Components in the RCS Estimation also the Multi-Scale Matrix-Pencil Algorithm is used $M = 40, N = 61, T_s = 0.02$, Sampling interval= $[0.4, 1.2]$, $T_s = 0.04$, Sampling interval= $[0.4, 2]$	68
5.9	The integration of Asymptotic values with the Matrix-Pencil Method	69
5.10	The integration of imaginary Asymptotic values with the Matrix-Pencil Method	70

5.11	Prediction of current value $\mathbf{J}(\theta_0, \phi_0)$ at frequency f_4 by using the lower frequency values $[\mathbf{J}(f_1, \theta_0, \phi_0), \mathbf{J}(f_2, \theta_0, \phi_0), \mathbf{J}(f_3, \theta_0, \phi_0)]$. . .	71
5.12	Applications of the Matrix-Pencil Method to Surface Current, the residues are generated with the eliminated set of exponentials ($\theta = 45^\circ, \phi = 0^\circ$) J_θ is sampled from $[0, 2]$, $M = 50$	72
5.13	Applications of the Matrix-Pencil Method to Surface Current, the residues are generated with the eliminated set of exponentials ($\theta = 90^\circ, \phi = 0^\circ$) J_θ is sampled from $[0, 2]$, $M = 50$	73
5.14	Applications of the Matrix-Pencil Method to Surface Current, the residues are generated with the eliminated set of exponentials ($\theta = 180^\circ, \phi = 0^\circ$) J_θ is sampled from $[0, 2]$, $M = 50$	74
5.15	Applications of the Matrix-Pencil Method to Surface Current, the residues are generated with the eliminated set of exponentials ($\theta = 45^\circ, \phi = 90^\circ$) J_ϕ is sampled from $[0, 2]$, $M = 50$	74
5.16	Applications of the Matrix-Pencil Method to Surface Current, the residues are generated with the eliminated set of exponentials ($\theta = 90^\circ, \phi = 90^\circ$) J_ϕ is sampled from $[0, 2]$, $M = 50$	75
6.1	The location of the unknown current values on the surface of the sphere	78
6.2	The open form of sphere surface lays along a flat plane. The variables which totally represents the sphere surface, θ, ϕ are taken as vertical and horizontal axis, respectively.	80
6.3	The Legendre-basis algorithm is applied to J_θ component of surface current when $a/\lambda = 2$, samples are taken from ($0^\circ \leq \theta \leq 6^\circ, 69^\circ \leq \theta \leq 180^\circ$) number of coefficients $M = 23$	81

6.4	The Legendre-basis algorithm is applied to J_θ component of surface current when $a/\lambda = 4$, samples are taken from ($0^\circ \leq \theta \leq 6^\circ$, $69^\circ \leq \theta \leq 180^\circ$) number of coefficients $M = 36$	82
6.5	The Legendre-basis algorithm is applied to J_ϕ component of surface current when $a/\lambda = 2$, samples are taken from ($0^\circ \leq \theta \leq 6^\circ$, $69^\circ \leq \theta \leq 180^\circ$) number of coefficients $M = 23$	83
6.6	The Legendre-basis algorithm is applied to J_ϕ component of surface current when $a/\lambda = 2$, samples are taken from ($0^\circ \leq \theta \leq 6^\circ$, $69^\circ \leq \theta \leq 180^\circ$) number of coefficients $M = 36$	84
6.7	An Arbitrary Electric Current Source	85
6.8	The location of the some intersection points on the PEC sphere .	89
6.9	3-D illustration of Current Estimation on the Surface of the sphere surface, θ, ϕ are taken as vertical and horizontal axis, respectively.	90
6.10	The monostatic ($\theta = \pi, \phi = \pi$) RCS calculations of the PEC sphere is illustrated. Before the integration of current values Legendre-basis algorithm is applied to J_θ and J_ϕ components of surface current by using the samples values which are taken ($0^\circ \leq \theta \leq 6^\circ, 69^\circ \leq \theta \leq 180^\circ$) at $\phi = 0$ and $\phi = 90^\circ$ cuts. The resolution of the plotted RCS figure is equal to 0.02.	91
6.11	The bistatic RCS calculations when the look angle ($\theta = \pi/3, \phi = \pi/6$) is illustrated. Before the integration of current values Legendre-basis algorithm is applied to J_θ and J_ϕ components of surface current by using the samples values which are taken ($0^\circ \leq \theta \leq 6^\circ, 69^\circ \leq \theta \leq 180^\circ$) at $\phi = 0$ and $\phi = 90^\circ$ cuts. The resolution of the plotted RCS figure is equal to 0.02.	92

A.1 Geometrical illustration of the least squares solution to an overdetermined set of linear equations. the best approximation to \mathbf{b} is formed when the error \mathbf{e} is orthogonal to to the vectors \mathbf{a}_1 and \mathbf{a}_2 101

List of Tables

3.1	Solution of the Exponents and Residues in the Exponential model with Prony's Method, Number of Exponents= 15 Number of samples= 40	35
4.1	Solution of the Matrix-Pencil method; exponents and residues $N = 81$, Interpolation region= $[0.4, 2]$, Extrapolation region= $[2, 10]$, Sampling period, $T_s = 0.02$	52

To My Family . . .

Chapter 1

Introduction

At high frequencies, calculation of radar cross section (RCS) values costs too much CPU time and memory allocation. As the electrical sizes of the problems get larger, numerical solution of the expressions become impossible.

The problem of uniform plane wave scattering by a conducting sphere is often used as a reference solution. In Chapter 2, the solution of this canonical geometry is presented. The analytical expressions of induced currents, far-zone scattered field components and RCS are also available in this chapter. Since the RCS signal is highly frequency dependent, one needs to do the calculation at finer increments of frequency to obtain an accurate representation of the frequency response. This can be computationally intensive and for electrically large objects it can be prohibitive despite the increased power of the present generation of computers.

In this thesis, a frequency extrapolation and interpolation scheme is investigated to predict scattered components using a model. To perform estimations of RCS signal values at high frequencies, at lower frequencies the RCS values are sampled with a sampling period T_s at N point. The sampled values can be denoted $x[k]$ where $k = 0, 1, \dots, N - 1$.

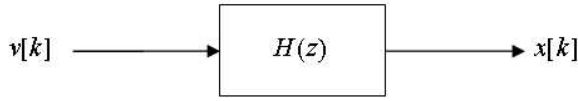


Figure 1.1: Modeling an RCS signal $x[k]$ as the response of a linear shift invariant filter to an input $v[k]$. The goal is to find the $H(z)$ coefficients that make $\hat{x}[k]$ as close as possible to $x[k]$.

Different type of models can be used to predict the signal values from its sample values, such as a rational function as shown in Fig. 1.1,

$$H(z) = \frac{\sum_{k=0}^q b_q(k)z^{-k}}{\sum_{k=0}^p a_p(k)z^{-k}},$$

where $b_q(k)$ and $a_p(k)$ are the coefficients of denominator and numerator, or a linear combination of exponentials

$$\hat{x}[k] = \sum_{i=1}^M R_i e^{[(\alpha_i + j\omega_i)kT_s]}, \quad (1.1)$$

where

$$\begin{aligned} \hat{x}[k] &: \text{the estimate of } x[k] \\ s_i &: \text{coefficient of the exponent} \\ R_i &: \text{Residue or complex coefficient} \\ T_s &: \text{Sampling period} \end{aligned} \quad (1.2)$$

or a sum of sinusoidal functions, etc. As a preliminary work of this thesis, the algorithms available in current literature to solve parameters of these models are used with sample values of RCS signal. For example, model-based parameter estimation (MBPE) [9] is used to determine the coefficients of rational function. From the signal processing area, the autocorrelation, the covariance, iterative pre-filtering and Burg's algorithms [12] are applied to RCS signal values. The MBPE is good at interpolation but the performance of the prediction at the extrapolation region does not satisfy the percentage error criteria of %1. These

methods are all used in the solution of the rational function coefficients. Also, there is a further comparison available at the end of Chapter 5.

According to the experience about the results of previous methods which are designed to solve the parameters of rational function, it is decided to use an exponential model rather than a rational function model. Once the form of the model has been selected, the next step is to find the model parameters that provide the best approximation to the given RCS signal. Briefly, the problem is to extract parameters of the exponential model from a set of sampled data. The exponential model parameters are extracted by using the Prony's [5] and the matrix-pencil [6] (often named as GPOF or generalized-pencil-of-function [3]) methods. Once the model parameters are determined, the frequency behavior of the RCS is extrapolated. The matrix-pencil algorithm is a general-purpose algorithm to represent arbitrary signals. However, RCS values have some specific features. By considering these features, the matrix-pencil method can be modified to estimate RCS at higher frequencies.

The other variables of the scattering problem, such as the induced currents on the surface of the sphere, are also intended to represent by a more convenient model rather than linear combination of exponential functions. The model is set up by using Legendre-Basis functions. Once the parameters of model is extracted from the sampled surface currents, current distribution can be determined all over the surface of the sphere. Furthermore, the calculation of RCS at an arbitrary angle (bistatic RCS) is possible by the integration of surface currents.

In Chapter 3, the Prony's method is presented to extract the parameters of exponential model. At the end of Chapter 3, the Prony's method is applied to the RCS signal. The matrix-pencil method is described in Chapter 4. Relationship between the Prony's and the matrix-pencil method and the applications to the RCS signal are also demonstrated in this chapter. Chapter 5, a new algorithm is proposed based on the matrix-pencil theory to estimate RCS signal values.

This algorithm can predict successfully the higher frequency RCS values with very modest sampled data and few exponentials. Also at the end of this chapter, the extrapolation of the induced currents in the frequency dimension is demonstrated.

In addition to the frequency dimension, calculation of the current on the surface of the sphere is also consuming too much CPU time and memory allocation. To reduce these bottlenecks, we have investigated a method to estimate the induced current values on the surface of the sphere. The basis functions of this method are consists of Legendre polynomials. In Chapter 6, we have proposed an efficient model to represent the induced currents on the surface of the PEC sphere. The coefficients of Legendre-basis functions are solved from the least squares problem. This model enables angular extrapolation of the induced currents all over the surface of the sphere from a few densely sampled data. Furthermore, calculation of bistatic RCS values accurately at an arbitrary look angle by integrating the set of induced current data, which are also estimated with few densely sampled induced currents, is demonstrated.

Chapter 2

Scattering by a Conducting Sphere

In scattering problems, a plane wave scattering by conducting sphere is often used as a reference scatterer to measure the scattering problem (such as the RCS) of the targets [1]. That's why the interpolation and extrapolation algorithms are applied to the RCS of a conducting sphere.

2.1 Scattered Electric Field Solutions

Let us assume that the electric field of a uniform plane wave is polarized in the x direction and it is travelling along the z -axis as shown in Figure 2.1. The electric field of the incident wave can be expressed as;

$$\mathbf{E}^i = \hat{a}_x E_x^i = \hat{a}_x E_o e^{-j\beta z} = \hat{a}_x E_o e^{-j\beta r \cos \theta} \quad (2.1)$$

where β is the propagation constant;

$$\beta = \frac{2\pi}{\lambda}.$$

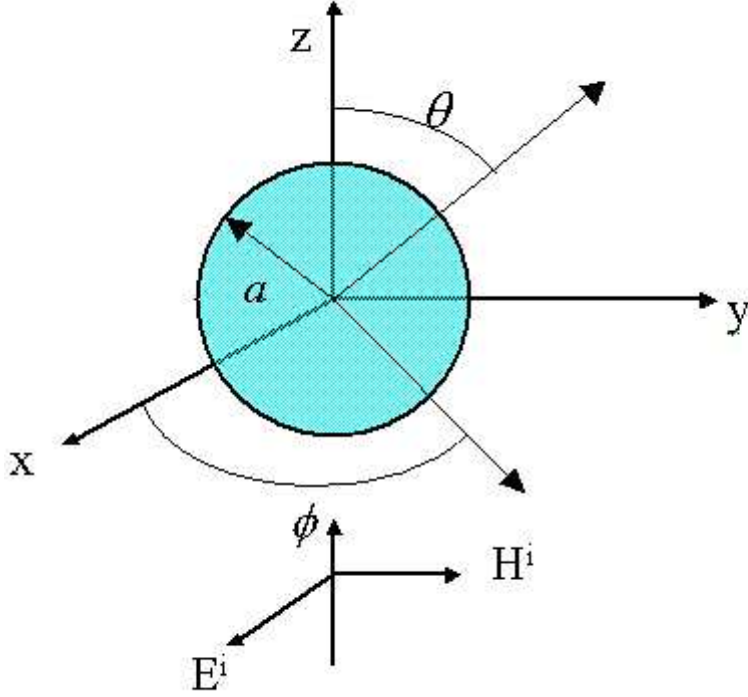


Figure 2.1: Uniform plane wave incident on a conducting sphere

Rectangular coordinate terms in Equation (2.1) can be transformed to spherical coordinates, as follows;

$$\mathbf{E}^i = \hat{a}_r E_r^i + \hat{a}_\theta E_\theta^i + \hat{a}_\phi E_\phi^i \quad (2.2)$$

where

$$E_r^i = E_x^i \sin \theta \cos \phi = E_o \sin \theta \cos \phi e^{-j\beta r \cos \theta} = E_o \frac{\cos \phi}{j\beta r} \frac{\partial}{\partial \theta} e^{-j\beta r \cos \theta} \quad (2.3a)$$

$$E_\theta^i = E_x^i \cos \theta \cos \phi = E_o \cos \theta \cos \phi e^{-j\beta r \cos \theta} \quad (2.3b)$$

$$E_\phi^i = -E_x^i \sin \phi = -E_o \sin \phi e^{-j\beta r \cos \theta} \quad (2.3c)$$

$$e^{-j\beta z} = e^{-j\beta r \cos \theta} = \sum_{n=0}^{\infty} a_n j_n(\beta r) P_n(\cos \theta) \quad (2.4)$$

$$a_n = j^{-n} (2n + 1)$$

We can rewrite the (2.3a) through (2.3c) using expansion in Eq. (2.4) of exponential function $e^{-j\beta z}$ with spherical Bessel and Legendre functions. We get

$$E_r^i = E_o \frac{\cos \phi}{j\beta r} \sum_{n=0}^{\infty} j^{-n} (2n+1) j_n(\beta r) \frac{\partial}{\partial \theta} [P_n(\cos \theta)] \quad (2.5a)$$

$$E_\theta^i = E_o \cos \phi \cos \theta \sum_{n=0}^{\infty} j^{-n} (2n+1) j_n(\beta r) P_n(\cos \theta) \quad (2.5b)$$

$$E_\phi^i = -E_o \sin \phi \sum_{n=0}^{\infty} j^{-n} (2n+1) j_n(\beta r) P_n(\cos \theta) \quad (2.5c)$$

Since spherical Bessel functions are replaced with special kind of spherical functions, the relation is

$$j_n = \frac{1}{\beta r} \hat{J}_n(\beta r) \quad (2.6)$$

and

$$\begin{aligned} \frac{\partial P_n}{\partial \theta} &= P_n^1(\cos \theta) \\ P_0^1 &= 0 \end{aligned} \quad (2.7)$$

we can write equation set 2.5 as

$$E_r^i = -j E_o \frac{\cos \phi}{(\beta r)^2} \sum_{n=1}^{\infty} j^{-n} (2n+1) \hat{J}_n(\beta r) [P_n^1(\cos \theta)] \quad (2.8a)$$

$$E_\theta^i = E_o \frac{\cos \phi \cos \theta}{\beta r} \sum_{n=0}^{\infty} j^{-n} (2n+1) \hat{J}_n(\beta r) [P_n^0(\cos \theta)] \quad (2.8b)$$

$$E_\phi^i = -E_o \frac{\sin \phi}{\beta r} \sum_{n=0}^{\infty} j^{-n} (2n+1) \hat{J}_n(\beta r) [P_n^0(\cos \theta)] \quad (2.8c)$$

The incident and scattered fields by the sphere can be expressed as a superposition of TE^r and TM^r where

$$\mathbf{E} = -\frac{1}{\varepsilon} \nabla \times \mathbf{F} + \frac{1}{j\omega\mu\varepsilon} \nabla \times \nabla \times \mathbf{A} \quad (2.9a)$$

$$\mathbf{H} = \frac{1}{j\omega\mu\varepsilon} \nabla \times \nabla \times \mathbf{F} + \frac{1}{\mu} \nabla \times \mathbf{A}. \quad (2.9b)$$

The TE^r fields are constructed by letting the vector potentials \mathbf{A} and \mathbf{F} equal to $\mathbf{A}=\mathbf{0}$ and $\mathbf{F} = \hat{a}_r F_r(r, \theta, \phi)$ in Eq. (2.9). The TM^r fields are constructed when $\mathbf{A} = \hat{a}_r A_r(r, \theta, \phi)$ and $\mathbf{F}=\mathbf{0}$. For example, the incident radial electric field component E_r^i can be obtained by expressing it in terms of TM^r modes or A_r^i . Thus using A_r^i we can write the incident electric field as

$$E_r^i = \frac{1}{j\omega\mu\varepsilon} \left(\frac{\partial^2}{\partial r^2} + \beta^2 \right) A_r^i \quad (2.10)$$

Equating (2.10) to (2.8a), A_r^i takes the form of

$$A_r^i = E_o \frac{\cos \phi}{\omega} \sum_{n=1}^{\infty} a_n \hat{J}_n(\beta r) [P_n^1(\cos \theta)] \quad (2.11)$$

where

$$a_n = j^{-n} \frac{(2n+1)}{n(n+1)} \quad (2.12)$$

This potential component A_r^i will give the correct value of E_r^i , and it will lead to $H_r^i = 0$.

The correct expression of the radial component of the incident magnetic field can be obtained by following a similar procedure but using TE^r modes or F_r^i . This allows us to show that

$$F_r^i = E_o \frac{\sin \phi}{\omega\eta} \sum_{n=1}^{\infty} a_n \hat{J}_n(\beta r) [P_n^1(\cos \theta)] \quad (2.13)$$

where a_n is given by (2.12). This expression leads to the correct H_r^i and to $E_r^i = 0$. Therefore the sum of (2.11) will give the correct E_r^i, H_r^i and the remaining electric and magnetic components.

Since the incident electric and magnetic field components of a uniform plane wave can be represented by TE^r and TM^r modes that can be constructed using the potentials A_r^i and F_r^i of (2.11) and (2.13), the scattered fields can be also be represented by TE^r and TM^r modes and be constructed using potentials A_r^s and F_r^s .

The forms of A_r^s and F_r^s similar to those of A_r^i and F_r^i of (2.11) and (2.13), and we can represent them by

$$A_r^s = E_o \frac{\cos \phi}{\omega} \sum_{n=1}^{\infty} b_n \hat{H}_n^{(2)}(\beta r) [P_n^1(\cos \theta)] \quad (2.14a)$$

$$F_r^s = E_o \frac{\sin \phi}{\omega \eta} \sum_{n=1}^{\infty} c_n \hat{H}_n^{(2)}(\beta r) [P_n^1(\cos \theta)] \quad (2.14b)$$

where the coefficients b_n and c_n will be found using the appropriate boundary conditions. In (2.14a) and (2.14b) the spherical Hankel function of the second kind $\hat{H}_n^{(2)}(\beta r)$ has replaced the spherical Bessel Function $\hat{J}_n(\beta r)$ in (2.11) and (2.13) in order to represent outward traveling waves. Thus all the components of the total field, incident plus scattered, can be found using the below equations

$$E_r^t = \frac{1}{j\omega\mu\epsilon} \left(\frac{\partial^2}{\partial r^2} + \beta^2 \right) A_r^t \quad (2.15a)$$

$$E_\theta^t = \frac{1}{j\omega\mu\epsilon} \frac{1}{r} \frac{\partial^2 A_r^t}{\partial r \partial \theta} - \frac{1}{\epsilon} \frac{1}{r \sin \theta} \frac{\partial F_r^t}{\partial \phi} \quad (2.15b)$$

$$E_\phi^t = \frac{1}{j\omega\mu\epsilon} \frac{1}{r \sin \theta} \frac{\partial^2 A_r^t}{\partial r \partial \phi} + \frac{1}{\epsilon} \frac{1}{r} \frac{\partial F_r^t}{\partial \theta} \quad (2.15c)$$

$$H_r^t = \frac{1}{j\omega\mu\epsilon} \left(\frac{\partial^2}{\partial r^2} + \beta^2 \right) F_r^t \quad (2.15d)$$

$$H_\theta^t = \frac{1}{\mu} \frac{1}{r \sin \theta} \frac{\partial A_r^t}{\partial \phi} + \frac{1}{j\omega\mu\epsilon} \frac{1}{r} \frac{\partial^2 F_r^t}{\partial r \partial \theta} \quad (2.15e)$$

$$H_\phi^t = -\frac{1}{\mu} \frac{1}{r} \frac{\partial A_r^t}{\partial \theta} - \frac{1}{j\omega\mu\epsilon} \frac{1}{r \sin \theta} \frac{\partial^2 F_r^t}{\partial r \partial \phi} \quad (2.15f)$$

where A_r^t and F_r^t are each equal to the sum of (2.11), (2.13), (2.14a) and (2.14b),
or

$$A_r^t = A_r^i + A_r^s = E_o \frac{\cos \phi}{\omega} \sum_{n=1}^{\infty} \left[a_n \hat{J}_n(\beta r) + b_n \hat{H}_n^{(2)}(\beta r) \right] P_n^1(\cos \theta) \quad (2.16a)$$

$$F_r^t = F_r^i + F_r^s = E_o \frac{\sin \phi}{\omega \eta} \sum_{n=1}^{\infty} \left[a_n \hat{J}_n(\beta r) + c_n \hat{H}_n^{(2)}(\beta r) \right] P_n^1(\cos \theta) \quad (2.16b)$$

$$a_n = j^{-n} \frac{(2n+1)}{n(n+1)} \quad (2.16c)$$

To determine the coefficients b_n and c_n , the boundary conditions of

$$E_\theta^t(r = a, 0 \leq \theta \leq \pi, 0 \leq \phi \leq 2\pi) = 0 \quad (2.17a)$$

$$E_\phi^t(r = a, 0 \leq \theta \leq \pi, 0 \leq \phi \leq 2\pi) = 0 \quad (2.17b)$$

The boundary conditions of (2.17) are satisfied provided that

$$b_n = -a_n \frac{\hat{J}_n'(\beta a)}{\hat{H}_n^{(2)'}(\beta a)} \quad (2.18a)$$

$$c_n = -a_n \frac{\hat{J}_n(\beta a)}{\hat{H}_n^{(2)}(\beta a)}. \quad (2.18b)$$

The scattered electric field components can be written using (2.14a) and (2.14b) as

$$E_r^s = -j E_o \cos \phi \sum_{n=1}^{\infty} b_n [\hat{H}_n^{(2)''}(\beta r) + \hat{H}_n^{(2)}(\beta r)] P_n^1(\cos \theta) \quad (2.19a)$$

$$E_\theta^s = \frac{E_o}{\beta r} \cos \phi \sum_{n=1}^{\infty} \left[j b_n \hat{H}_n^{(2)'}(\beta r) \sin \theta P_n^1(\cos \theta) - c_n \hat{H}_n^{(2)}(\beta r) \frac{P_n^1(\cos \theta)}{\sin \theta} \right] \quad (2.19b)$$

$$E_\phi^s = \frac{E_o}{\beta r} \sin \phi \sum_{n=1}^{\infty} \left[j b_n \hat{H}_n^{(2)'}(\beta r) \frac{P_n^1(\cos \theta)}{\sin \theta} - c_n \hat{H}_n^{(2)}(\beta r) \sin \theta P_n^1(\cos \theta) \right] \quad (2.19c)$$

where $'$ denotes the derivative with respect to the argument.

2.2 Far-Field Observations

The Spherical Hankel function related to the regular Hankel function by

$$\hat{H}_n^{(2)}(\beta r) = \sqrt{\frac{\pi\beta r}{2}} H_{n+1/2}^{(2)}(\beta r) \quad (2.20)$$

Since for large values of βr the regular Hankel function can be represented by

$$H_{n+1/2}^{(2)}(\beta r) \stackrel{\beta r \rightarrow \infty}{\simeq} \sqrt{\frac{2j}{\pi\beta r}} j^{n+1/2} e^{-j\beta r} = j \sqrt{\frac{2}{\pi\beta r}} j^n e^{-j\beta r} \quad (2.21)$$

then the spherical Hankel function of (2.20) and its partial derivatives can be approximated by

$$\hat{H}_n^{(2)}(\beta r) \stackrel{\beta r \rightarrow \infty}{\simeq} j^{n+1} e^{-j\beta r} \quad (2.22a)$$

$$\hat{H}_n^{(2)'}(\beta r) = \frac{\partial \hat{H}_n^{(2)}(\beta r)}{\partial(\beta r)} \stackrel{\beta r \rightarrow \infty}{\simeq} -j^2 j^n e^{-j\beta r} = j^n e^{-j\beta r} \quad (2.22b)$$

$$\hat{H}_n^{(2)''}(\beta r) = \frac{\partial^2 \hat{H}_n^{(2)}(\beta r)}{\partial(\beta r)^2} \stackrel{\beta r \rightarrow \infty}{\simeq} -j^{n+1} e^{-j\beta r} \quad (2.22c)$$

For far field observations ($\beta r \rightarrow$ large), the electric field components of (2.19a) through (2.19c) can be simplified by using the approximations of (2.22). Since the radial component E_r^s of (2.19a) reduces with the approximations of (2.22) to zero, then in the far zone (2.19a) through (2.19c) can be approximated by

$$E_r^s \simeq 0 \quad (2.23a)$$

$$E_\theta^s \simeq j E_o \frac{e^{-j\beta r}}{\beta r} \cos \phi \sum_{n=1}^{\infty} j^n \left[b_n \sin \theta P_n^{1'}(\cos \theta) - c_n \frac{P_n^1(\cos \theta)}{\sin \theta} \right] \quad (2.23b)$$

$$E_\phi^s \simeq j E_o \frac{e^{-j\beta r}}{\beta r} \sin \phi \sum_{n=1}^{\infty} j^n \left[b_n \frac{P_n^1(\cos \theta)}{\sin \theta} - c_n \sin \theta P_n^{1'}(\cos \theta) \right] \quad (2.23c)$$

where b_n and c_n are given by (2.18a) through (2.18b).

2.3 Radar Cross Section

The bi-static radar cross section is,

$$\sigma(\text{bistatic}) = \lim_{r \rightarrow \infty} \left[4\pi r^2 \frac{|\mathbf{E}^s|^2}{|\mathbf{E}^i|^2} \right] \quad (2.24)$$

and it can be written using (2.1) and (2.23a) through (2.23c) as

$$\sigma(\text{bistatic}) = \frac{\lambda^2}{\pi} [\cos^2 \phi |A_\theta|^2 + \sin^2 \phi |A_\phi|^2] \quad (2.25)$$

where

$$|A_\theta|^2 = \left| \sum_{n=1}^{\infty} j^n \left[b_n \sin \theta P_n^1(\cos \theta) - c_n \frac{P_n^1(\cos \theta)}{\sin \theta} \right] \right|^2 \quad (2.26a)$$

$$|A_\phi|^2 = \left| \sum_{n=1}^{\infty} j^n \left[b_n \frac{P_n^1(\cos \theta)}{\sin \theta} - c_n \sin \theta P_n^1(\cos \theta) \right] \right|^2 \quad (2.26b)$$

The mono-static radar cross section can be found by first reducing the field expressions for observations toward $\theta = \pi$. In that direction the scattered electric field of interest is the copolar component of E_x^s , it can be found using (2.23a) through (2.23c) and the transformation by evaluating both

$$E_x^s = E_\theta^s \cos \theta \cos \phi |_{\theta=\pi, \phi=\pi} = E_\theta^s |_{\theta=\pi, \phi=\pi} \quad (2.27a)$$

$$E_x^s = -E_\phi^s \sin \phi |_{\theta=\pi, \phi=3\pi/2} = E_\phi^s |_{\theta=\pi, \phi=3\pi/2} \quad (2.27b)$$

To accomplish either (2.27a) or (2.27b) we need to evaluate the associated Legendre function and its derivative when $\theta = \pi$.

$$-\frac{P_n^1(\cos \theta)}{\sin \theta} \Big|_{\theta=\pi} = -(-1)^n \frac{n(n+1)}{2} \quad (2.28a)$$

$$\sin \theta P_n^1(\cos \theta) \Big|_{\theta=\pi} = \sin \theta \frac{dP_n^1}{d(\cos \theta)} = (-1)^n \frac{n(n+1)}{2} \quad (2.28b)$$

$$\begin{aligned}
E_\theta^s \Big|_{\substack{\theta=\pi \\ \phi=\pi}} &= jE_o \frac{e^{-j\beta r}}{\beta r} \sum_{n=1}^{\infty} j^n (-1)^n \frac{n(n+1)}{2} [b_n - c_n] \\
&= -jE_o \frac{e^{-j\beta r}}{\beta r} \sum_{n=1}^{\infty} j^n (-1)^n \frac{n(n+1)}{2} a_n \left[\frac{\hat{J}'_n(\beta a)}{\hat{H}_n^{(2)'}(\beta a)} - \frac{\hat{J}_n(\beta a)}{\hat{H}_n^{(2)}(\beta a)} \right] \quad (2.29) \\
E_\theta^s \Big|_{\substack{\theta=\pi \\ \phi=\pi}} &= -jE_o \frac{e^{-j\beta r}}{\beta r} \sum_{n=1}^{\infty} (-1)^n \frac{(2n+1)}{2} \left[\frac{\hat{J}'_n(\beta a) \hat{H}_n^{(2)}(\beta a) - \hat{J}_n(\beta a) \hat{H}_n^{(2)'}(\beta a)}{\hat{H}_n^{(2)'}(\beta a) \hat{H}_n^{(2)}(\beta a)} \right]
\end{aligned}$$

which reduces, using the Wronskian [2] for spherical Bessel functions of

$$\hat{J}'_n(\beta a) \hat{H}_n^{(2)}(\beta a) - \hat{J}_n(\beta a) \hat{H}_n^{(2)'}(\beta a) = j \left[\hat{J}_n(\beta a) \hat{Y}'_n(\beta a) - \hat{J}'_n(\beta a) \hat{Y}_n(\beta a) \right] = j \quad (2.30)$$

to

$$E_\theta^s \Big|_{\substack{\theta=\pi \\ \phi=\pi}} = E_o \frac{e^{-j\beta r}}{2\beta r} \sum_{n=1}^{\infty} \left[\frac{(-1)^n (2n+1)}{\hat{H}_n^{(2)'}(\beta a) \hat{H}_n^{(2)}(\beta a)} \right] \quad (2.31)$$

Thus monostatic radar cross section can be expressed using (2.31) by

$$\sigma(\text{monostatic}) = \lim_{r \rightarrow \infty} \left[4\pi r^2 \frac{|\mathbf{E}^s|^2}{|\mathbf{E}^i|^2} \right] = \frac{\lambda^2}{4\pi} \left| \sum_{n=1}^{\infty} \frac{(-1)^n (2n+1)}{\hat{H}_n^{(2)'}(\beta a) \hat{H}_n^{(2)}(\beta a)} \right|^2 \quad (2.32)$$

2.4 Choice of the Number of Terms in Series Summation

The solution of scattered electric field components contains a summation operator that goes to infinity. In order to decide on where to truncate the series, $E_{\theta}^s(r = a)$ and $E_{\phi}^s(r = a)$ scattered components are compared with $-E_{\theta}^i(r = a)$ and $-E_{\phi}^i(r = a)$ incident electric field components at 30 points. These 30 points are taken from the three primary cuts ($\phi = 0$, $\phi = \pi/2$, and $\theta = \pi/2$) equally spaced. The maximum error is bounded below 10^{-3} level by increasing the number of series (N) among these 30 points. At every frequency value, this operation is repeated and the number of series versus (a/λ) plot is produced in Fig. 2.2. The horizontal axes (a/λ) also implies the frequency values.

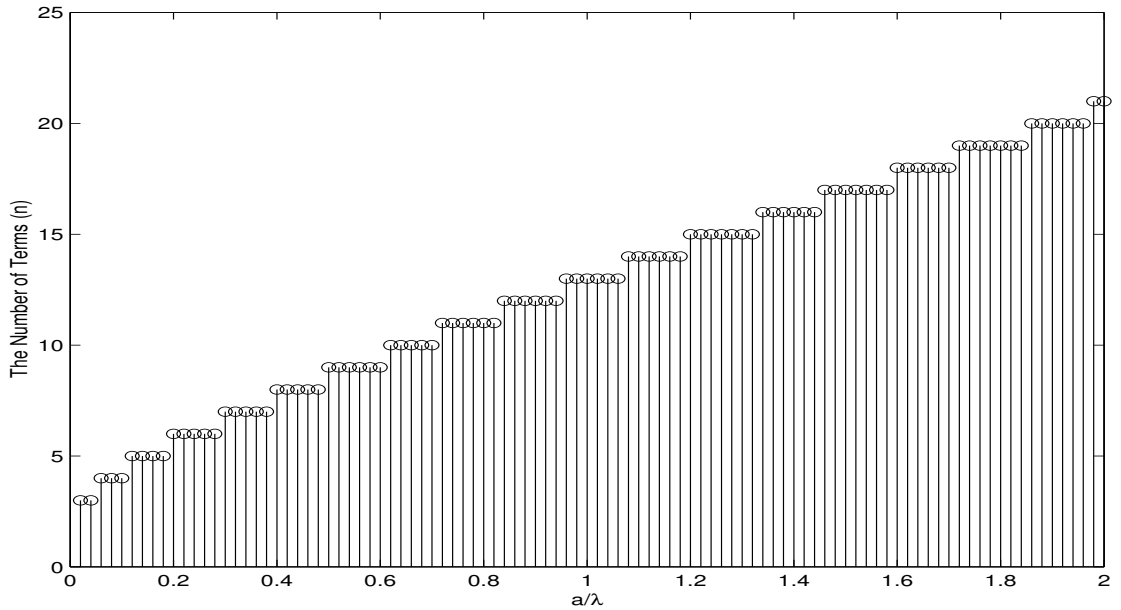


Figure 2.2: The number of series is shown between $a/\lambda = 0$ and $a/\lambda = 2$. $[0, 2]$ interval is divided 100 points with sampling period $T_s = 0.02$

$$\frac{f}{\lambda} = \left(\frac{c}{a}\right).$$

2.5 Calculation of RCS by Using Scattered Electric Fields

In the far field, we have already derived the E_{θ}^s and E_{ϕ}^s expressions in Eq. (2.23b) and Eq. (2.23c). In those expressions, the terms are generally dependent to the number of series (n). The number of series is directly proportional to the frequency (a/λ). This is the main reason for the cost of computation time at high frequency values. The information about Legendre polynomials is given at appendix A.2. The scattered electric fields $E_{\theta}^s(\theta = \pi, \phi = \phi)$ and $E_{\phi}^s(\theta = \pi, \phi = \phi)$ are calculated between $a/\lambda=0$ and $a/\lambda=2$ with 0.02 sampling period. The normalized RCS values are calculated by using the Eq. (2.24) at $(\theta = \pi, \phi = \phi)$. The results are shown in Fig. 2.3. The selected look angle exactly denotes the

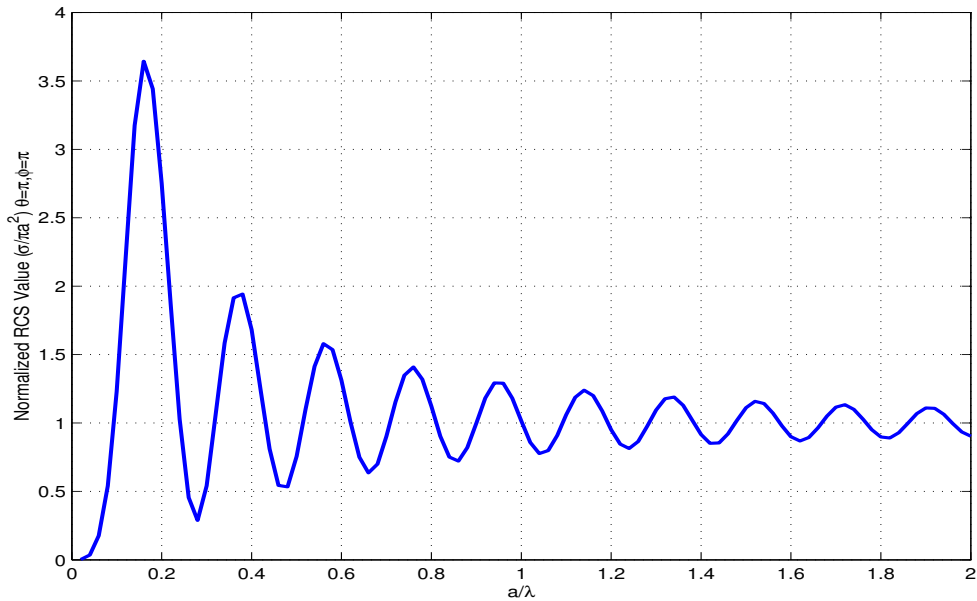


Figure 2.3: Normalized radar cross section for a conducting sphere as a function of its radius ($\theta = \pi, \phi = \phi$).

monostatic RCS values.

The scale of the vertical axes in Fig. 2.3 is converted to logarithmic. A plot of monostatic RCS as a function of the sphere radius is shown in Figure 2.4. This is a classic signature that can be found in any literature dealing with electromagnetic

scattering. The total curve can be subdivided into three regions; the Rayleigh, the Mie (or resonance), and the optical regions. The Rayleigh region represents the part of the curve for small values of the radius ($a \leq 0.1\lambda$) and the optical region represents the RCS of the sphere for large values of the radius (typically $a \geq 2\lambda$). The region between those two extremes is the Mie or resonance region. For large values, the RCS approaches the value of πa^2 that is the physical area of the cross section of the sphere.

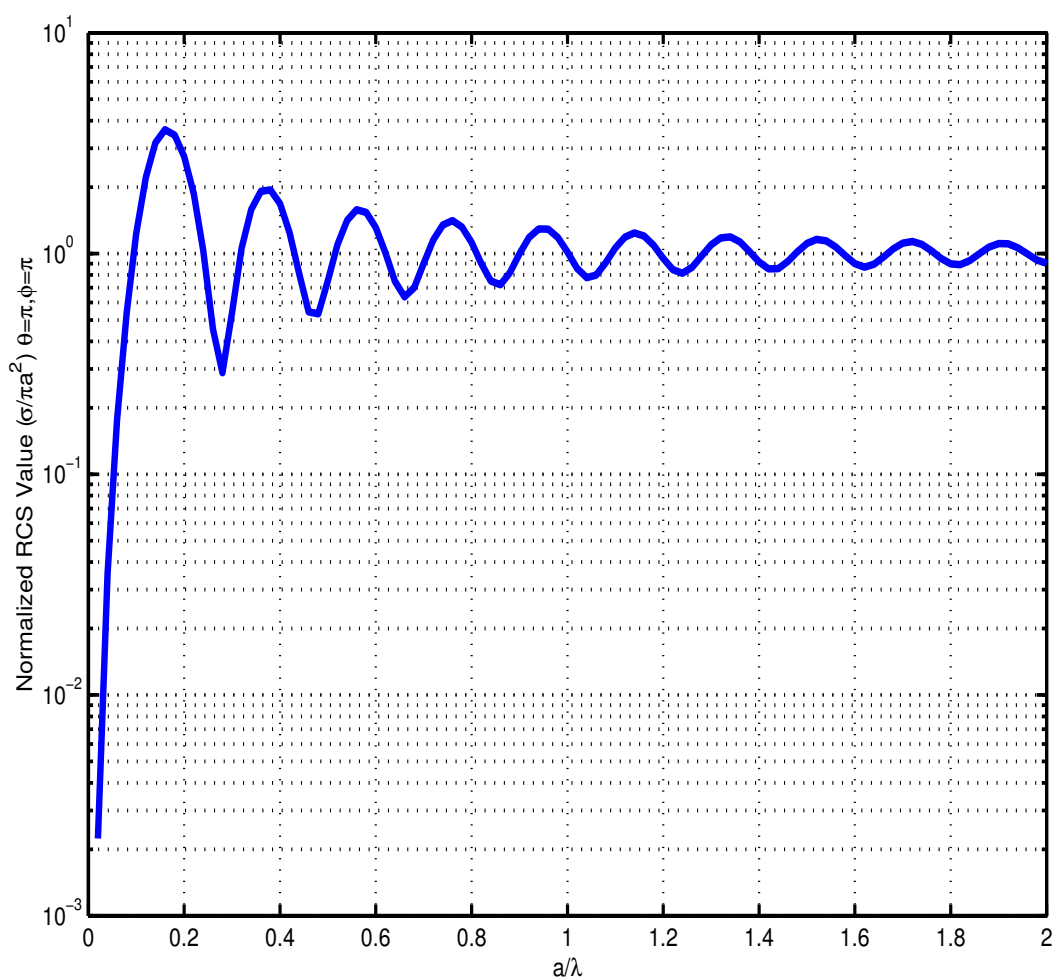


Figure 2.4: Normalized monostatic radar cross section for a conducting sphere as a function of its radius. The RCS values are plotted in the logarithmic scale.

2.6 Induced Current Distribution of the PEC Sphere

We already know that the tangential components of the magnetic field intensity are discontinuous next to a perfect electric conductor an amount of equal to the induced linear current density [13].

$$\begin{aligned}\mathbf{J} &= \hat{n} \times \mathbf{H}(r = a) = \hat{a}_r \times (\hat{a}_\theta H_\theta + \hat{a}_\phi H_\phi) \\ &= \hat{a}_\phi H_\theta - \hat{a}_\theta H_\phi\end{aligned}\tag{2.33}$$

$$J_\theta = -H_\phi$$

$$J_\phi = H_\theta$$

H_θ , H_ϕ magnetic field intensities can be derived by substituting equations A_r^t (2.16a) and F_r^t (2.16b) into equations (2.15e) and (2.15f), after that H_θ becomes;

$$\begin{aligned}H_\theta \Big|_{r=a} &= \frac{-E_\theta \sin \theta}{\omega \mu a} \sum_{n=1}^{\infty} \left\{ \frac{a_n}{\hat{H}_n^{(2)}(\beta a)} \left[\hat{J}_n(\beta a) \hat{H}_n^{(2)'}(\beta a) - \hat{J}_n'(\beta a) \hat{H}_n^{(2)}(\beta a) \right] \frac{P_n^1(\cos \theta)}{\sin \theta} \right. \\ &\quad \left. - \frac{a_n}{\hat{H}_n^{(2)}(\beta a)} \left[\hat{J}_n'(\beta a) \hat{H}_n^{(2)}(\beta a) - \hat{J}_n(\beta a) \hat{H}_n^{(2)'}(\beta a) \right] \sin \theta P_n^1(\cos \theta) \right\}\end{aligned}\tag{2.34}$$

using the Wronskian [2] for spherical Bessel functions of

$$\left[\hat{J}_n(\beta a) \hat{H}_n^{(2)'}(\beta a) - \hat{J}_n'(\beta a) \hat{H}_n^{(2)}(\beta a) \right] = -j$$

with the help of Eq. (2.33), J_ϕ is equal to

$$J_\phi = H_\theta = \frac{E_\theta \sin \phi}{\omega \mu a} \sum_{n=1}^{\infty} a_n \left[\frac{P_n^1(\cos \theta)}{\sin \theta \hat{H}_n^{(2)'}(\beta a)} + j \frac{\sin \theta P_n^1(\cos \theta)}{\hat{H}_n^{(2)}(\beta a)} \right]\tag{2.35}$$

by the same manner J_θ can be found;

$$J_\theta = \frac{j E_\theta \cos \phi}{\eta \beta a} \sum_{n=1}^{\infty} a_n \left[\frac{\sin \theta P_n^1(\cos \theta)}{\hat{H}_n^{(2)}(\beta a)} + j \frac{P_n^1(\cos \theta)}{\sin \theta \hat{H}_n^{(2)'}(\beta a)} \right]\tag{2.36a}$$

$$J_\phi = \frac{j E_\theta \sin \phi}{\eta \beta a} \sum_{n=1}^{\infty} a_n \left[\frac{P_n^1(\cos \theta)}{\sin \theta \hat{H}_n^{(2)'}(\beta a)} + j \frac{\sin \theta P_n^1(\cos \theta)}{\hat{H}_n^{(2)}(\beta a)} \right]\tag{2.36b}$$

The current distribution J_θ , J_ϕ values are calculated by sampling in the θ and ϕ direction by using the number of series in Section (2.4). The magnitude of $|\mathbf{J}|$

current distribution are plotted in Fig. 2.5, Fig. 2.6 and Fig. 2.7. Notice that in Fig. 2.6 and Fig. 2.7 are at the optical frequencies, the dark region can be separated from the light region. Individually, the magnitude and phase values of J_θ and J_ϕ components are plotted in Fig. 2.8

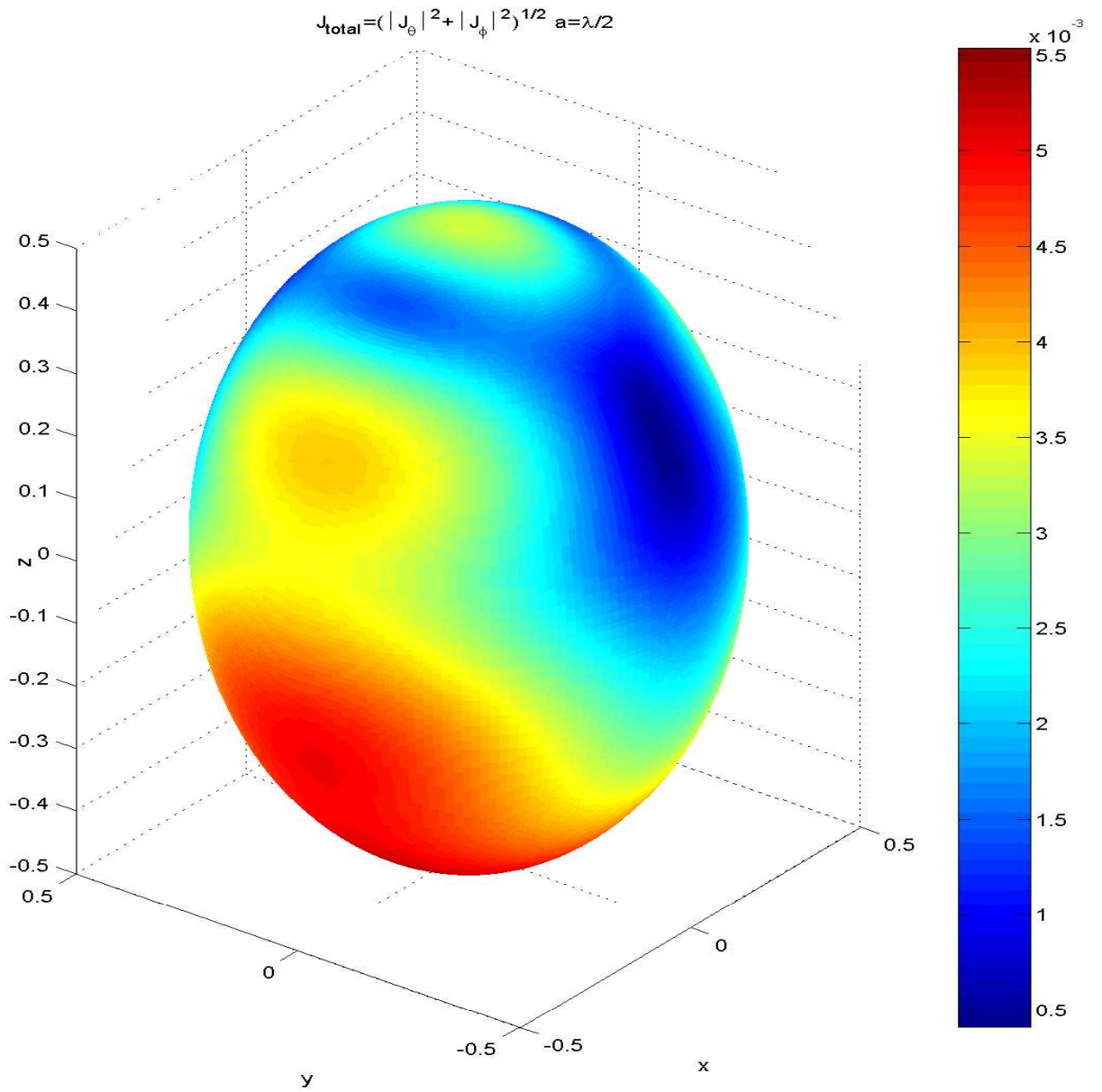


Figure 2.5: Induced current distribution on the surface of the sphere. The radius of the sphere $a = \lambda/2$. The resultant surface current is calculated ($\mathbf{J} = (|J_{\theta}|^2 + |J_{\phi}|^2)^{1/2}$)

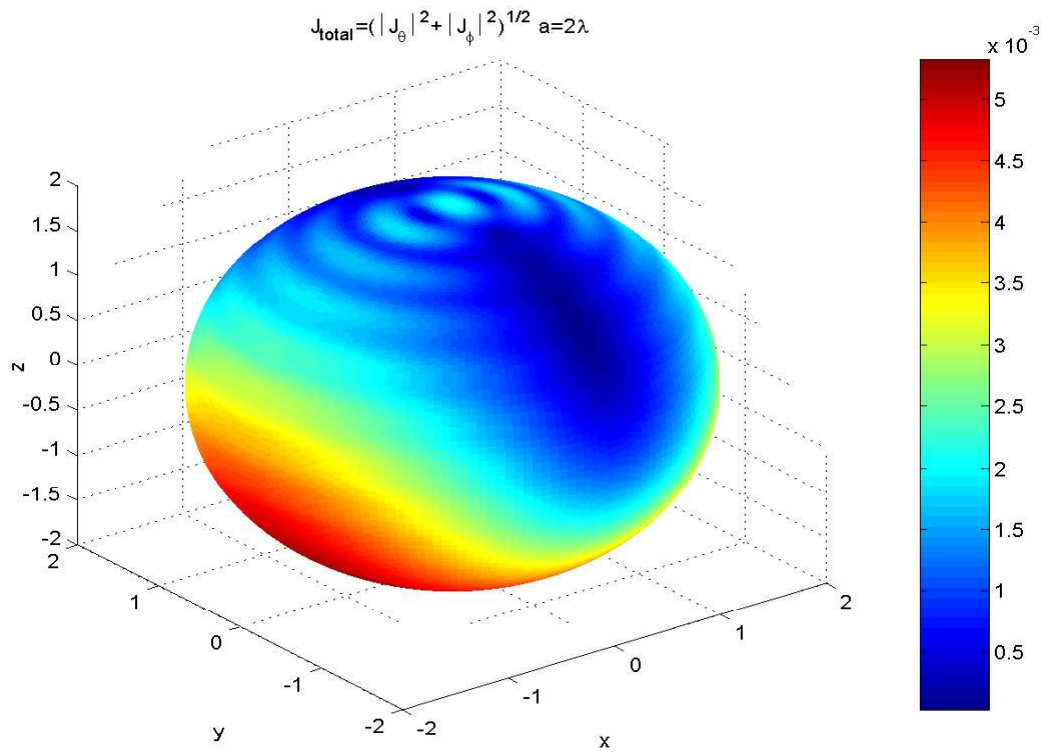


Figure 2.6: Induced current distribution of the sphere when the radius (a) is equal to 2λ . The resultant surface current is calculated ($\mathbf{J} = (|J_{\theta}|^2 + |J_{\phi}|^2)^{1/2}$)

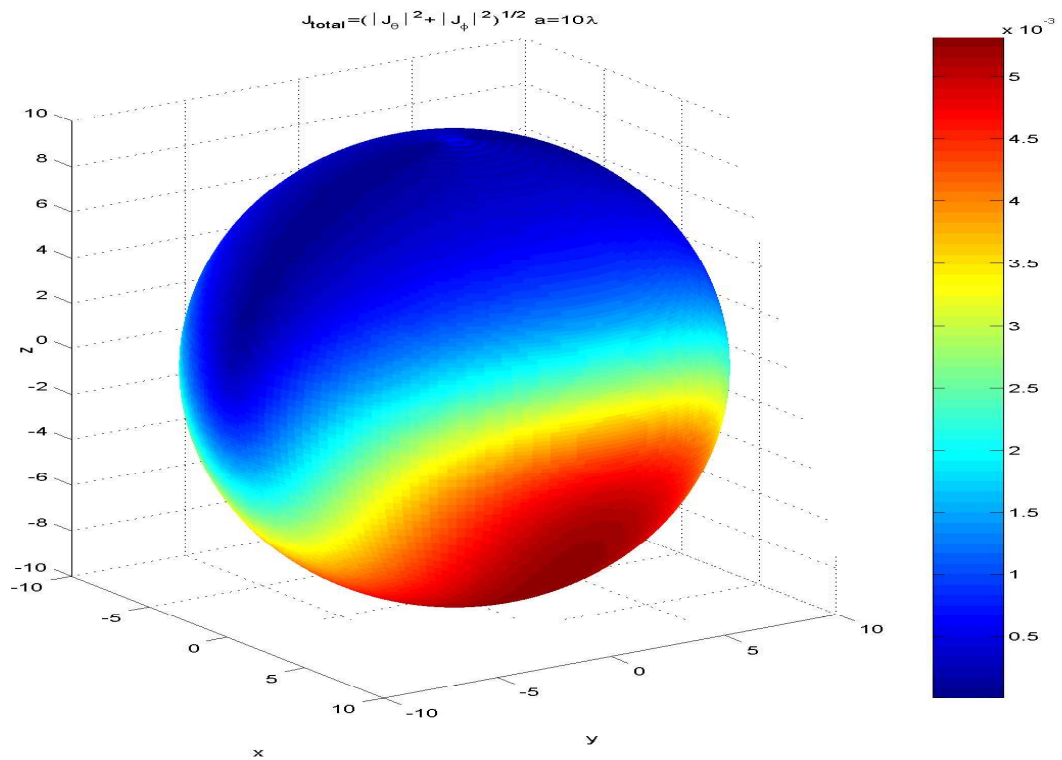


Figure 2.7: Induced current distribution when $a = 10\lambda$. The dark and light region can be seen easily. The magnitude of the resultant current is calculated. $|\mathbf{J}| = (|J_{\theta}|^2 + |J_{\phi}|^2)^{1/2}$

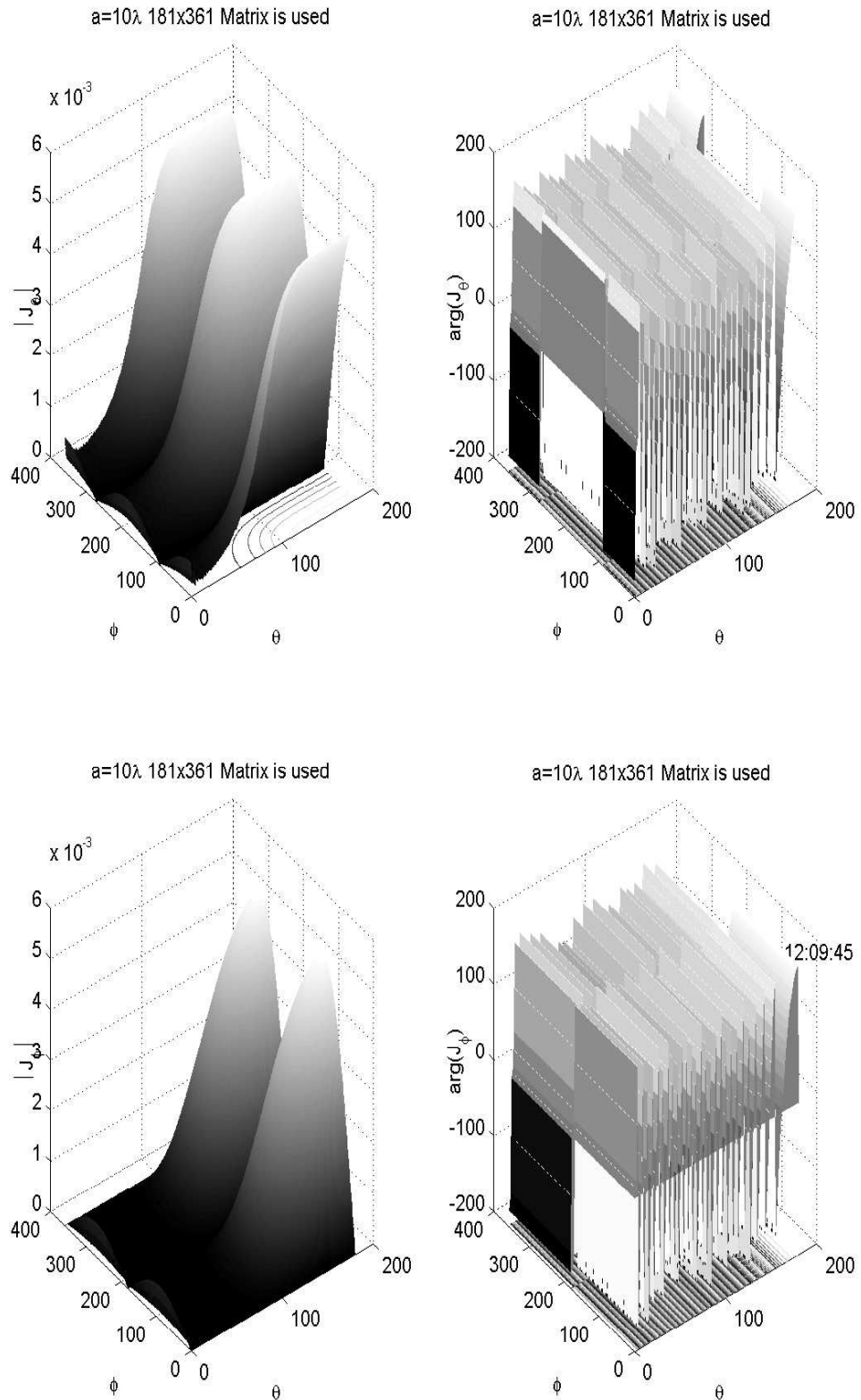


Figure 2.8: Induced Surface Current Distributions at $a = 10\lambda$, $|J_\theta|$ and $|J_\phi|$ and its phases. The plot curves, 181×361 sampled matrix is used on the surface of the sphere

Chapter 3

Prony's Method

Signal modeling is an important problem that arises in a variety of applications. One application of signal modeling is in the area of signal prediction (extrapolation) and signal interpolation. For example, the signal $x(t)$ is intended to be modelled. Sampled data $x[k] = x(kT_s)$ can be represented by a linear combination of exponentials as

$$\hat{x}[k] = \sum_{i=1}^M |R_i| e^{[(\alpha_i + j\omega_i)kT_s + j\theta_i]} \quad (3.1)$$

where

$$\begin{aligned} \hat{x}[k] &: \text{the estimate of } x[k] \\ \alpha_i &: \text{damping factor} \\ \omega_i &: \text{Angular frequency } (\omega_i = 2\pi f_i) \\ R_i &: \text{Residue or complex coefficient } (R_i = |R_i|e^{j\theta_i}) \\ \theta_i &: \text{Phase angle} \\ T_s &: \text{Sampling period} \end{aligned} \quad (3.2)$$

Prony's method [5] is a technique to solve parameters of M -term exponential model from N complex data samples $x[0], x[1], \dots, x[N-1]$. There are three basic steps in the Prony's method:

1. Linear prediction parameters that fit the sampled data are determined.
2. The damping factors and angular frequencies are estimated from roots of a polynomial formed from the linear prediction coefficients.
3. Solution of a second set of linear equations yields the estimates of complex residues.

In case of real data samples,

$$\hat{x}[k] = \sum_{i=1}^{M/2} 2|R_i|e^{-\alpha_i k T_s} \cos(\omega_i k T_s + \theta_i) \quad k = 0, 1, \dots, N-1 \quad (3.3)$$

If the number of complex exponentials M is even, then there are $M/2$ damped cosines. If M is odd, then there are $(M-1)/2$ damped cosines plus a single purely damped exponential.

3.1 Simultaneous Exponential Parameter Estimation

The M -exponent discrete-time function of Eq. (3.1) may be concisely expressed in the form

$$\hat{x}[k] = \sum_{i=1}^M R_i z_i^k \quad k = 0, 1, \dots, N-1, \quad (3.4)$$

where R_i is complex coefficient that represents a t -independent parameter, whereas z_i is a complex exponent that represents a t -dependent parameter.

Ideally, one would like to minimize the squared error over the N data values

$$\rho = \sum_{k=0}^{N-1} |\epsilon[k]|^2 \quad (3.5)$$

where

$$\epsilon[k] = x[k] - \hat{x}[k] = x[k] - \sum_{i=1}^M R_i z_i^k \quad (3.6)$$

with respect to the R_i parameters, the z_i parameters and the number of exponents M simultaneously. Actually, this is a difficult problem and this difficulty can be demonstrated with a single-exponent case. Minimization of the squared error ρ using the damped exponential model

$$\hat{x}[k] = R \exp(\alpha k T_s) \quad (3.7)$$

is obtained by setting to zero the derivatives with respect to R and α .

$$\begin{aligned} \frac{\partial \rho}{\partial R} &= c_1 - c_2 R = 0 \\ \frac{\partial \rho}{\partial \alpha} &= c_3 - c_4 R = 0 \end{aligned} \quad (3.8)$$

where

$$\begin{aligned} c_1 &= \sum_{k=0}^{N-1} x[k] \exp(\alpha k T_s) \\ c_2 &= \sum_{k=0}^{N-1} \exp(2\alpha k T_s) \\ c_3 &= \sum_{k=0}^{N-1} (k+1) x[k] \exp(\alpha k T_s) \\ c_4 &= \sum_{k=0}^{N-1} (k+1) \exp(\alpha k T_s) \end{aligned} \quad (3.9)$$

In this case, $\hat{x}[k]$, R and α are assumed real. From the first equation of (3.8) one obtains $R = c_1/c_2$; substituting this into second equation of (3.8) yields

$$c_2 c_3 = c_1 c_4 \quad (3.10)$$

This is a highly nonlinear expression in terms of sums involving $\exp(\alpha k T_s)$ which must be solved for α . No analytic solution is available. This difficulty led to the development of suboptimum minimization of ρ , known as the least-squares Prony's method that utilizes linear equation solutions. The Prony's method embeds the nonlinear aspects of the exponential model into a polynomial factoring, for which reasonably fast solution algorithms are available.

3.2 Original Prony Concept

If as many data samples are used as there are exponential parameters, then an exact exponential fit to the data may be made. Consider the M -exponent discrete-function

$$x[k] = \sum_{i=1}^M R_i z_i^k \quad (3.11)$$

$2M$ complex samples $x[0], x[1], \dots, x[2M - 1]$ are used to model $2M$ complex parameters $R_1, R_2, \dots, R_M; z_1, z_2, \dots, z_M$.

$$\begin{bmatrix} z_1^0 & z_2^0 & \cdots & z_M^0 \\ z_1^1 & z_2^1 & \cdots & z_M^1 \\ \vdots & \vdots & & \vdots \\ z_1^{M-1} & z_2^{M-1} & \cdots & z_M^{M-1} \end{bmatrix} \begin{bmatrix} R_1 \\ R_2 \\ \vdots \\ R_M \end{bmatrix} = \begin{bmatrix} x[0] \\ x[1] \\ \vdots \\ x[M-1] \end{bmatrix} \quad (3.12)$$

If a method is obtained to determine the z_i elements separately, Eq. (3.12) represent a set of linear simultaneous equations that can be solved for unknown vector of complex coefficients. Separation algorithm can be done by solving a homogenous linear constant coefficient difference equation. In order to find the form of this difference equation, first define the polynomial $\phi(z)$ that has z_i exponent as its roots,

$$\phi(z) = \prod_{i=1}^M (z - z_i). \quad (3.13)$$

If the products of Eq (3.13) are expanded into a power series, then the polynomial may be represented as the summation.

$$\phi(z) = \sum_{m=0}^M a[m] z^{M-m} = a[0] z^M + a[1] z^{M-1} + \dots + a[M] z^0. \quad (3.14)$$

with complex coefficients $a[m]$ such that $a[0] = 1$. Shifting the index of Eq. (3.11) from k to $k - m$ and multiplying by the parameter $a[m]$ yields

$$a[m] x[k - m] = a[m] \sum_{i=1}^M R_i z_i^{k-m} \quad (3.15)$$

Forming similar products $a[0]x[k], \dots, a[m-1]x[k-m+1]$ and summing produces

$$\sum_{m=0}^M a[m]x[k-m] = \sum_{i=1}^M R_i \sum_{m=0}^M a[m]z_i^{k-m} \quad (3.16)$$

It has been changed summation location of m indices with i , Equation (3.16) is valid for $M \leq k \leq 2M - 1$. Making the substitution in Eq. (3.16), $z_i^{k-m} = z_i^{k-M} z_i^{M-m}$ then

$$\sum_{m=0}^M a[m]x[k-m] = \sum_{i=1}^M R_i z_i^{k-M} \underbrace{\sum_{m=0}^M a[m]z_i^{M-m}}_0 = 0 \quad (3.17)$$

The right-hand side in Eq. (3.17) with a bracket may be recognized as the polynomial defined by Eq. (3.14), evaluated at each of roots z_i , yielding a zero result as indicated. The polynomial is the *characteristic equation* associated with this linear difference equation. For $k = M$ Eq. (3.17) yields,

$$a[1]x[M-1] + a[2]x[M-2] + \dots + a[M]x[0] = -x[M]$$

For $k = M, \dots, 2M - 1$

$$\begin{bmatrix} x[M-1] & x[M-2] & \dots & x[0] \\ x[M] & x[M-1] & \dots & x[1] \\ \vdots & \vdots & & \vdots \\ x[2M-2] & x[2M-3] & \dots & x[M-1] \end{bmatrix} \begin{bmatrix} a[1] \\ a[2] \\ \vdots \\ a[M] \end{bmatrix} = - \begin{bmatrix} x[M] \\ x[M+1] \\ \vdots \\ x[2M-1] \end{bmatrix} \quad (3.18)$$

Roots z_i 's can be calculated by substituting the solution of matrix Eq. (3.18) into Eq. (3.14).

The damping α_i and sinusoidal frequency f_i may be determined from the root z_i using the relationships

$$\alpha_i = \ln |z_i| / T_s \quad (3.19)$$

$$f_i = \tan^{-1} [Im\{z_i\} / Re\{z_i\}] / 2\pi T_s \quad (3.20)$$

Again the Prony procedure to fit M exponentials to $2M$ complex data samples may be now be summarized in three steps.

1. Solution of Eq. (3.18) for the polynomial coefficients is obtained.
2. The roots of the polynomial defined by Eq. (3.14) are calculated. The damping α_i and sinusoidal frequency f_i may be determined from the roots using the relationship Eq. (3.19) and (3.20).
3. The roots computed in the second step are used to construct the matrix elements of Eq. (3.12), which is then solved for the M complex parameters R_1, R_2, \dots, R_M .

3.3 Least-Squares Prony's Method

In applications, the number of data points, namely N usually exceeds the minimum number needed to fit a model of M exponentials, i.e., $N > 2M$. In this overdetermined case, the data sequence can only be approximated as an exponential sequence,

$$\hat{x}[k] = \sum_{i=1}^M R_i z_i^k \quad k = 0, 1, \dots, N-1, \quad (3.21)$$

Approximation error is denoted $\epsilon[k] = x[k] - \hat{x}[k]$. Simultaneously finding the order M and the parameters $\{R_i, z_i\}$ for $i = 1$ to $i = M$ that minimizes total squared error $\rho = \sum_{k=0}^{N-1} |\epsilon[k]|^2$ was shown in section 3.1 to be a difficult nonlinear problem. A variant of Prony method can provide a suboptimum solution. Substitution of appropriate linear-least squares procedures for the first and third steps of the Prony's method that sometimes been called the *extended Prony method*. In the overdetermined sampled data case, the difference Eq. (3.17) is modified to

$$\sum_{m=0}^M [a[m]x[k-m]] = e[k] \quad (3.22)$$

$$a[0]x[k] + a[1]x[k-1] + \dots + a[M]x[k-M] = -e[k]$$

The term $e[k]$ represents the linear prediction approximation error, in contrast to error $\epsilon[k]$, which represents the exponential approximation error. Expression in Eq. (3.22) is identical to the forward linear prediction error equation, making each $a[m]$ term a linear prediction parameter. Instead of Eq. (3.17), the $a[m]$ parameters may be selected as those that minimize the linear prediction squared error $\sum_{k=M}^{N-1} |e[k]|^2$ rather than the exponential squared error ρ . This is simply the covariance method of linear prediction. The number of exponentials M may be estimated by using Singular Value Decomposition (SVD) analysis. The maximum order is limited to $M \leq N/2$. The exponents z_1, z_2, \dots, z_M can be determined by least squares linear prediction analysis and polynomial factoring, then calculation of R_1, R_2, \dots, R_M coefficients becomes a linear problem. Minimizing the squared error with respect to each of the R_i parameters yields the complex values $M \times M$ matrix normal equation.

$$[\mathbf{Z}^H \mathbf{Z}] \mathbf{R} = \mathbf{Z}^H \mathbf{x}, \quad (3.23)$$

where the $N \times M$ matrix \mathbf{Z} , the $M \times 1$ vector \mathbf{R} , $N \times 1$ data vector as follows

$$\mathbf{Z} = \begin{bmatrix} z_1^0 & z_2^0 & \cdots & z_M^0 \\ z_1^1 & z_2^1 & \cdots & z_M^1 \\ \vdots & \vdots & & \vdots \\ z_1^{N-1} & z_2^{N-1} & \cdots & z_M^{N-1} \end{bmatrix}, \mathbf{R} = \begin{bmatrix} R_1 \\ R_2 \\ \vdots \\ R_M \end{bmatrix}, \mathbf{x} = \begin{bmatrix} x[0] \\ x[1] \\ \vdots \\ x[N-1] \end{bmatrix}. \quad (3.24)$$

The $M \times M$ Hermitian matrix $\mathbf{Z}^H \mathbf{Z}$ has the form

$$\mathbf{Z}^H \mathbf{Z} = \begin{pmatrix} \gamma_{11} & \cdots & \gamma_{1M} \\ \vdots & & \vdots \\ \gamma_{M1} & \cdots & \gamma_{MM} \end{pmatrix}$$

where

$$\gamma_{ij} = \sum_{k=0}^{N-1} (z_i^* z_j)^k = \gamma_{ji}^* \quad (3.25)$$

A useful relation that avoids the summation of Eq. (3.25)

$$\gamma_{ij} = \begin{cases} \frac{(z_i^* z_j)^{N-1}}{z_j^* z_i - 1} & \text{if } z_i^* z_j \neq 1 \\ N & \text{if } z_i^* z_j = 1 \end{cases} .$$

The Prony's method will also fit exponentials to any additive noise present in the data. An exponential model incorporating additive noise would have the form of

$$\hat{y}[k] = \sum_{i=1}^M R_i z_i^k + \epsilon[k] \quad . \quad (3.26)$$

The function $\epsilon[k]$ has also been used to represent the approximation error of the exponential model. If $\hat{y}[k] - \epsilon[k]$ is used in place of $x[k]$ in the analysis, then the linear difference equation that describes the process consisting of sum of exponentials plus white noise

$$y[k] = \sum_{i=1}^M a[i] y[k - i] + \sum_{i=0}^M a[i] \epsilon[k] \quad . \quad (3.27)$$

3.4 Application of Prony's Method

Prony's method is applied to estimate the RCS values of the sphere. Exact values are calculated by using Eq. (2.24) for monostatic case.

Initially, the parameters of the exponential model in Eq. (3.1) $M = 7$ (number of terms), N (number of samples) are chosen and the results are shown in Fig. 3.1. In this calculation, the sampled data is taken from the interval $[0, 2]$ with a sampling period of 0.02. Although Prony's method has a good performance until $a/\lambda = 0.2$, after this value divergence of dashed line can be clearly observed from the exact RCS values. The bottom part of this figure shows the error, which is defined as the difference of the two results.

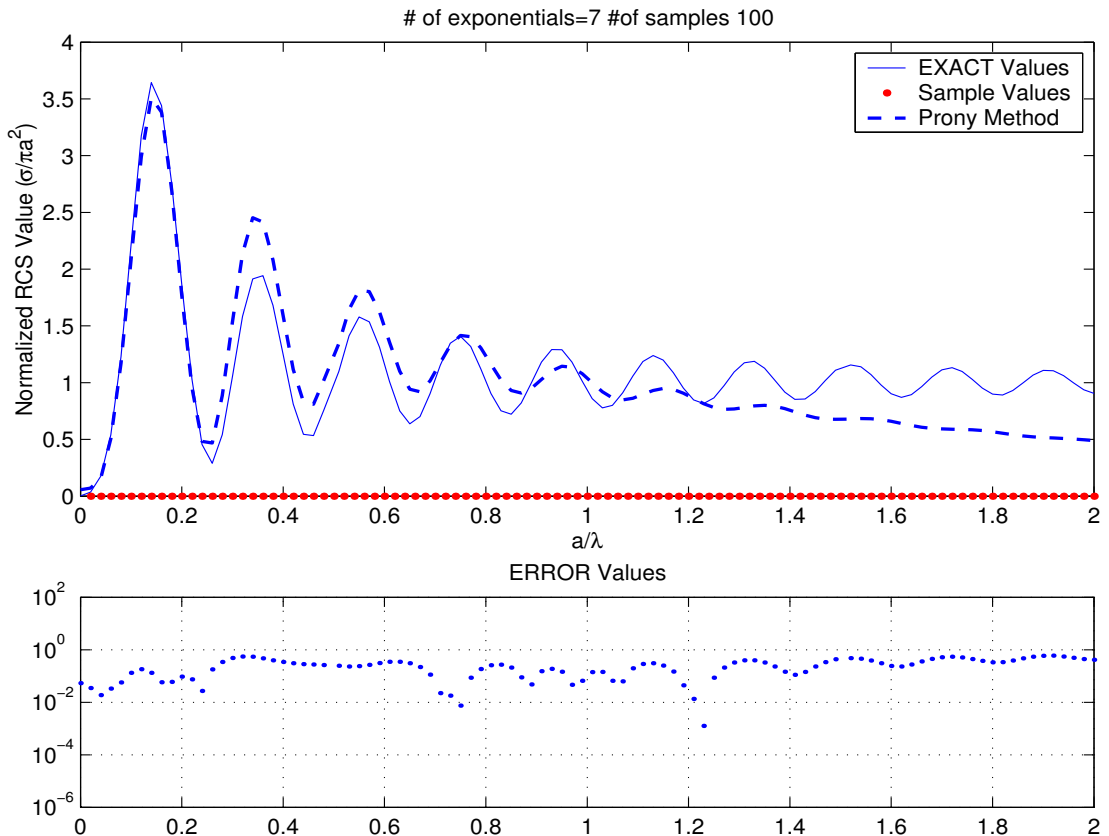


Figure 3.1: Application of the Prony's method to monostatic RCS results $M = 7$, $N = 100$, $T_s = 0.02$, Samples are taken from the interval= $[0.02, 2]$

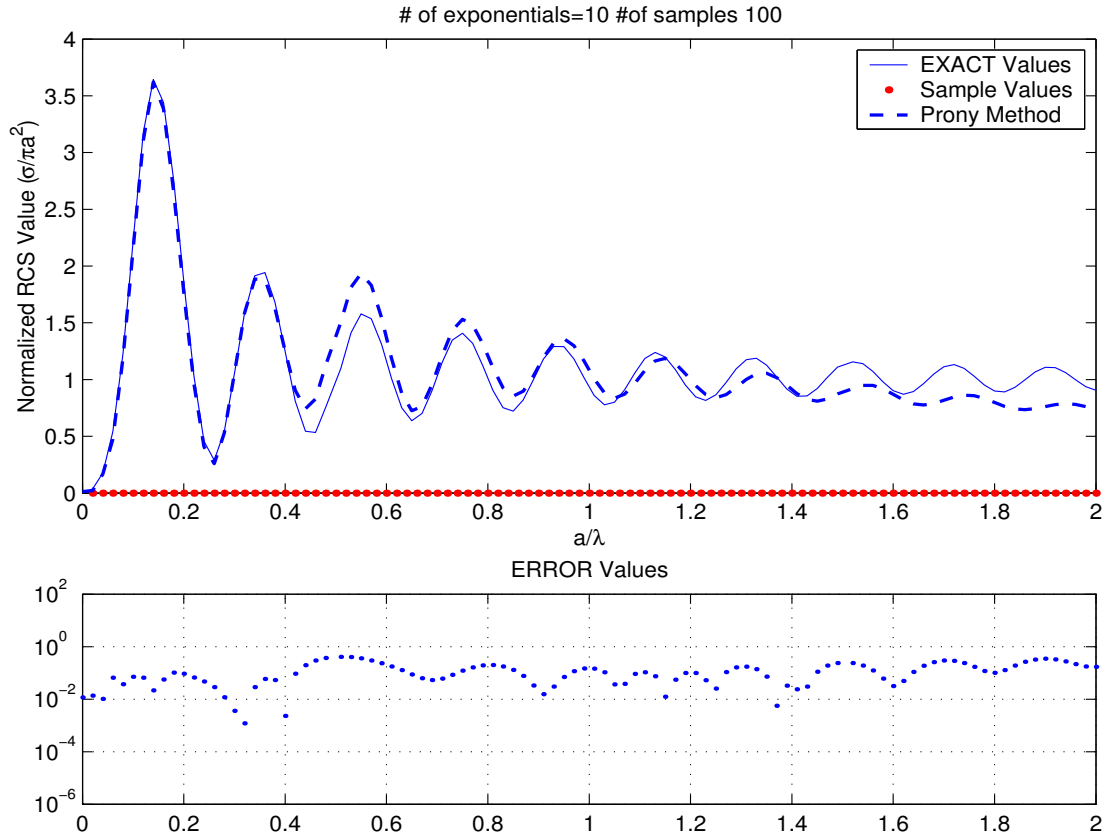


Figure 3.2: Application of the Prony's method to monostatic RCS results. The number of exponentials is increased to $M = 10$

When we increase the number of terms from 7 to 10 in Fig. 3.2, and keep the number of samples same as before, it is observed that the error becomes less than that of Fig. 3.1.

A better agreement is observed in Fig. 3.3, when the number of terms is taken as 15. In Fig. 3.3, the error values are obtained nearly below the 0.01 line. Our goal is to keep the error strictly less than 0.01.

In Fig. 3.4, 20 exponentials are used to represent the RCS values. At the bottom part of the Fig. 3.3, one can observe the decrease of the error values. In Fig. 3.5, we have used the maximum number (49) of exponentials to find the limits of decrease in error values. Up to now, applications of the Prony's Method is about interpolation simulations.

Finally, in Fig. 3.6 an implementation of extrapolation is demonstrated by using sampled data in the interval $[0, 1.6]$ with $T_s = 0.02$. By using the coefficients and

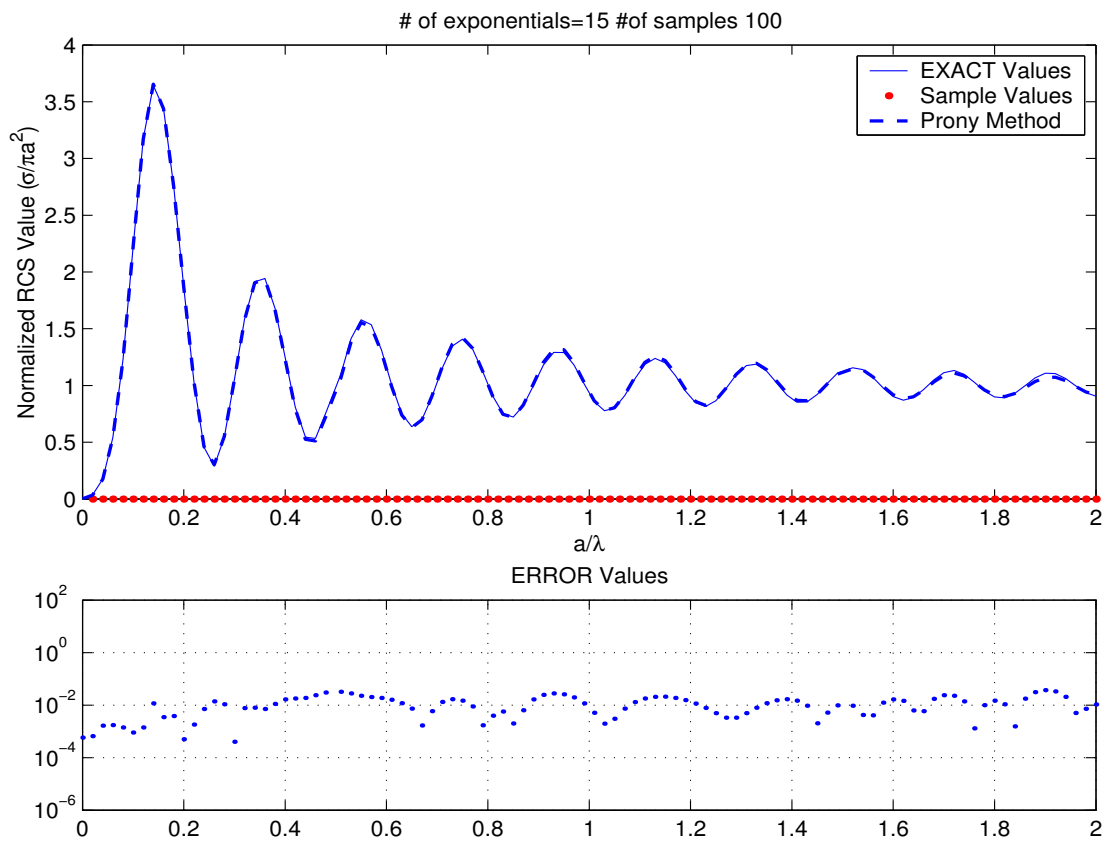


Figure 3.3: Application of the Prony's Method to monostatic RCS results $M = 15$, $N = 100$, $T_s = 0.02$, Sampling interval=[0.02, 2]

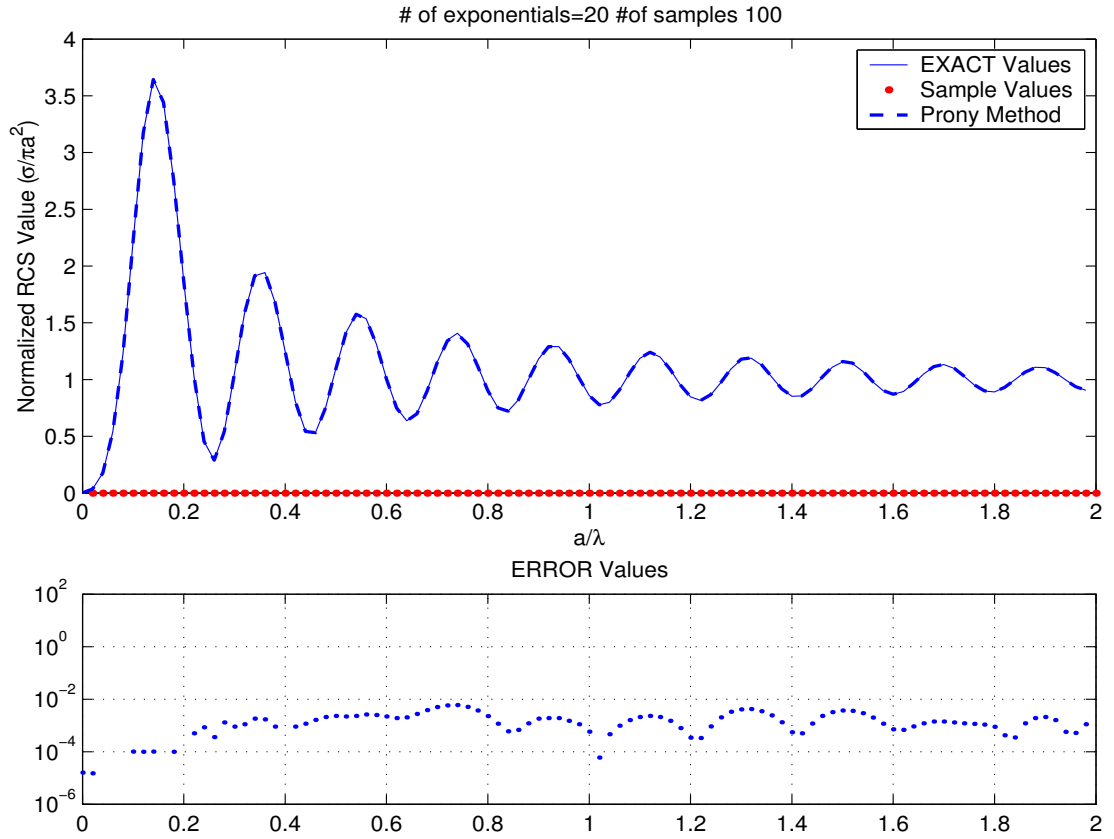


Figure 3.4: Application of the Prony's method to monostatic RCS results $M = 20$, $N = 100$, $T_s = 0.02$, Sampling interval=[0.02, 2]

exponents of each term in Table (3.1), an extrapolation is performed between $a/\lambda = 1.6$ and $a/\lambda = 2$.

Although, the performance of the Prony's method at extrapolation region is good, it does not yield results suitable to the percentage error criteria 1%. Due to this fact, we search for an alternative method, which provides better estimations at the extrapolation region.

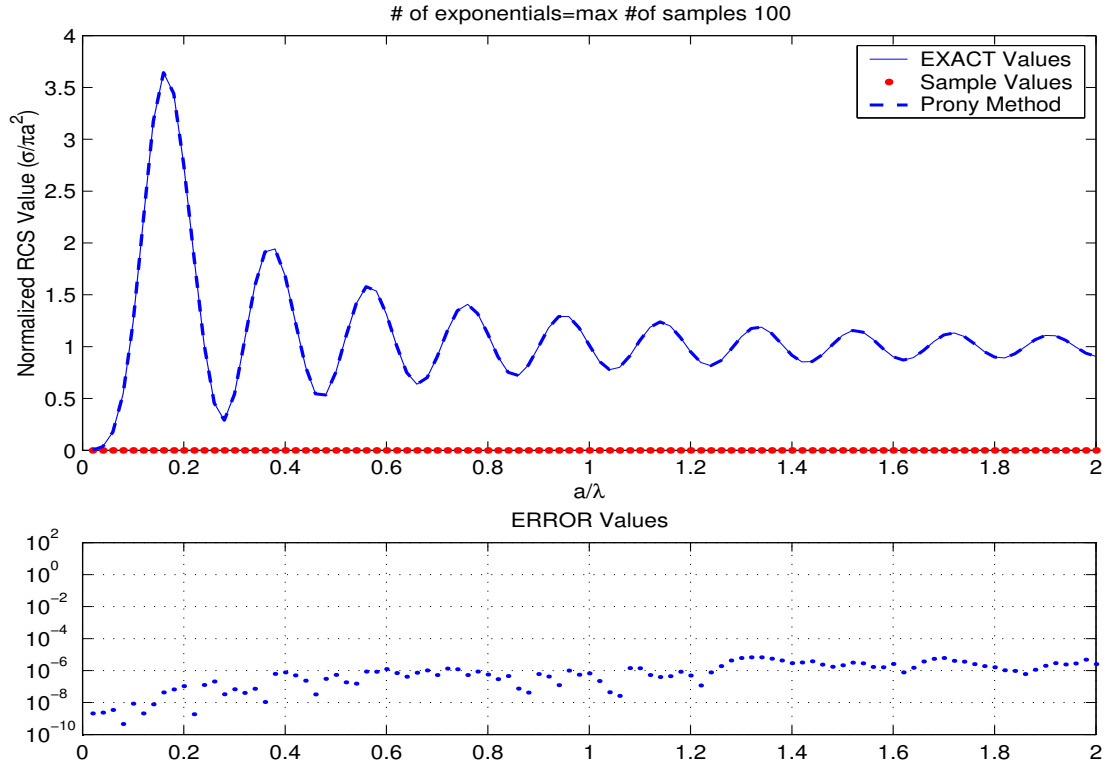


Figure 3.5: The maximum number of exponentials are used in the Prony's Method. $M = \max(49)$, $N = 100$, $T_s = 0.02$, Sampling interval=[0.02, 2]

R_i (Coefficients of Exponential Model) # Exponents=15 # samples=40		Exponents $s = -\alpha_i + j\omega_i$	
Real	Imaginary	Real	Imaginary
-3.6011e+000	-3.4897e+000	4.1072e+001	-1.3332e+001
-3.6006e+000	3.4897e+000	4.1071e+001	1.3333e+001
2.0569e-001	-1.7554e+000	8.2639e+000	-2.8686e+001
4.9029e-001	1.8148e-001	1.3490e+000	3.2673e+001
4.7643e+000	1.3826e-006	1.0123e+001	-1.8110e-007
8.9196e-003	1.9161e-001	1.2175e+001	6.6640e+001
-2.0558e-002	9.8250e-006	3.6492e+001	1.5708e+002
8.9243e-003	-1.9160e-001	1.2175e+001	-6.6640e+001
1.0931e+000	7.2800e-008	5.6673e-002	-7.9100e-008
-1.1347e-002	1.4201e-002	6.0347e+000	7.0750e+001
-1.1346e-002	-1.4203e-002	6.0347e+000	-7.0750e+001
-1.1038e-002	3.6649e-002	2.1283e+001	1.0942e+002
-1.1039e-002	-3.6640e-002	2.1283e+001	-1.0942e+002
2.0568e-001	1.7554e+000	8.2639e+000	2.8686e+001
4.9029e-001	-1.8148e-001	1.3490e+000	-3.2673e+001

Table 3.1: Solution of the Exponents and Residues in the Exponential model with Prony's Method, Number of Exponents= 15 Number of samples= 40

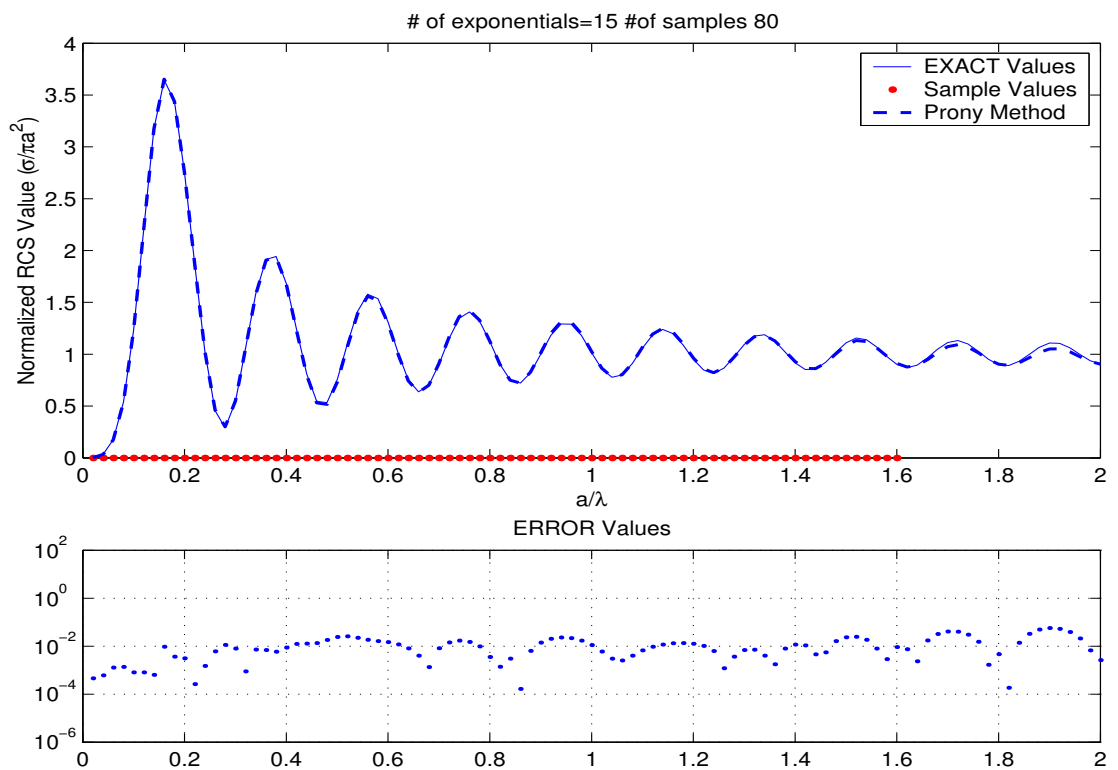


Figure 3.6: Extrapolation of RCS values in the frequency dimension. The parameters are solved with Prony's method. $M = 15$, $N = 80$, $T_s = 0.02$, Sampling interval=[0.02, 1.6]

Chapter 4

Matrix-Pencil Method

The signal model of the observed late time of electromagnetic energy-scattered response from an object in general can be formulated as,

$$y(t) = x(t) + n(t) \approx \sum_{i=1}^M R_i e^{s_i t} + n(t), \quad 0 \leq t \leq T \quad (4.1)$$

In Matrix-Pencil method, same sequence of data samples are used in achieving the parameter estimation, where

$y(t)$: observed time response

$n(t)$: noise in the system

$x(t)$: signal

$$s_i : -\alpha_i + j\omega_i \quad (4.2)$$

α_i : damping factor

ω_i : Angular frequency ($\omega_i = 2\pi f_i$)

R_i : residue or complex coefficient .

After sampling, variable, t , is replaced by kT_s , where T_s is the sampling period.

The sequence can be written as

$$y(kT_s) = x(kT_s) + n(kT_s) \approx \sum_{i=1}^M R_i z_i^k + n(kT_s) \quad \text{for} \quad k = 0, 1, \dots, N - 1 \quad (4.3)$$

and

$$z_i = e^{s_i T_s} = e^{(-\alpha_i + j\omega_i)T_s} \quad \text{for} \quad i = 1, \dots, M$$

The main problem is to find the best estimates of M , R_i 's, and z_i 's from the noise contaminated data, $y(kT_s)$. In general, simultaneous estimation of M , R_i 's, and z_i 's is a nonlinear problem.

However, solving the linear problem is interesting and, in many cases, is equivalent to solving the nonlinear problem. In addition, the solution to the linear problem can be used as an initial guess to non-linear-optimization problems.

Two of the popular linear methods to solve the parameters are the ‘‘polynomial’’ method and the ‘‘Matrix-Pencil’’ method [6]. For example, Prony’s method is polynomial type method. The basic difference between two method is that the ‘‘polynomial’’ method is a two step process in finding the poles, z_i . On the other hand, the ‘‘Matrix-Pencil’’ approach is a one-step process. The poles z_i are found as the solution of a generalized eigenvalue problem. The Matrix-Pencil technique is published in 1989, even though its roots go back to the pencil-of-function approach. The term ‘‘Pencil’’ arises when combining two functions defined on a common interval, with a scalar parameter, λ :

$$f(t, \lambda) = g(t) + \lambda h(t) \tag{4.4}$$

$f(t, \lambda)$ is called a pencil of functions $g(t)$ and $h(t)$, parameterized by λ . To avoid obvious triviality, $g(t)$ is not permitted to be a scalar multiple of $h(t)$. The pencil-of-function contains very important features about extracting information about z_i , given $y(t)$, when $g(t)$, $h(t)$ and λ are approximately selected. Also, the Matrix-Pencil method is called Generalized Pencil of Function (GPOF) method [3]. For noiseless data, we can define two $(N - L) \times L$ matrices \mathbf{Y}_1 and \mathbf{Y}_2 defined by,

$$\mathbf{Y}_2 = \begin{bmatrix} x(1) & x(2) & \cdots & x(L) \\ x(2) & x(3) & \cdots & x(L+1) \\ \vdots & \vdots & & \vdots \\ x(N-L) & x(N-L+1) & \cdots & x(N-1) \end{bmatrix}_{(N-L) \times L} \quad (4.5a)$$

$$\mathbf{Y}_1 = \begin{bmatrix} x(0) & x(1) & \cdots & x(L-1) \\ x(1) & x(2) & \cdots & x(L) \\ \vdots & \vdots & & \vdots \\ x(N-L-1) & x(N-L) & \cdots & x(N-2) \end{bmatrix}_{(N-L) \times L} \quad (4.5b)$$

where L is referred to as the pencil parameter and very useful in eliminating the some effects of noise in data. One can write

$$\mathbf{Y}_2 = \mathbf{Z}_1 \mathbf{R} \mathbf{Z}_0 \mathbf{Z}_2 \quad (4.6a)$$

$$\mathbf{Y}_1 = \mathbf{Z}_1 \mathbf{R} \mathbf{Z}_2 \quad (4.6b)$$

where

$$\mathbf{Z}_1 = \begin{bmatrix} 1 & 1 & \cdots & 1 \\ z_1 & z_2 & \cdots & z_M \\ \vdots & \vdots & & \vdots \\ z_1^{N-L-1} & z_2^{N-L-1} & \cdots & z_M^{N-L-1} \end{bmatrix}_{(N-L) \times M} \quad (4.7a)$$

$$\mathbf{Z}_2 = \begin{bmatrix} 1 & z_1 & \cdots & z_1^{L-1} \\ 1 & z_2 & \cdots & z_2^{L-1} \\ \vdots & \vdots & & \vdots \\ 1 & z_M & \cdots & z_M^{L-1} \end{bmatrix}_{M \times L} \quad (4.7b)$$

$$\mathbf{Z}_0 = \text{diag}[z_1, z_2, \dots, z_M] \quad (4.7c)$$

$$\mathbf{R} = \text{diag}[R_1, R_2, \dots, R_M] \quad (4.7d)$$

where $\text{diag}[\cdot]$ represents an $M \times M$ diagonal matrix. Now consider a matrix pencil

$$\mathbf{Y}_2 - \lambda \mathbf{Y}_1 = \mathbf{Z}_1 \mathbf{R} \{\mathbf{Z}_0 - \lambda \mathbf{I}\} \mathbf{Z}_2 \quad (4.8)$$

due to the $[R]_{M \times M}$ matrix, \mathbf{I} is an $M \times M$ identity matrix. In general, the rank of $\mathbf{Y}_2 - \lambda \mathbf{Y}_1$ will be M . However, if λ is equal to z_i , $i = 1, 2, \dots, M$, the rank of matrix is $M - 1$. Therefore, the parameters z_i may be found as the generalized eigenvalues of the matrix pair $\{\mathbf{Y}_2, \mathbf{Y}_1\}$. By using the \mathbf{Y}_1^+ Moore-Penrose pseudo-inverse of \mathbf{Y}_1 , problem of solving for z_i can be thought as an ordinary eigenvalue problem,

$$\{\mathbf{Y}_1^+ \mathbf{Y}_2 - \lambda \mathbf{I}\} \quad (4.9)$$

$\mathbf{Y}_1^+ = \{\mathbf{Y}_1^H \mathbf{Y}_1\}^{-1} \mathbf{Y}_1^H$, where the superscript ‘‘H’’ denotes the conjugate transpose. Based on the decomposition of \mathbf{Y}_1 and \mathbf{Y}_2 in Eq. (4.6a) and Eq. (4.6b), one can show that if $M \leq L \leq N - M$ the poles $z_i; i = 1, \dots, M$ are the generalized eigenvalues of the matrix pencil $\mathbf{Y}_2 - \lambda \mathbf{Y}_1$. Namely, if $M \leq L \leq N - M$, $\lambda = z_i$ is a rank reducing number of $\mathbf{Y}_2 - \lambda \mathbf{Y}_1$.

One forms the data matrix \mathbf{Y} from the noise-contaminated-data $y(t)$.

$$\mathbf{Y} = \begin{bmatrix} y(0) & y(1) & \cdots & y(L) \\ y(1) & y(2) & \cdots & y(L+1) \\ \vdots & \vdots & & \vdots \\ y(N-L-1) & y(N-L) & \cdots & y(N-1) \end{bmatrix}_{(N-L) \times (L+1)} \quad (4.10)$$

Notice that \mathbf{Y}_1 is obtained from \mathbf{Y} by deleting the last column, and \mathbf{Y}_2 is obtained from \mathbf{Y} by deleting the first column. Therefore, in the presence of noise, the matrix elements $x(k)$'s are replaced by $y(k)$ to obtain \mathbf{Y}_1 , \mathbf{Y}_2 and \mathbf{Y} . For efficient noise filtering, the parameter L is chosen between $N/3$ and $N/2$. In applications; we set $L = N/2$. After than, a singular-value decomposition (SVD) of the matrix \mathbf{Y} is carried out as

$$\mathbf{Y} = \mathbf{U} \mathbf{\Sigma} \mathbf{V}^H \quad (4.11)$$

Here, \mathbf{U} and \mathbf{V} are unitary matrices, composed of eigenvectors of $\mathbf{Y}\mathbf{Y}^{\mathbf{H}}$ and $\mathbf{Y}^{\mathbf{H}}\mathbf{Y}$, respectively, and $\mathbf{\Sigma}$ is a diagonal matrix containing the singular values of \mathbf{Y} , i.e.

$$\mathbf{U}^{\mathbf{H}}\mathbf{Y}\mathbf{V} = \mathbf{\Sigma} \quad (4.12)$$

The parameters M is chosen at this stage. One compares the various singular values with largest one. Typically, the singular values beyond M are set equal to zero. The procedure of choosing M is as follows. Consider the singular values σ_c such that

$$\frac{\sigma_c}{\sigma_{max}} \approx 10^{-n} \quad (4.13)$$

where n is the number significant decimal digits in the data. Once M and z_i 's are known, the residues, R_i , are solved from the least-squares problem:

$$\begin{bmatrix} y(0) \\ y(1) \\ \vdots \\ \vdots \\ y(N-1) \end{bmatrix} = \begin{bmatrix} 1 & 1 & \cdots & 1 \\ z_1 & z_2 & \cdots & z_M \\ \vdots & \vdots & & \vdots \\ \vdots & \vdots & & \vdots \\ z_1^{N-1} & z_2^{N-1} & \cdots & z_M^{N-1} \end{bmatrix} \begin{bmatrix} R_1 \\ R_2 \\ \vdots \\ R_M \end{bmatrix} \quad (4.14)$$

4.1 Relation between the Prony's and Matrix-Pencil Method

Given M complex number $z_i, i = 1, 2, \dots, M$ there exist unique complex numbers $a_k, k = 1, 2, \dots, M$, such that

$$1 + \sum_{k=1}^M a_k z_i^{-k} = 0 \quad \text{for } i = 1, 2, \dots, M \quad (4.15)$$

Therefore, finding the signal poles $z_i, i=1,2,\dots,M$, is equivalent to finding the coefficients $a_k, k = 1, 2, \dots, M$, of the M^{th} degree polynomial $\sum_{k=0}^M a_k z^{-k}$ (with $a_0 = 1$), which has roots at z_i . This is the essence of the original Prony method. This, however, can be generalized as follows. Finding

the signal-poles z_i 's are equivalent to finding the coefficients a_k , $k = 1, 2, \dots, L$ of an L^{th} -degree polynomial $\sum_{k=0}^L a_k z^{-k}$ (with $a_0 = 1$ and $L \geq M$), such that of all the L roots of the polynomial, there are M signal roots which are one-to-one functions of z_i 's, and which are also separable from the other $(L - M)$ (extraneous) roots, due to "over-modelling" as L is greater than M .

Let

$$p(\lambda) = \sum_{k=0}^L a_k \lambda^{-k}$$

so that $p(z_i) = 0$ for $i = 1, 2, \dots, M$. Then, it can be shown that for $L \leq m \leq N - 1$

$$\sum_{k=0}^L y_{m-k} a_k = y_m a_0 + y_{m-1} a_1 + \dots + y_{m-k} a_k + \dots + y_{m-L} a_L = 0$$

Therefore in matrix form $[Y][a] = \mathbf{0}$, where

$$\mathbf{Y} = [Y_1 : y] = \begin{bmatrix} y(0) & \dots & y(L-1) & \vdots & y(L) \\ y(1) & & y(L) & \vdots & y(L+1) \\ \vdots & & \vdots & \vdots & \vdots \\ y(N-L-1) & \dots & y(N-2) & \vdots & y(N-1) \end{bmatrix} \quad (4.16)$$

where $\mathbf{y} = [y(L), \dots, y(N-1)]^T$, and $\mathbf{a} = [a_L, \dots, a_0]^T$. Note also that

$$\mathbf{Y} = [Z_1][R][Z_2 : z]$$

with

$$[z] = [z_1^L, \dots, z_M^L]^T$$

Since the roots of polynomial are independent of the uniform scaling of the coefficients a_i , we have left a_0 be one, without any loss of information. Therefore

$$[Y][a] = -[y]$$

where $\mathbf{a} = [a_L, \dots, a_1]^T$. In digital signal processing this equation is called "forward linear prediction" equation. The minimum-norm solution, which is given

by

$$[a] = -[Y_1^+][y]$$

The link between Matrix-Pencil and Prony's method is shown below: It can be shown that the roots of Prony's $\sum_{k=0}^L a_k z^{-k}$ (with $a_0 = 1$) are the eigenvalues of the matrix

$$\mathbf{C}_1 = \begin{bmatrix} 0 & 0 & \cdots & 0 & -a_L \\ 1 & 0 & \cdots & 0 & -a_{L-1} \\ 0 & 1 & \cdots & 0 & -a_{L-2} \\ \vdots & \vdots & & \vdots & \vdots \\ 0 & 0 & \cdots & 1 & -a_1 \end{bmatrix}_{L \times L} = [\mathbf{U}_2, \mathbf{U}_3, \dots, \mathbf{U}_L, \mathbf{Y}_1^+ \mathbf{y}], \quad (4.17)$$

where \mathbf{U}_i is the $(L \times 1)$ vector with the i^{th} element equal to 1 and all other elements zero. $\mathbf{Y}_1^+ \mathbf{Y}_2$ can be written as

$$\mathbf{C}_2 = \mathbf{Y}_1^+ \mathbf{Y}_2 = [\mathbf{Y}_1^+ \mathbf{y}_1, \mathbf{Y}_1^+ \mathbf{y}_2, \dots, \mathbf{Y}_1^+ \mathbf{y}_L]$$

with $\mathbf{y}_k = [y_k, \dots, y_{k+N-L-1}]^T$, where $k = 1, \dots, L$. As we can see, the i^{th} column of \mathbf{C}_2 is a solution of the following equation:

$$[Y_1][b] = [y_i] \quad (4.18)$$

But in \mathbf{C}_1 , only the last column vector is the minimum-norm solution with $i = L$, while in \mathbf{C}_2 , all column vectors are minimum-norm solutions of Equation (4.18).

4.2 Applications of the Matrix-Pencil Method

In this section, the estimation of RCS values with the Matrix-Pencil method is presented. The Matrix-Pencil Method is designed for the estimation of general type systems. But RCS solutions have some specific features, such as, high-frequency RCS of an object converges to its cross-section area. Also, we already know that the calculation of RCS at high frequencies is consuming much CPU time. We have done some modifications in the Matrix-Pencil method to adapt to the RCS calculations.

4.2.1 Natural Matrix-Pencil Method

Prony's method has been presented in the previous chapter. In order to clarify the superiority of Matrix-Pencil method, two illustrations are explained with the

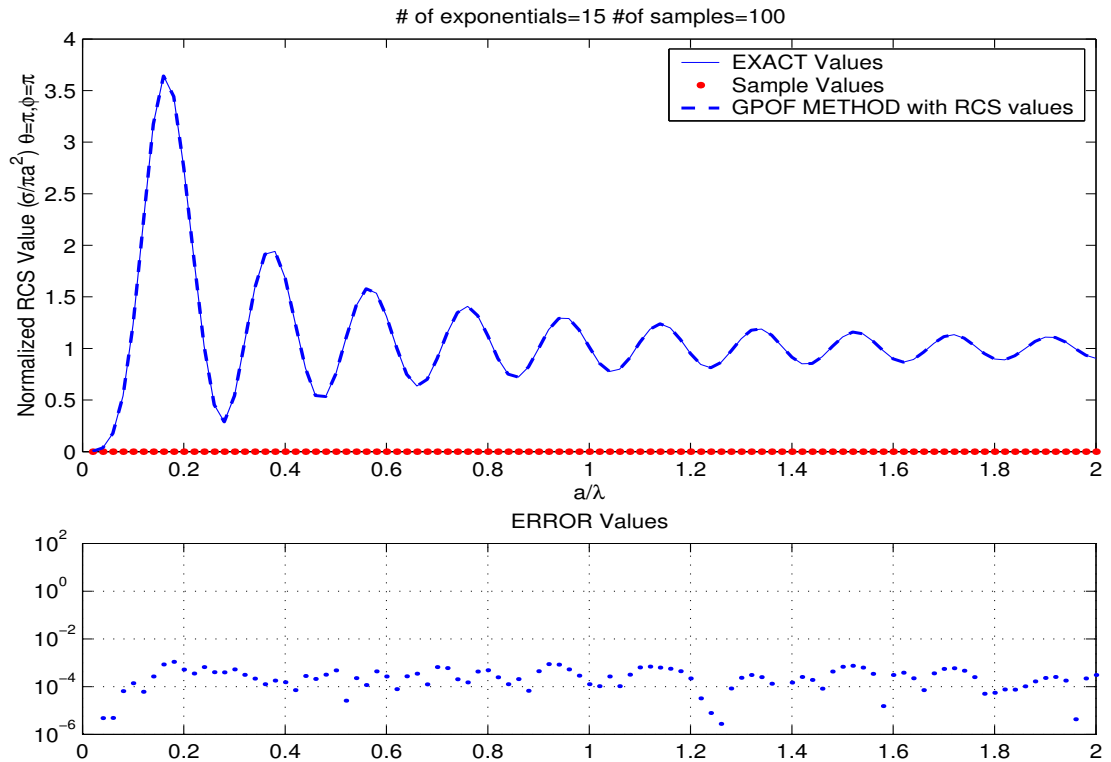


Figure 4.1: Application of the Matrix-Pencil method to monostatic RCS results $M = 15$, $N = 100$, $T_s = 0.02$, Sampling interval= $[0.02, 2]$

same conditions used in Prony's method. The parameters of these two solutions, results of which are shown in Fig. 4.1 and Fig. 3.3, are the same.

If we look at the interpolation error plots of the Fig. 4.1 and Fig. 3.3, we can see the superiority of Matrix-Pencil method. Also, the error results of monostatic RCS at high frequencies imply the relative error, because normalized RCS value converges to 1. Both in the interpolation and extrapolation regions, Matrix-Pencil method estimations come closer to the exact solutions of RCS. Likewise, Fig. 4.2 is analogous to Fig. 3.6.

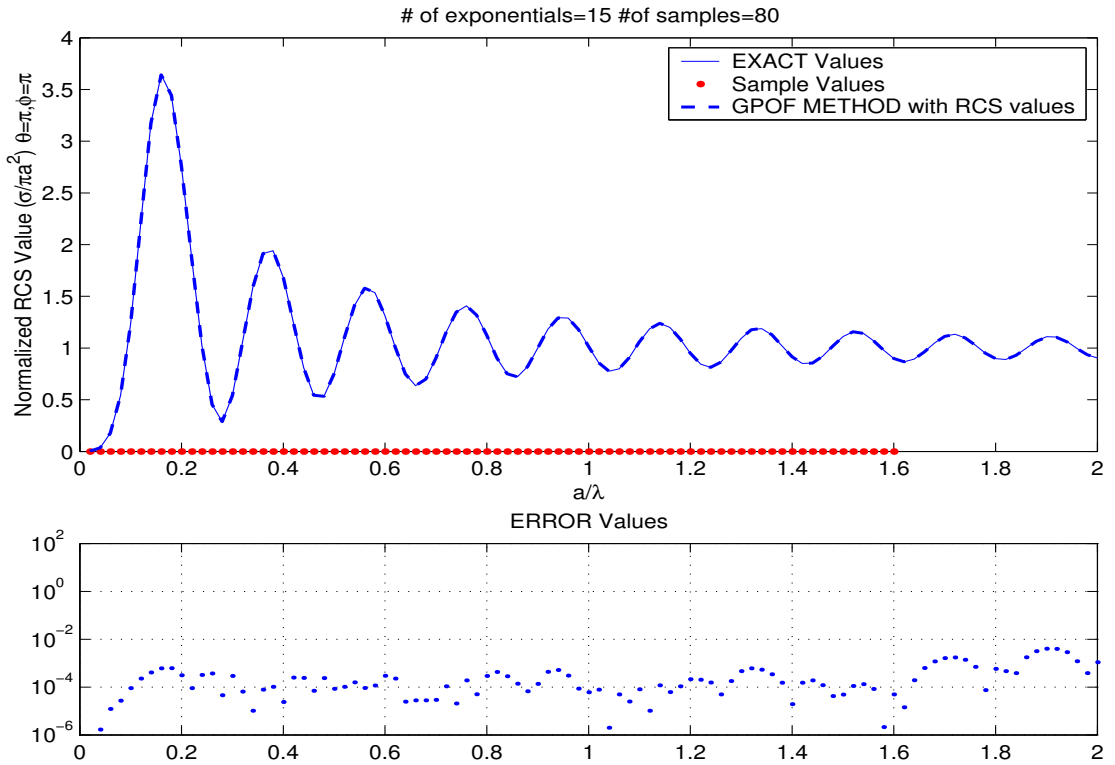


Figure 4.2: Extrapolation of the monostatic RCS values with Matrix-Pencil method. $M = 15$, $N = 80$, $T_s = 0.02$, Sampling interval= $[0.02, 1.6]$. Extrapolation is performed until $a/\lambda = 2$

According to these figures, we can conclude that the extrapolation performance of Matrix-Pencil method is better than Prony's performance. After this conclusion, we have tested Matrix-Pencil by using different parameter values.

In the monostatic case, if we look at the shape of the RCS curve, we observe that the amplitude and variety of the interval $a/\lambda = 0$ to $a/\lambda = 0.4$ is greater

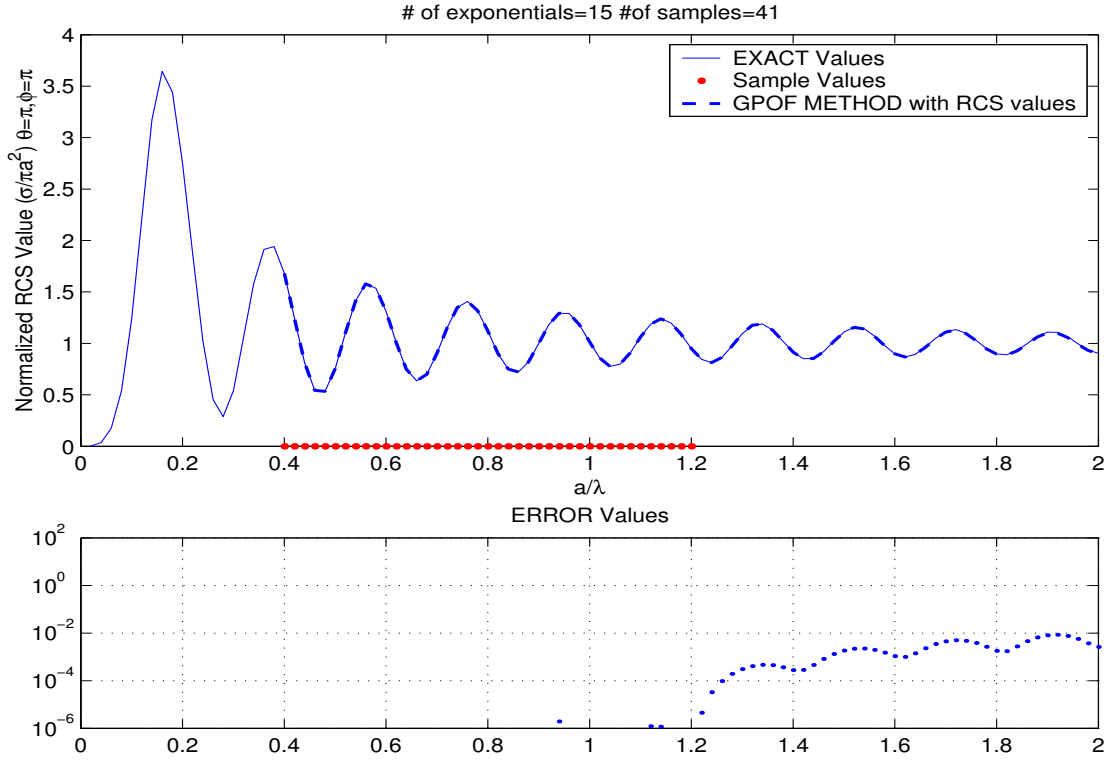


Figure 4.3: Extrapolation of the monostatic RCS values with using less sampled data. The number of exponentials (M) is still 15, $N = 41$, $T_s = 0.02$, Sampling interval= $[0.02, 1.2]$

than the high frequency (optical) region. Taking this feature into consideration, we have excluded the interval $[0, 0.4]$ from the sampled data.

In Fig. 4.3, we have begun sampling from $a/\lambda = 0.4$ to $a/\lambda = 1.2$. Notice that the end point of sampled data was also decreased to extrapolate more RCS values without using analytical expressions. This modification improves both interpolation and extrapolation results as seen from the Fig. 4.3 in the bottom plot.

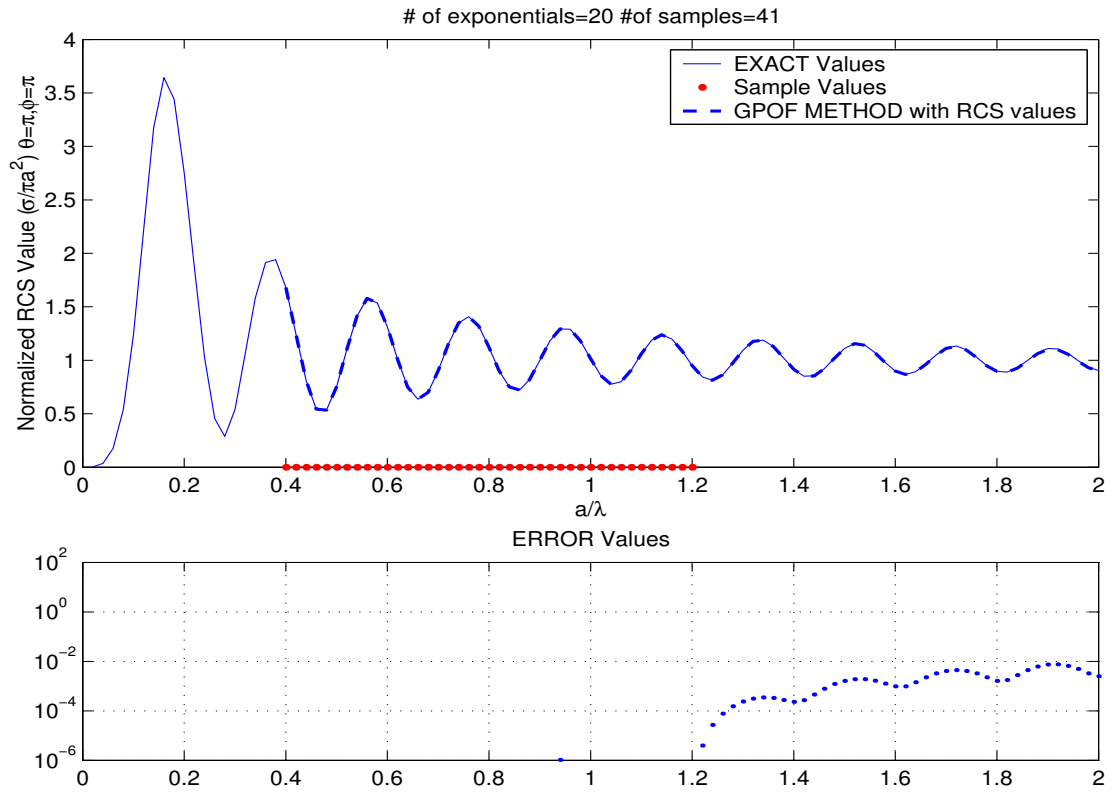


Figure 4.4: Application of the Matrix-Pencil Method to monostatic RCS results $M = 20$, $N = 41$, $T_s = 0.02$, Sampling interval= $[0.02, 1.2]$

In Fig. 4.4, only the number of terms is changed from 15 to 20. In this figure, Matrix-Pencil method is used with its maximum number of terms, according to this, the error values are decreased. However, it does not yield any considerable improvement in the extrapolation region.

Based on the importance of the prediction at high-frequency values, in Fig. 4.5,

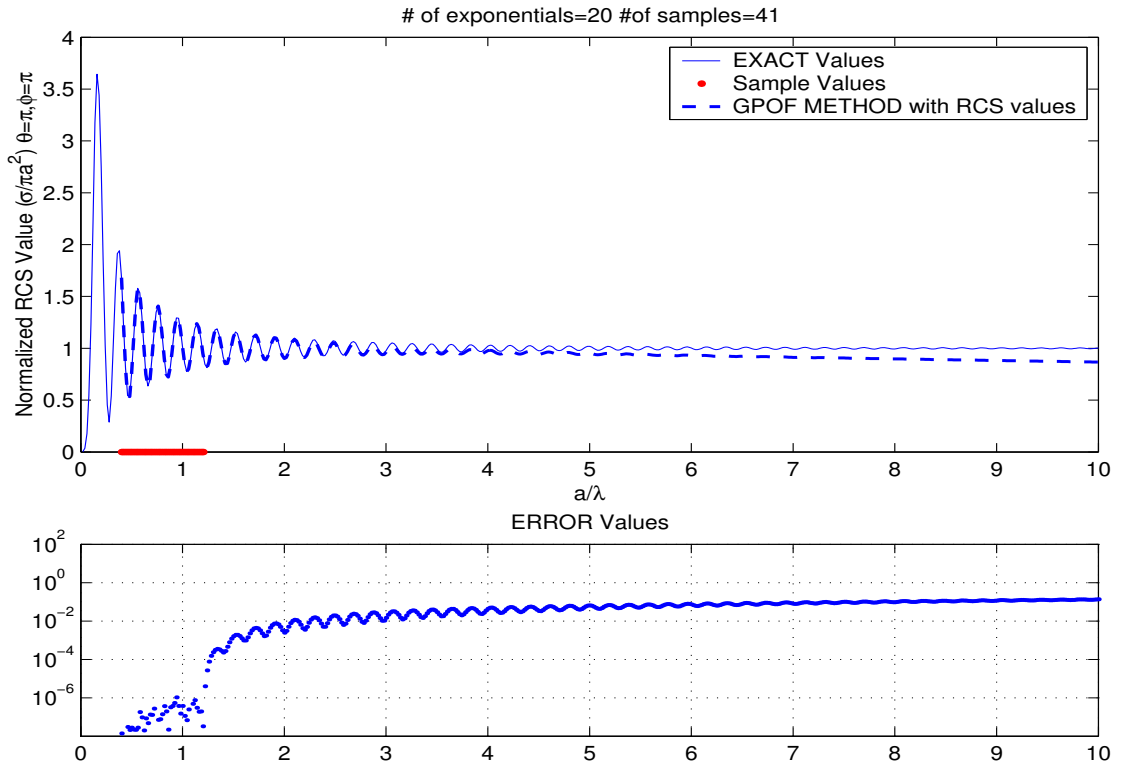


Figure 4.5: The extrapolation is extended up to $a/\lambda = 10$. Application of the Matrix-Pencil Method to monostatic RCS results $M = 20$, $N = 41$, $T_s = 0.02$, Sampling interval=[0.02, 1.6]

we have made an extrapolation until $a/\lambda = 10$. After $a/\lambda = 2$, the results is not acceptable according to the percentage error criteria of 1%.

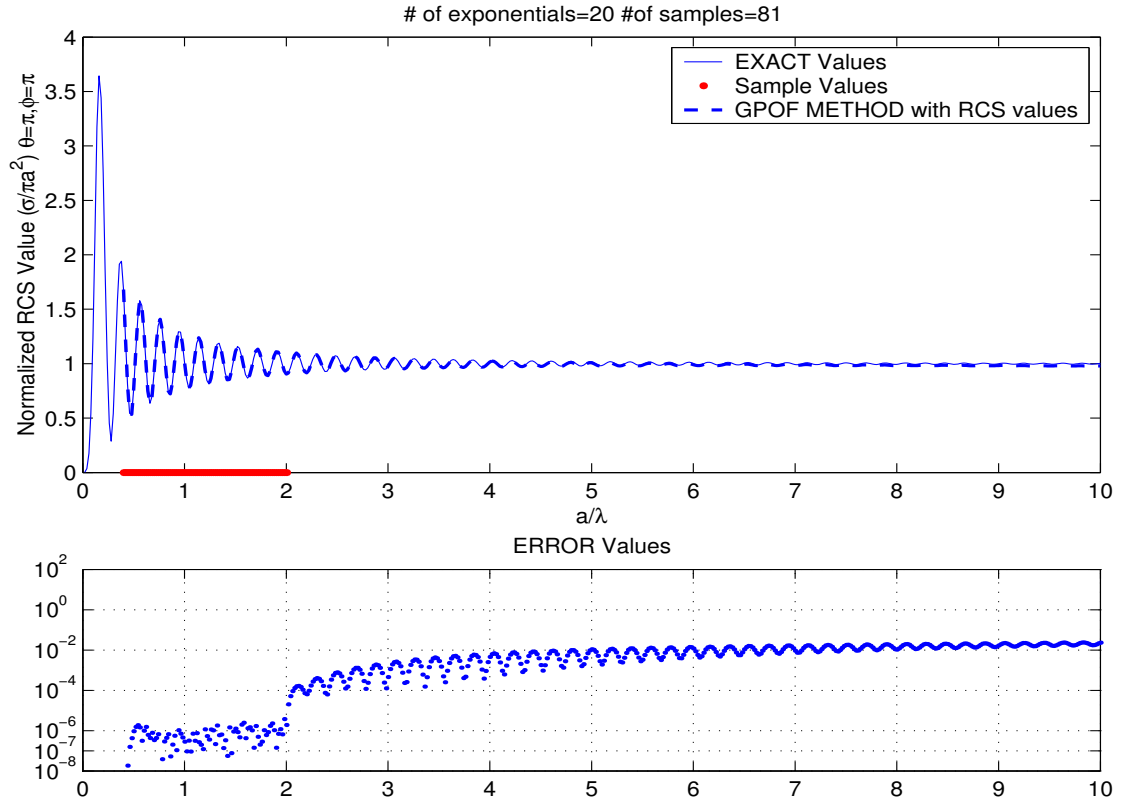


Figure 4.6: The error values are shown at the bottom plot with logarithmic scale. Application of the Matrix-Pencil Method to monostatic RCS results $M = 20$, $N = 81$, $T_s = 0.02$, Sampling interval= $[0.4, 1.6]$

Furthermore, In Fig. 4.6, the number of terms is still 20, but we have included the interval $[1.6, 2]$ to sampled data, as a result N is taken as 81. Between $a/\lambda = 0.4$ and $a/\lambda = 2$, which is the interpolation region, the Matrix-Pencil Method yields error values in the vicinity of 10^{-6} . By using low-frequency values of RCS, we can make a prediction with an acceptable range until $a/\lambda = 5$ as seen from the bottom plot of the Fig. 4.6.

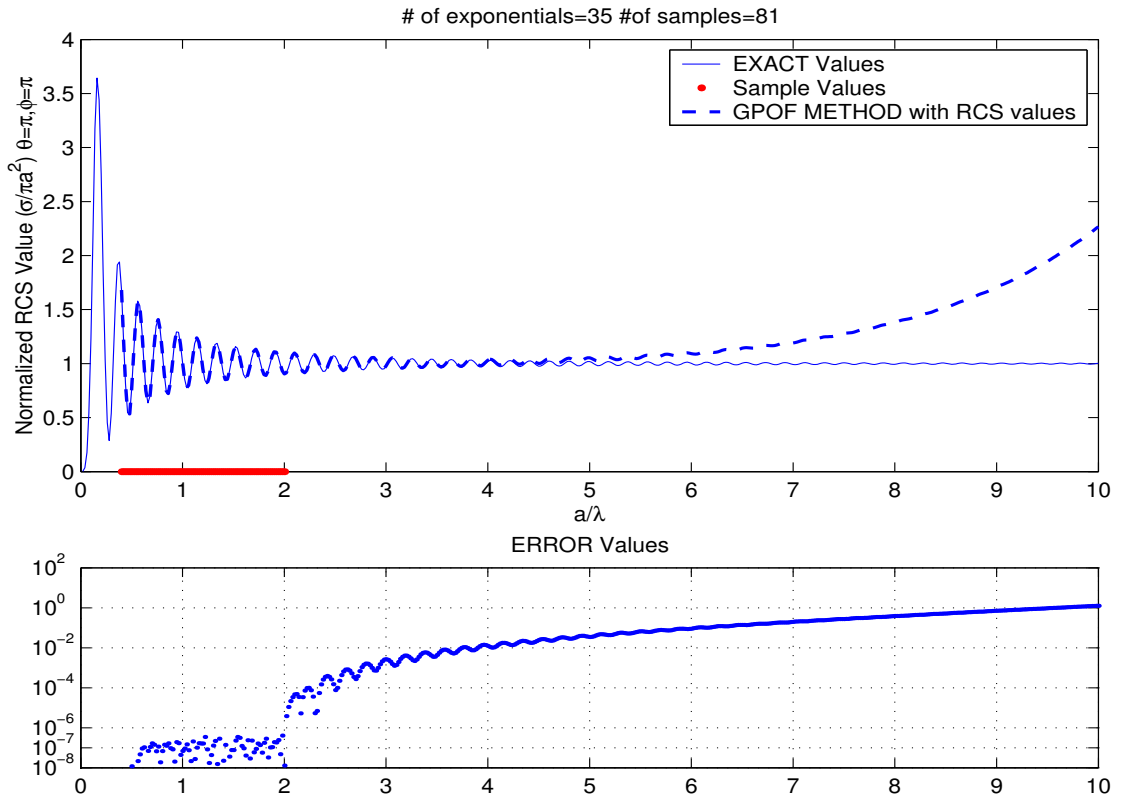


Figure 4.7: Application of the Matrix-Pencil Method to monostatic RCS results $M = 35$, $N = 81$, $T_s = 0.02$, Sampling interval= $[0.4, 1.6]$

In Figure 4.7, the number of terms is increased from $M = 20$ to $M = 35$. In this case, the interpolation error is decreased, but at high frequencies $a/\lambda \geq 4$ we have observed a growing curve at extrapolation. Actually, this growing curve arises from the dominant negative damping factors (α).

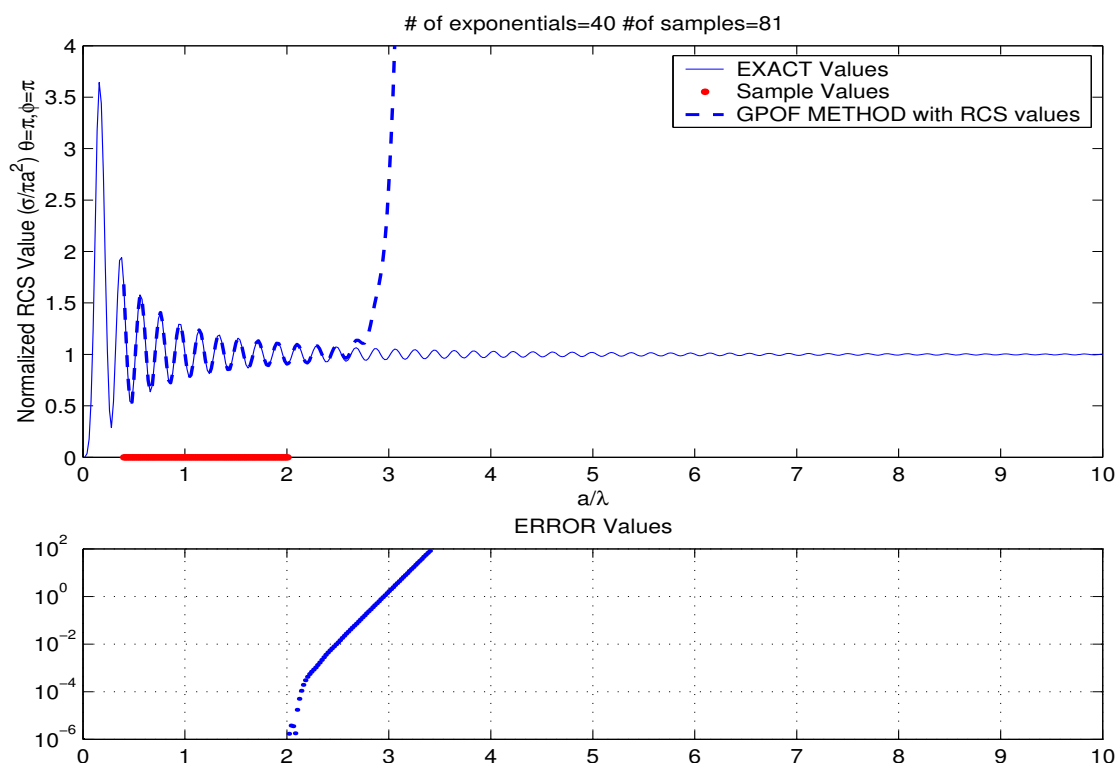


Figure 4.8: The maximum number of exponentials is used ($M = 40$). Application of the Matrix-Pencil Method to monostatic RCS results , $N = 80$, $T_s = 0.02$, Sampling interval=[0.02, 1.6]

Table 4.1 illustrates the solution of coefficients and exponents. The negative α 's and the relevant terms are written in boldface. In Figure 4.8, we have changed the number of terms from 35 to 40. Increasing the number of terms makes an improvement at the interpolation, but it places too much stress on exponents. In the following sections, we investigate a modification to remove the effects of these negative damping factors.

Singular values	α	ω	$\Re(\mathbf{R})$	$\Im(\mathbf{R})$	$ \mathbf{R} $
1. 4.136e+001	-1.9342e-001	1.3600e+002	-1.8936e-008	5.8864e-008	6.1835e-008
2. 5.184e+000	-1.9342e-001	-1.3600e+002	-1.8936e-008	-5.8864e-008	6.1835e-008
3. 5.158e+000	8.1006e-002	1.5708e+002	2.3044e-007	-1.9630e-016	2.3044e-007
4. 3.6297e-001	2.9508e+000	1.5319e+002	4.8376e-007	-5.2137e-007	7.1123e-007
5. 2.1987e-001	2.9508e+000	-1.5319e+002	4.8376e-007	5.2137e-007	7.1123e-007
6. 2.0108e-001	1.5899e+000	1.1012e+002	-2.9368e-007	-6.9867e-007	7.5788e-007
7. 1.4316e-002	1.5899e+000	-1.1012e+002	-2.9368e-007	6.9867e-007	7.5788e-007
8. 7.9102e-003	2.2880e-001	1.0778e+002	-1.8027e-007	1.9168e-007	2.6313e-007
9. 5.8604e-003	2.2880e-001	-1.0778e+002	-1.8027e-007	-1.9168e-007	2.6313e-007
10. 4.6608e-003	2.0154e+001	1.2462e+002	1.0143e-005	1.4355e-005	1.7577e-005
11. 4.2487e-003	2.0154e+001	-1.2462e+002	1.0143e-005	-1.4355e-005	1.7577e-005
12. 1.0107e-003	4.5918e-003	8.7113e+001	-1.4717e-007	-1.5333e-008	1.4797e-007
13. 6.8345e-004	4.5918e-003	-8.7113e+001	-1.4717e-007	1.5333e-008	1.4797e-007
14. 3.2095e-004	2.8084e+000	7.2927e+001	2.1571e-004	-8.1360e-005	2.3054e-004
15. 3.1183e-004	2.8084e+000	-7.2927e+001	2.1571e-004	8.1360e-005	2.3054e-004
16. 1.8904e-004	5.8880e+000	7.2152e+001	7.1104e-004	-9.1674e-004	1.1602e-003
17. 9.9275e-005	5.8880e+000	-7.2152e+001	7.1104e-004	9.1674e-004	1.1602e-003
18. 2.1924e-005	9.2517e+000	7.1109e+001	-7.8813e-004	-7.3480e-004	1.0775e-003
19. 1.1929e-005	9.2517e+000	-7.1109e+001	-7.8813e-004	7.3480e-004	1.0775e-003
20. 9.2148e-006	-8.9395e-001	5.9412e+001	-6.6271e-008	6.5261e-008	9.3010e-008
21. 7.1315e-006	-8.9395e-001	-5.9412e+001	-6.6271e-008	-6.5261e-008	9.3010e-008
22. 6.2892e-006	-5.2942e-001	0	8.6446e-003	1.1790e-016	8.6446e-003
23. 5.8014e-006	1.4956e-002	0	1.0069e+000	-3.2618e-016	1.0069e+000
24. 5.1444e-006	3.3963e+000	0	1.0231e-001	1.1575e-015	1.0231e-001
25. 4.9580e-006	9.3205e+000	0	5.1610e-002	-3.6520e-016	5.1610e-002
26. 4.9420e-006	1.3746e+000	1.2715e+001	-1.1823e-004	-1.6427e-005	1.1937e-004
27. 3.9020e-006	1.3746e+000	-1.2715e+001	-1.1823e-004	1.6427e-005	1.1937e-004
28. 3.5676e-006	9.5897e+000	3.2424e+001	1.9125e-003	2.8396e-002	2.8460e-002
29. 3.2510e-006	9.5897e+000	-3.2424e+001	1.9125e-003	-2.8396e-002	2.8460e-002
30. 2.4436e-006	4.6055e+000	3.3407e+001	4.8547e-002	5.7146e-002	7.4983e-002
31. 2.2627e-006	4.6055e+000	-3.3407e+001	4.8547e-002	-5.7146e-002	7.4983e-002
32. 2.0154e-006	5.4222e-001	3.2661e+001	5.7596e-002	8.4852e-002	1.0255e-001
33. 1.6865e-006	5.4222e-001	-3.2661e+001	5.7596e-002	-8.4852e-002	1.0255e-001
34. 1.4683e-006	1.9089e+000	3.2877e+001	1.4745e-001	8.8223e-002	1.7183e-001
35. 1.4312e-006	1.9089e+000	-3.2877e+001	1.4745e-001	-8.8223e-002	1.7183e-001

Table 4.1: Solution of the Matrix-Pencil method; exponents and residues $N = 81$, Interpolation region= $[0.4, 2]$, Extrapolation region= $[2, 10]$, Sampling period, $T_s = 0.02$.

4.2.2 Choice of the Parameters in the Matrix-Pencil Method

In the flowchart of Fig. 4.9, the basic steps of the Matrix-Pencil method are illustrated. In the first step the parameters, M and L are not chosen arbitrarily. L is a parameter that determines the number of columns for \mathbf{Y}_1 and \mathbf{Y}_2 matrices. The optimal choice of L is equal to $N/2$ [3]. After setting $L = N/2$, M must be in a range $0 \leq M \leq N/2$ (Note the inequality $M \leq L \leq N - M$).

One can set M according to Eq. (4.19) by looking at the list of singular values

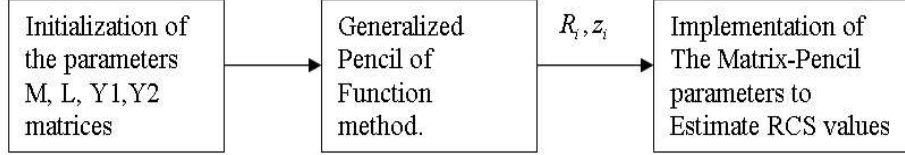


Figure 4.9: Flowchart of the Matrix-Pencil algorithm.

in Table 4.1, which are displayed in descending order;

$$\frac{\sigma_c}{\sigma_{max}} \approx 10^{-n}, \quad (4.19)$$

where the subscript c denotes the row location of singular values, and n is the degree of the error at the interpolation region [0.4, 2]. For example, in Table. 4.1, we have used $N = 81$ uniformly sampled data. According to this data, the number of exponentials must be in a range $0 \leq M \leq 40$.

The ratio of the singular values (σ_c) to the first singular value (σ_{max}) also implies the degree of the error in the the interpolation region, when the row number of the chosen singular value is the same as the number of exponentials (M). Briefly, if M is equal to c , then degree of the error is equal to $\frac{\sigma_c}{\sigma_{max}} \approx 10^{-n}$. For example, the maximum singular value is

$$\sigma_{max} = 4.13 \times 10^1.$$

The singular values at the 20th row and last row are

$$\sigma_{20} = 9.21 \times 10^{-6}, \quad \sigma_{35} = 1.4 \times 10^{-6}.$$

The related ratios of these singular values are

$$\frac{\sigma_{20}}{\sigma_{max}} = \frac{9.21 \times 10^{-6}}{4.13 \times 10^1} = 2 \times 10^{-7}, \quad \frac{\sigma_{35}}{\sigma_{max}} = \frac{1.4 \times 10^{-6}}{4.13 \times 10^1} = 3 \times 10^{-8}.$$

If we choose the number of exponentials as $M = 35$, we will obtain an error in the interpolation region in the order of $10^{-8} \sim 10^{-7}$, as shown in Fig. 4.7. In case of $M = 20$, simulation results yield an error range approximately $10^{-7} \sim 10^{-6}$ in the interval $[0.4, 2]$, as shown in Fig. 4.6. The drift between the ratios and the interpolation errors can be due to the insufficient precision of the numbers.

As a result, these ratios give us an intuition about the accuracy of the interpolation. Also, this singular value check provides a flexibility to adjust the interpolation error by considering only the singular values and without making any simulations. However, if the adjustment is done only by considering the interpolation results, a deviation (growing curve) can be observed in the extrapolation region. In the following sections, this difficulty is solved by eliminating the growing exponentials.

4.2.3 Elimination of the Growing Exponentials

In this section, an improvement will be presented in the Matrix-Pencil simulations. In Fig. 4.7 and Fig. 4.6, one can see the convergence of the interpolation error results to 0, when the number of terms is increased. However, increasing the number of terms leads to deviations in the extrapolation results. When we investigate the list of the exponents and complex coefficients (R) in Table 4.1, we see that some of the damping factors (α_i) are negative. In the exponential model

$$y(kT_s) = \sum_{i=1}^M R_i z_i^k = R_1 e^{(-\alpha_1 + j\omega_1)kT_s} + \dots + R_M e^{(-\alpha_M + j\omega_M)kT_s}, \quad (4.20)$$

the damping factor with a negative sign yields a growing term in the overall summation.

For example, five growing exponentials present in Fig. 4.7 are plotted separately

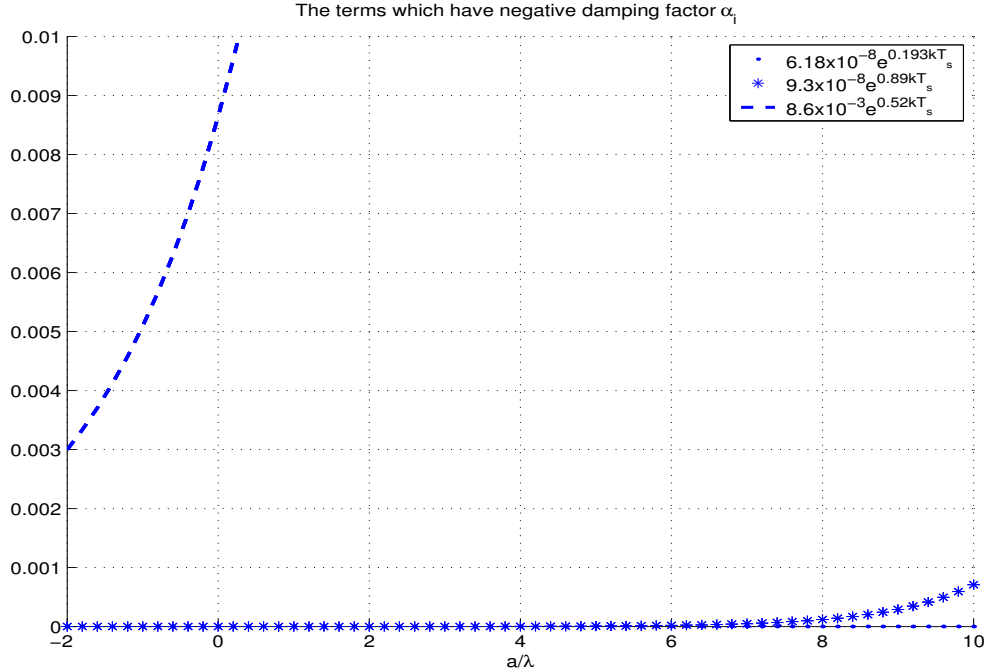


Figure 4.10: Growing exponentials present in Fig. 4.7 are plotted separately.

in Fig. 4.10. Actually, in this figure, three exponential plots are seen. Notice that in Fig. 4.10, the terms that have complex conjugate pairs are plotted as a single term. If we look at the exact values of RCS at higher frequencies, we can observe a convergence of the curve to 1. Before the implementation of interpolation or extrapolation, the negative damping factors (α_i) are replaced with 0 to reduce the effect of the growing exponentials as follows;

$$z_i = \begin{cases} R_i e^{(j\omega_i)kT_s} & \text{if } \alpha_i \leq 0 \\ R_i e^{(-\alpha_i + j\omega_i)kT_s} & \text{if } \alpha_i \geq 0 \end{cases} \quad (4.21)$$

If we compare Fig. 4.7 to Fig. 4.11, the improvement in the extrapolation region can be easily seen. On the other hand, in the interpolation region, a distortion can be observed by looking at the bottom plot of Fig. 4.11. This modification is a partial remedy for this problem. Furthermore, in the next

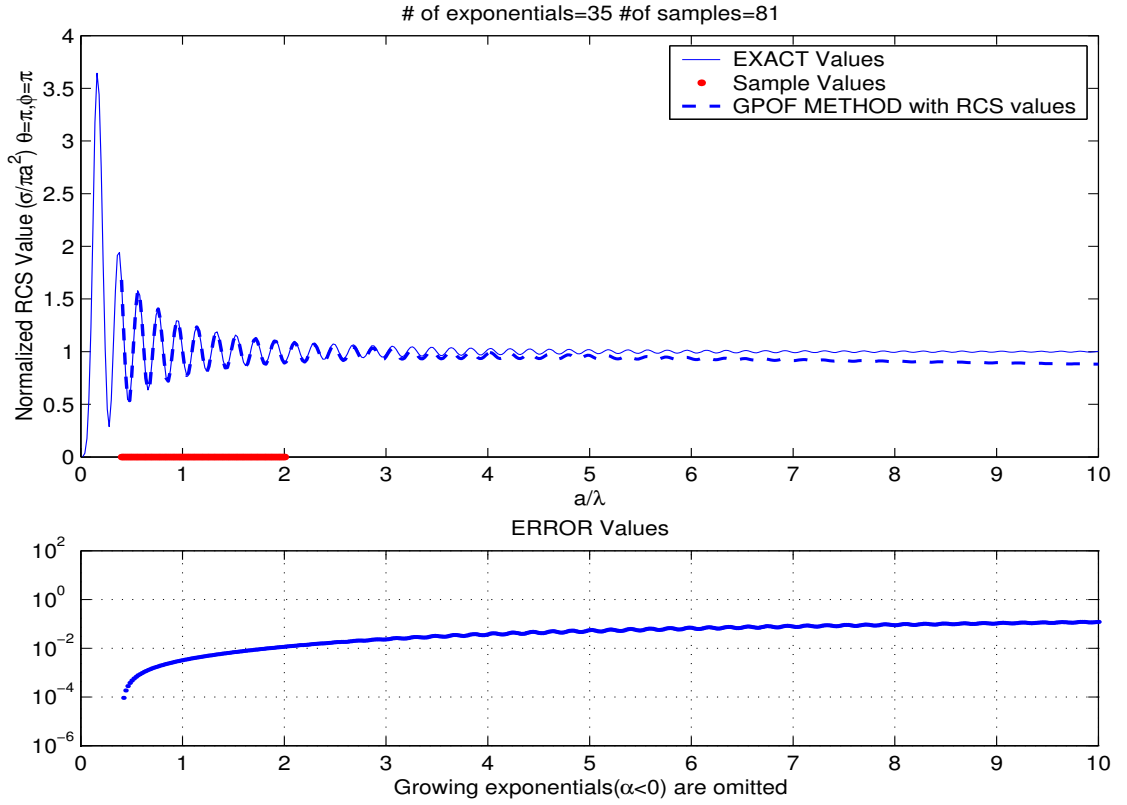


Figure 4.11: The elimination of the growing exponentials from monostatic RCS results with $M = 35$, $N = 81$, $T_s = 0.02$ and sampling interval= $[0.4, 2]$.

section, a modification is also applied to the residues of the exponential model before the implementation of the extrapolation or interpolation of the RCS curve.

4.2.4 Generation of the Residues with the New Set of Exponentials

In the previous section, the elimination of the growing exponentials are demonstrated. As a result, the set of poles (z_i) used in the estimation is changed. Elimination of the negative damping factor (α_i) gives us an opportunity to increase the number of exponentials freely. So in Fig. 4.12, we have selected the maximum number of terms as 40.

In the flowchart of the Matrix-Pencil method, in Fig. 4.9, the output of the second box yields two sets of parameters. In the previous section the set

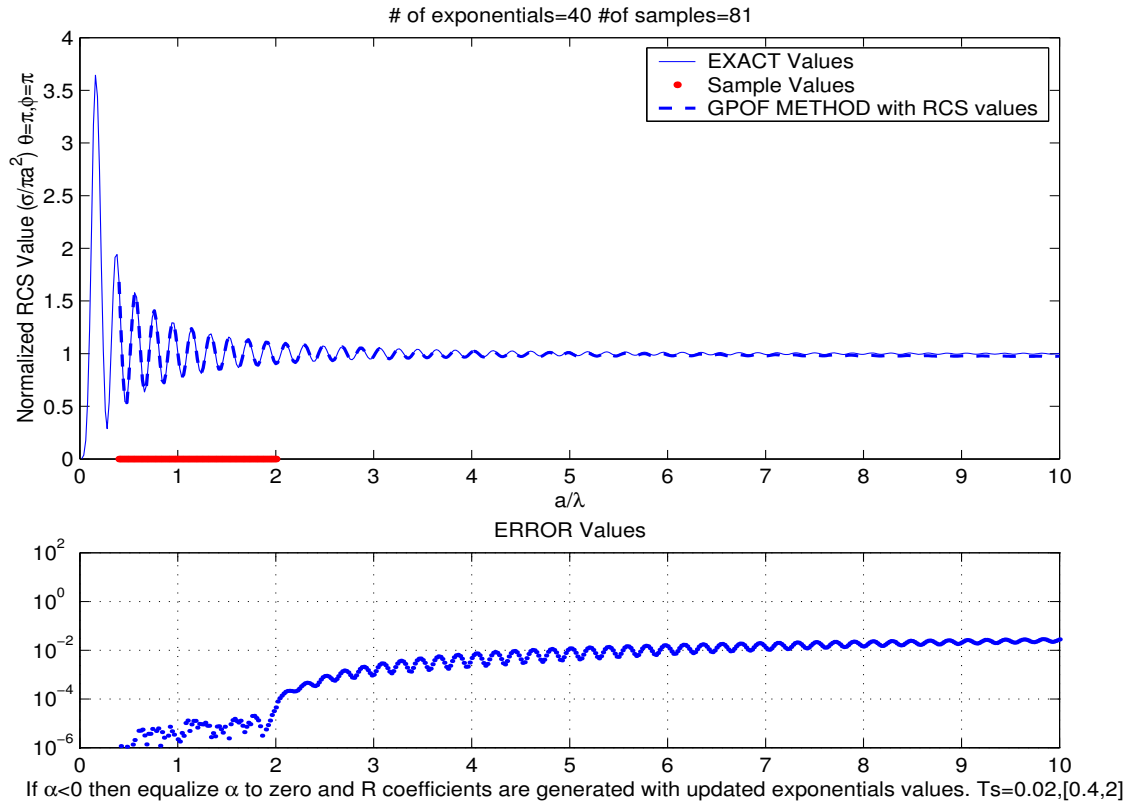


Figure 4.12: Generation of the residues with the new set of exponentials with $M = 40$, $N = 81$, $T_s = 0.02$ and sampling interval= $[0.4, 2]$.

of exponentials is changed before the implementation, but the residues (R) are still the same. But, in this section, we have also updated the residues (R) before the interpolation and the extrapolation of the RCS values. In fact, this update operation enforces the estimation of sampled data with a new set of exponents. The flowchart of the Matrix-Pencil method with its modification is plotted with

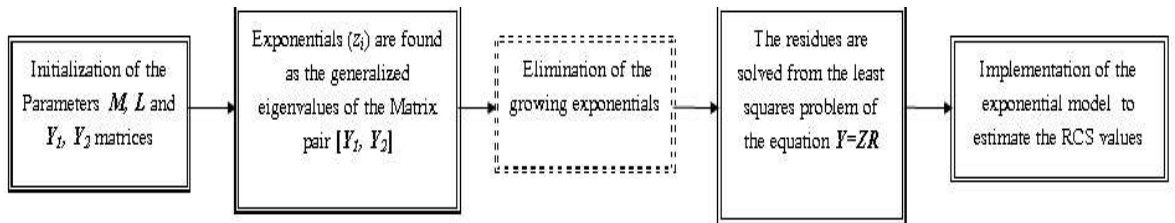


Figure 4.13: Flowchart of the elimination of the growing exponentials.

dashed-line rectangular box in Fig. 4.13. Notice that the improvement in the interpolation region $[0.4, 2]$ and the extrapolation region $[2, 10]$ can be easily seen by comparing Fig. 4.11 and Fig. 4.12.

Chapter 5

Multi-Scale Matrix-Pencil Method

In this chapter, a method is investigated to estimate the RCS values by using fewer number of sampled data and with better error range. A better algorithm is developed with respect to the previous ones on the basis of the Matrix-Pencil method. This algorithm provides a better estimation of the RCS results with fewer number of sampled data (N). The steps of this method are explained below.

Firstly, we begin uniformly sampling the RCS values with two different sampling periods $T_{s_d} = 0.02$ and $T_{s_w} = 0.04$ as shown in Fig. 5.1.

First data set is created from the interval $[0.4, 1.2]$ with $T_{s_d} = 0.02$. And the second one is created from $[0.4, 2]$ with $T_{s_w} = 0.04$. According to these two

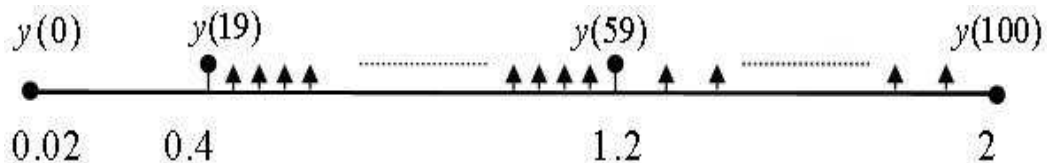


Figure 5.1: Sampling procedure of the Multi-scale GPOF

sets of data values, two different generalized eigenvalue solutions are performed, which are also shown in the branches of the flowchart in Fig. 5.2.

$$\begin{bmatrix} y(0) \\ y(1) \\ \vdots \\ \vdots \\ y(40) \end{bmatrix} = \begin{bmatrix} 1 & 1 & \cdots & 1 \\ z_{d_1} & z_{d_2} & \cdots & z_{d_{20}} \\ \vdots & \vdots & & \vdots \\ \vdots & \vdots & & \vdots \\ z_{d_1}^{40} & z_{d_2}^{40} & \cdots & z_{d_1}^{40} \end{bmatrix} \begin{bmatrix} R_{d_1} \\ R_{d_2} \\ \vdots \\ R_{d_{20}} \end{bmatrix} \quad (5.1)$$

Equations (5.1) and (5.2) are designed for the solutions of least-squares problems from the first data set and second data set, respectively.

$$\begin{bmatrix} y(0) \\ y(2) \\ \vdots \\ \vdots \\ y(80) \end{bmatrix} = \begin{bmatrix} 1 & 1 & \cdots & 1 \\ z_{w_1} & z_{w_2} & \cdots & z_{w_{20}} \\ \vdots & \vdots & & \vdots \\ \vdots & \vdots & & \vdots \\ z_{w_1}^{40} & z_{w_2}^{40} & \cdots & z_{w_1}^{40} \end{bmatrix} \begin{bmatrix} R_{w_1} \\ R_{w_2} \\ \vdots \\ R_{w_{20}} \end{bmatrix} \quad (5.2)$$

Furthermore, these two set of poles (z_d, z_w) are synthesized to perform a least squares problem in Eq. (5.3). For example, in Fig. 4.12, individually, $M_d = 20$, $M_w = 20$ and $M_{total} = 40$ poles are generated with generalized eigenvalue solution

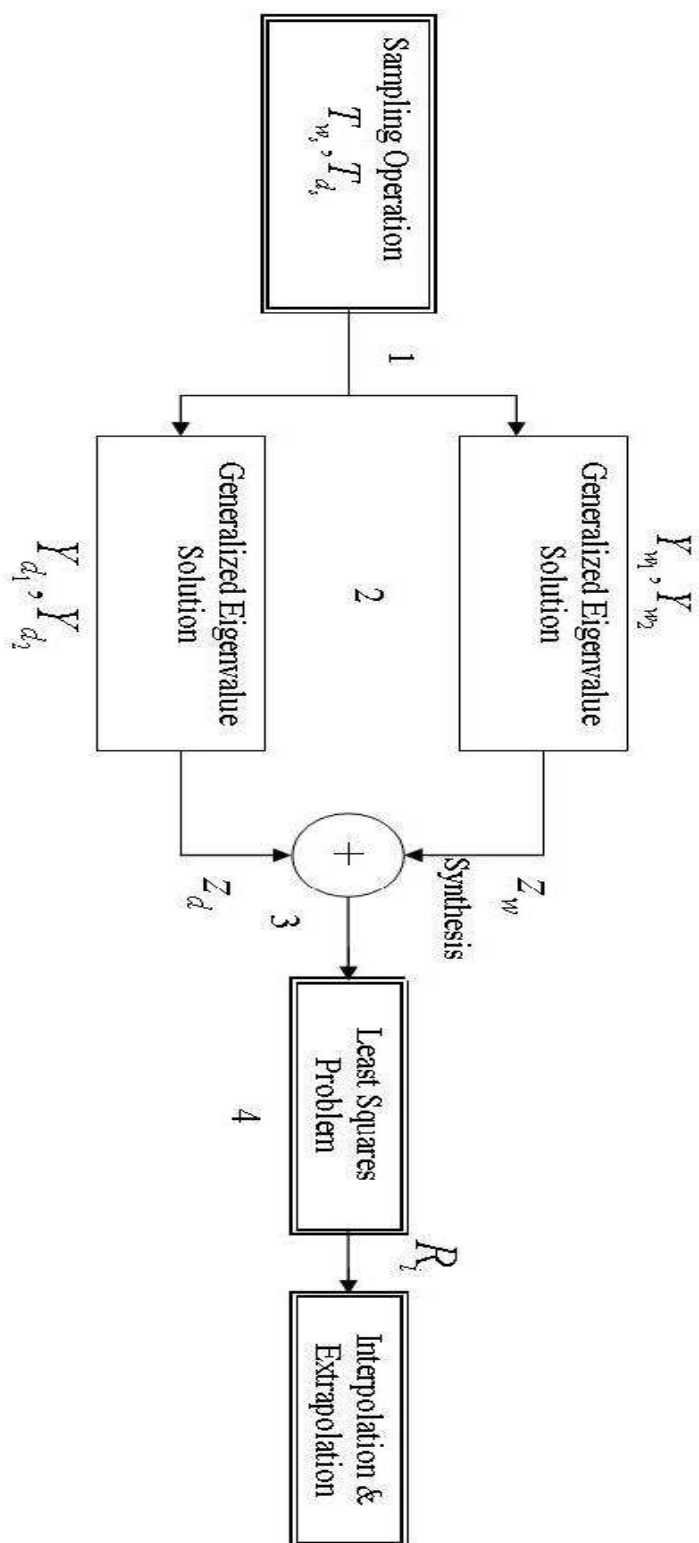


Figure 5.2: Flowchart of the Multi-scale GPOF

from the first and second data set.

$$\begin{bmatrix} y(0) \\ y(1) \\ y(2) \\ \vdots \\ \vdots \\ y(39) \\ y(40) \\ y(42) \\ y(44) \\ \vdots \\ \vdots \\ y(78) \\ y(80) \end{bmatrix} = \begin{bmatrix} 1 & 1 & \cdots & 1 & 1 & \cdots & 1 \\ z_{d_1} & z_{d_2} & \cdots & z_{d_{20}} & z_{w_1} & \cdots & z_{w_{20}} \\ \vdots & \vdots & & \vdots & \vdots & & \vdots \\ \vdots & \vdots & & \vdots & \vdots & & \vdots \\ z_{d_1}^{40} & z_{d_2}^{40} & \cdots & z_{d_1}^{40} & z_{w_1}^{40} & \cdots & z_{w_1}^{40} \\ z_{d_1}^{42} & z_{d_2}^{42} & \cdots & z_{d_1}^{42} & z_{w_1}^{42} & \cdots & z_{w_1}^{42} \\ \vdots & \vdots & & \vdots & \vdots & & \vdots \\ \vdots & \vdots & & \vdots & \vdots & & \vdots \\ z_{d_1}^{80} & z_{d_2}^{80} & \cdots & z_{d_1}^{42} & z_{w_1}^{80} & \cdots & z_{w_1}^{80} \end{bmatrix} \begin{bmatrix} R_1 \\ R_2 \\ \vdots \\ R_{20} \\ R_{21} \\ \vdots \\ R_{40} \end{bmatrix} \quad (5.3)$$

According to the experience in the previous section, growing exponentials are eliminated before the least-squares solution. Therefore $[z_d, z_w]$ pole set is totally filtered from the growing terms. Instead of solving Eqs. (5.1) and (5.2), a synthesized matrix consisting of filtered $[z_d, z_w]$ poles is created to solve for residues (R_i) in Eq. (5.3).

After the calculation of the residues, the simulation of monostatic RCS values is illustrated in Fig. 5.3. Both interpolation and extrapolation are done. One can see the success of the multi-scale method comparing Fig. 5.3 with Fig. 4.12. Notice that both the error values and the number of sampled data are decreased.

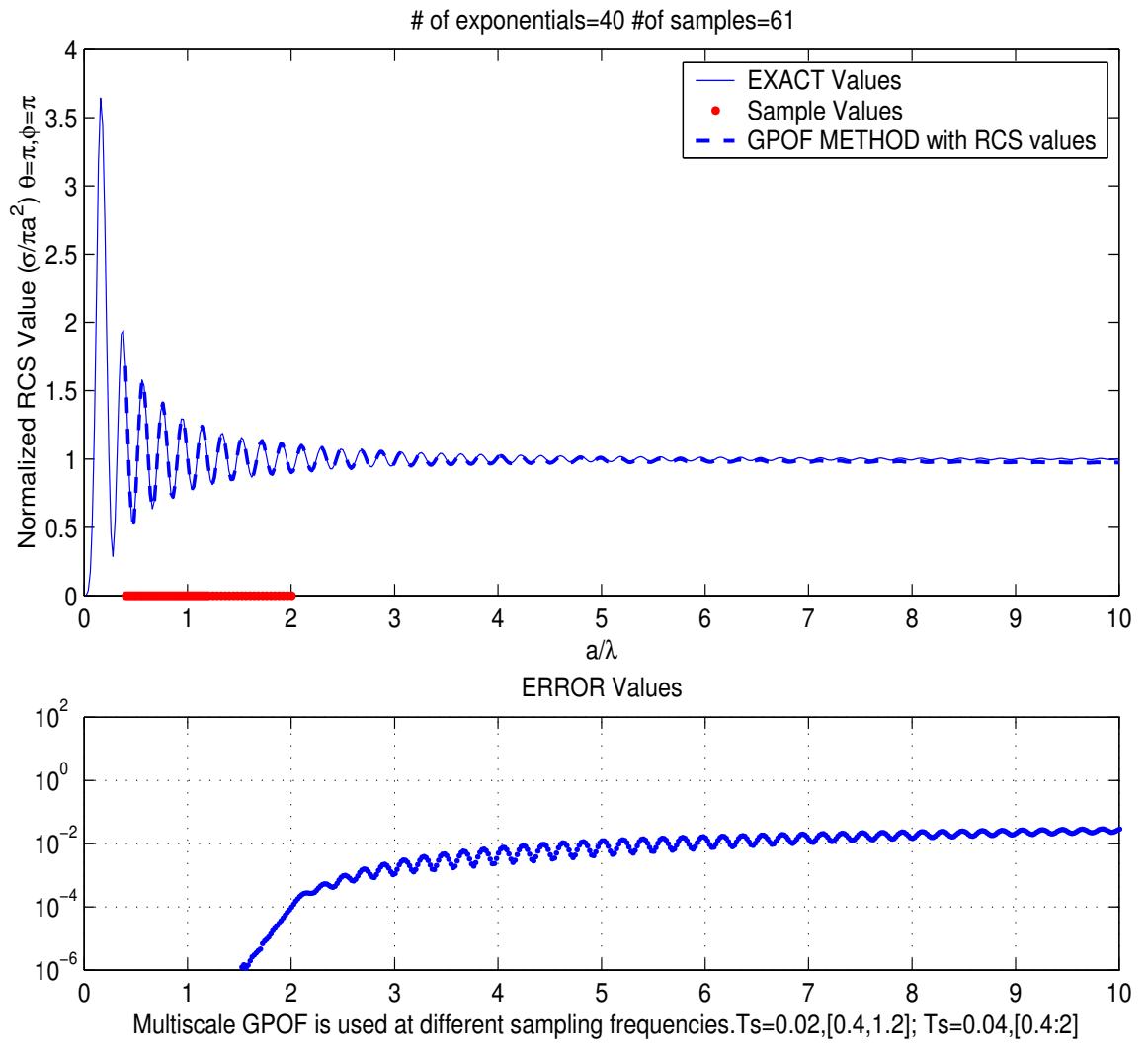


Figure 5.3: Multi-scale Matrix-Pencil Method with RCS values $M = 40$, $N = 61$, $T_s = 0.02$, Sampling interval=[0.4, 2]

5.1 Employing E_θ^s , E_ϕ^s Components in the RCS Estimation

In this section, we will see the application of the Matrix-Pencil method to the individual electric field components to estimate the RCS values. Below equation shows the components of the scattered electric field in the normalized RCS calculation,

$$\frac{\sigma(bistatic)}{\pi a^2} = \lim_{r \rightarrow \infty} \left[\frac{4\pi r^2 |\mathbf{E}^s|^2}{\pi a^2 |\mathbf{E}^i|^2} \right] = \lim_{r \rightarrow \infty} \left[\frac{4\pi r^2 (|\mathbf{E}_\theta^s|^2 + |\mathbf{E}_\phi^s|^2)}{\pi a^2 |\mathbf{E}^i|^2} \right] \quad (5.4)$$

The Matrix-Pencil method is also capable of representing complex variables, such as E_θ^s , E_ϕ^s . By using the Matrix-Pencil with full capacity yields better results in the estimation of the RCS values. Due to the complex nature of E_θ^s , E_ϕ^s components, they are also more suitable variables to represent with a complex exponents and residues. In Fig. 5.4, the monostatic ($\theta = \pi$, $\phi = \pi$) case values of E_θ^s , E_ϕ^s components are modelled with $M = 15$ exponentials. After that, high-frequency values of E_θ^s , E_ϕ^s components are predicted separately by using the exponential model. After the estimation of electric field component values, normalized RCS values are calculated by using Eq. (5.4). The success of estimation can be concluded by looking at Fig. 5.4 and Fig. 4.8. Notice that both interpolation and extrapolation errors are decreased, shown in the bottom plot of Fig. 5.4. Furthermore, we have modelled with the maximum number of exponentials (40) to estimate the electric field components in Fig. 5.5.

The extrapolation results can be acceptable until $a/\lambda = 3.5$ according to the percentage error criteria of %1. If we compare Fig. 4.8 and Fig. 5.5, we can see the increase of the acceptable extrapolation range from $[2, 2.5]$ to $[2, 3.5]$. Actually, this increase is important due to the difficulty of the RCS calculation at high frequencies. In the vicinity of $a/\lambda = 4$, the estimated RCS values become unmanageable. According to the experience about growing exponentials in section (4.2.3) and (4.2.4), the growing exponentials are eliminated.

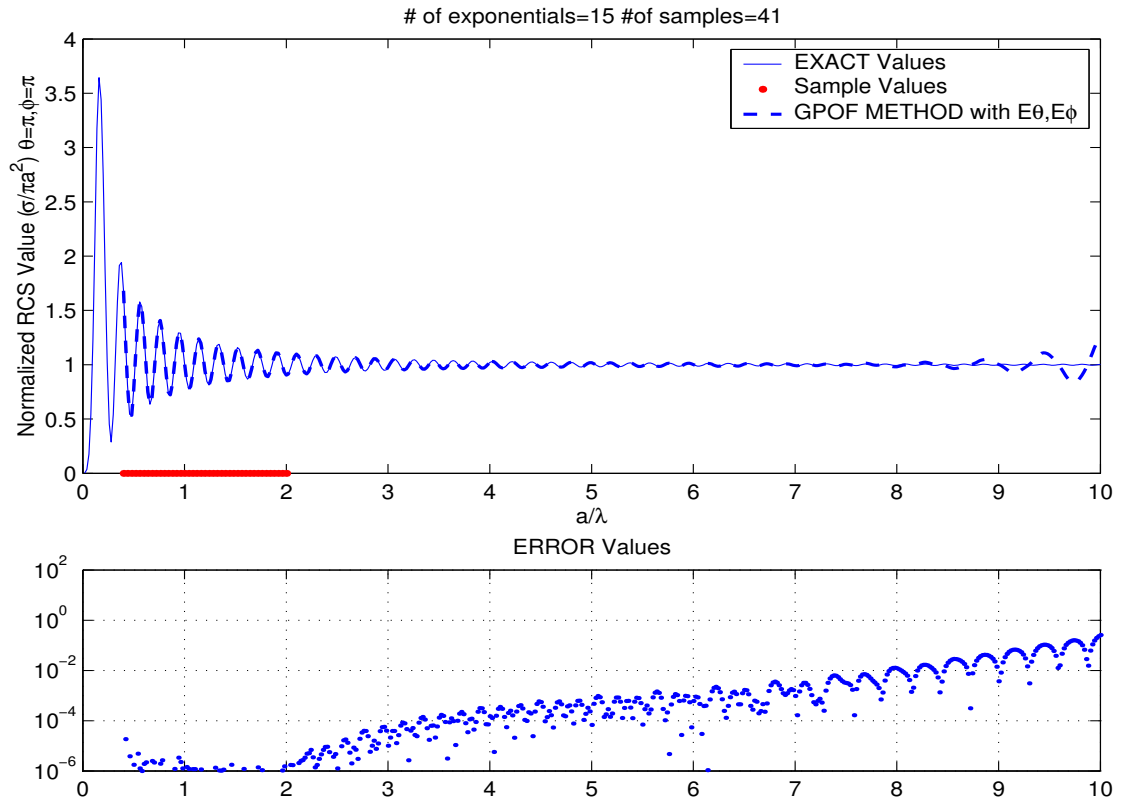


Figure 5.4: Employing E_θ^s, E_ϕ^s Components in the RCS Estimation $M = 15$, $N = 41$, $T_s = 0.04$, Sampling interval=[0.4, 2]

In Fig. 5.6, the negative damping factors (α_i) are all replaced with zero and residues are generated with the new set of exponentials. Despite the distortion in the interpolation region, the improvement can be observed in the extrapolation region by comparing Fig. 5.5 and Fig. 5.6.

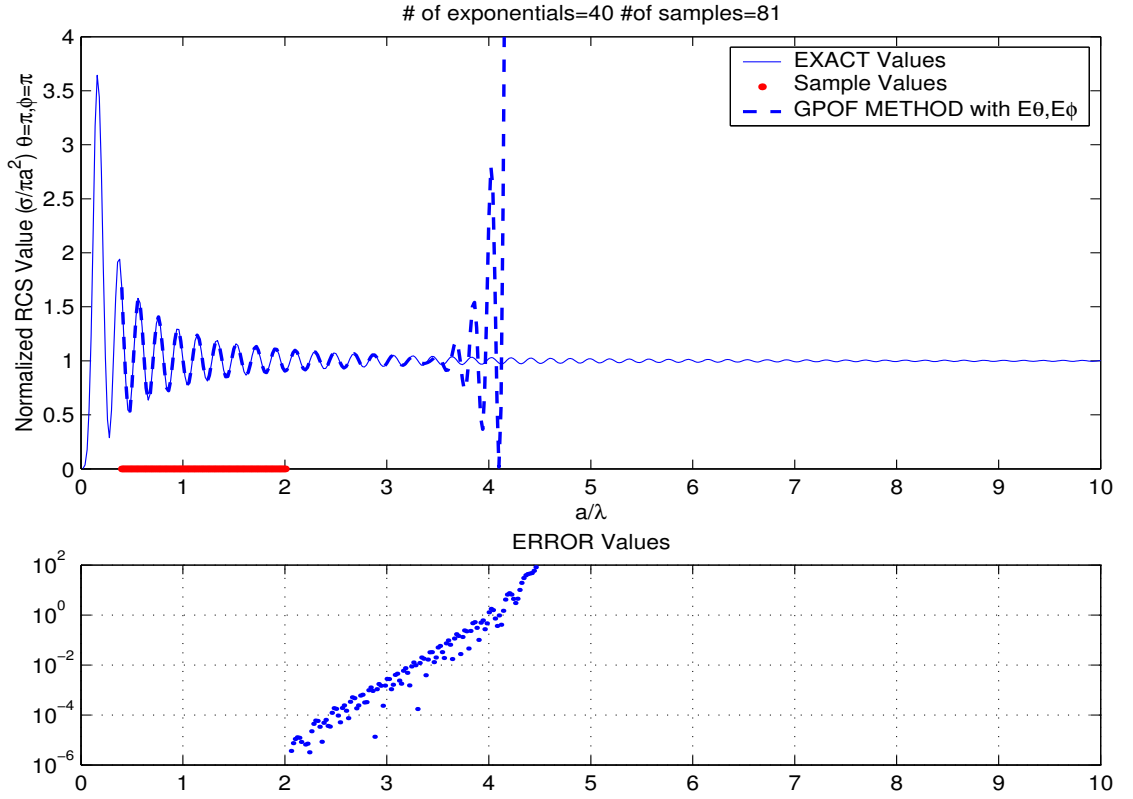


Figure 5.5: Employing E_θ^s, E_ϕ^s Components in the RCS Estimation $M = 40$, $N = 81$, $T_s = 0.02$, Sampling interval= $[0.4, 2]$

5.2 Application of Multi-Scale Matrix-Pencil Method to E_θ^s, E_ϕ^s Components

In this section, the synthesis of three main algorithms used in the previous sections for the estimation of the RCS values are presented. Up to now, we have demonstrated the elimination of growing exponentials together with updated residues (R'_i), according to the new set of exponents in Section 4.2.4. After that, multi-scale matrix pencil method is demonstrated. At last, we have used E_θ^s, E_ϕ^s components in the estimation of the RCS values. Individually, all three modifications make an improvement in the implementation of interpolation and extrapolation. Furthermore, we have synthesized three useful modifications in this section. The flowchart of synthesized algorithm is shown in Fig. 5.7. The “ Δ ” operation is simply the process of Eq. (5.4).

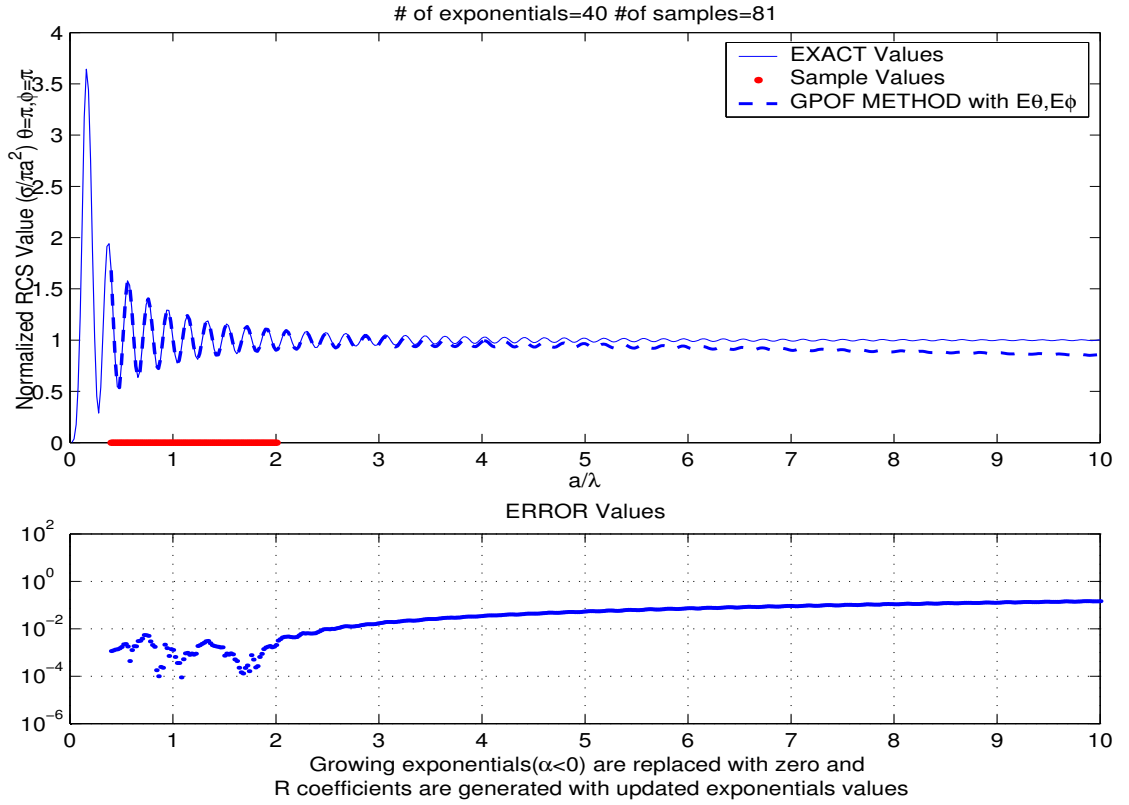


Figure 5.6: Employing E_{θ}^s, E_{ϕ}^s Components in the RCS Estimation also the Growing exponentials are eliminated $M = 40, N = 81, T_s = 0.02$, Sampling interval=[0.4, 2]

In Fig. 5.8, the application of the flowchart 5.7 is shown. Notice that the superiority of extrapolation and interpolation results can be easily observed in the bottom plot in Fig. 5.8. The estimation in the whole extrapolation interval [2, 10] can be achieved below the desired percentage error criteria 1%. In addition to that, interpolation results are already derived in the vicinity of 10^{-6} . This algorithm is a complete method that estimates the RCS values with an acceptable range.

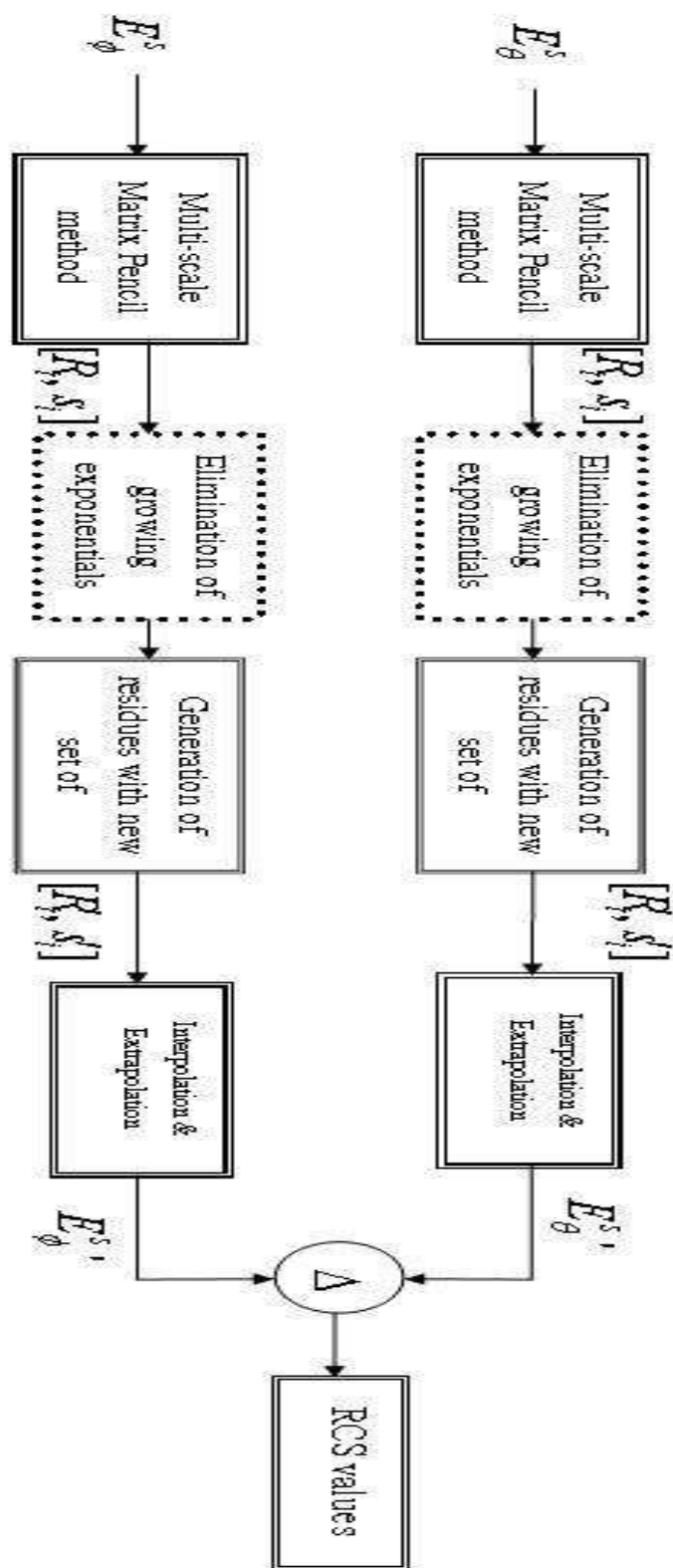


Figure 5.7: Synthesized Flowchart of the Multi-scale Matrix-Pencil method

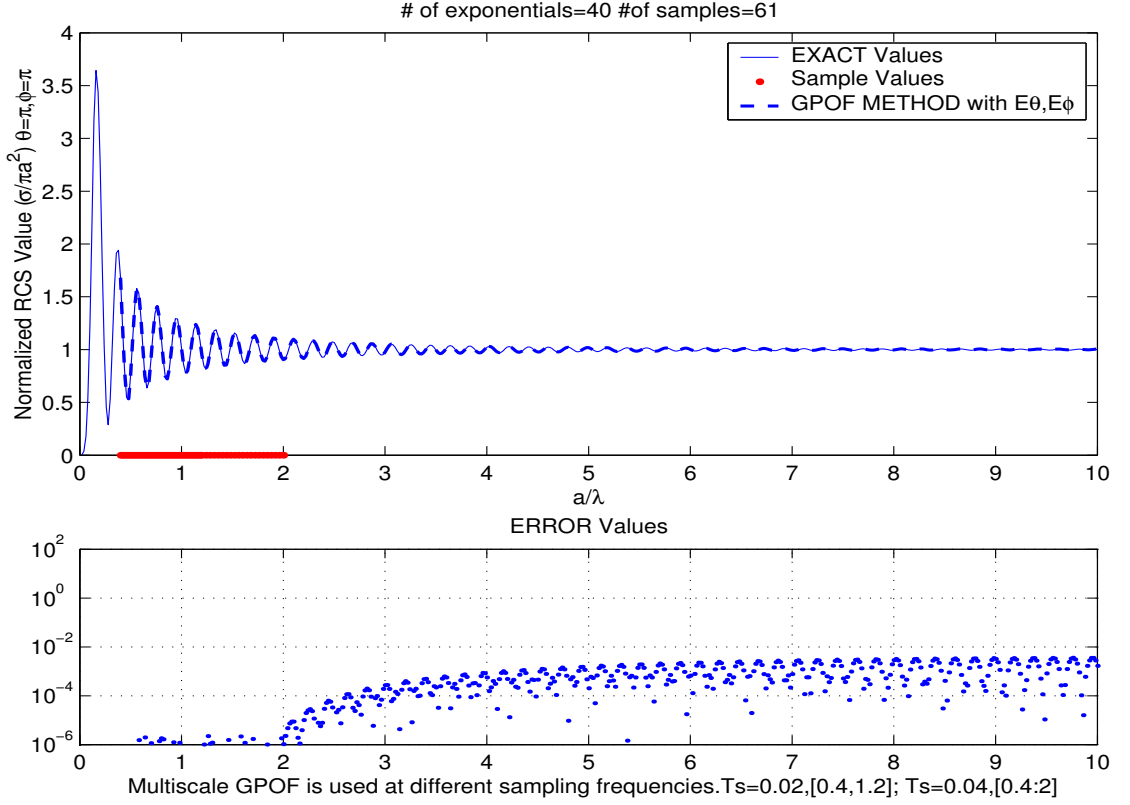


Figure 5.8: Employing E_{θ}^s, E_{ϕ}^s Components in the RCS Estimation also the Multi-Scale Matrix-Pencil Algorithm is used $M = 40, N = 61, T_s = 0.02$, Sampling interval= $[0.4, 1.2]$, $T_s = 0.04$, Sampling interval= $[0.4, 2]$

5.3 Matrix-Pencil Method with Asymptotic RCS Values

We already know that at high frequencies, exact RCS value converges to unity due to the surface area normalization of results. In the estimations of the natural Matrix-Pencil method generates negative damping factors (α_i) in the solution of exponential model. These negative damping factors grow inconsistently at the high frequency estimations. If the high frequency information is integrated to Matrix-Pencil method, these negative damping factors will be diminish. Before this, we already know that calculation of high frequency RCS values consumes too much time. First of all, we have decided to use asymptotic expressions in the calculation of high frequency RCS values. The asymptotic expression are given

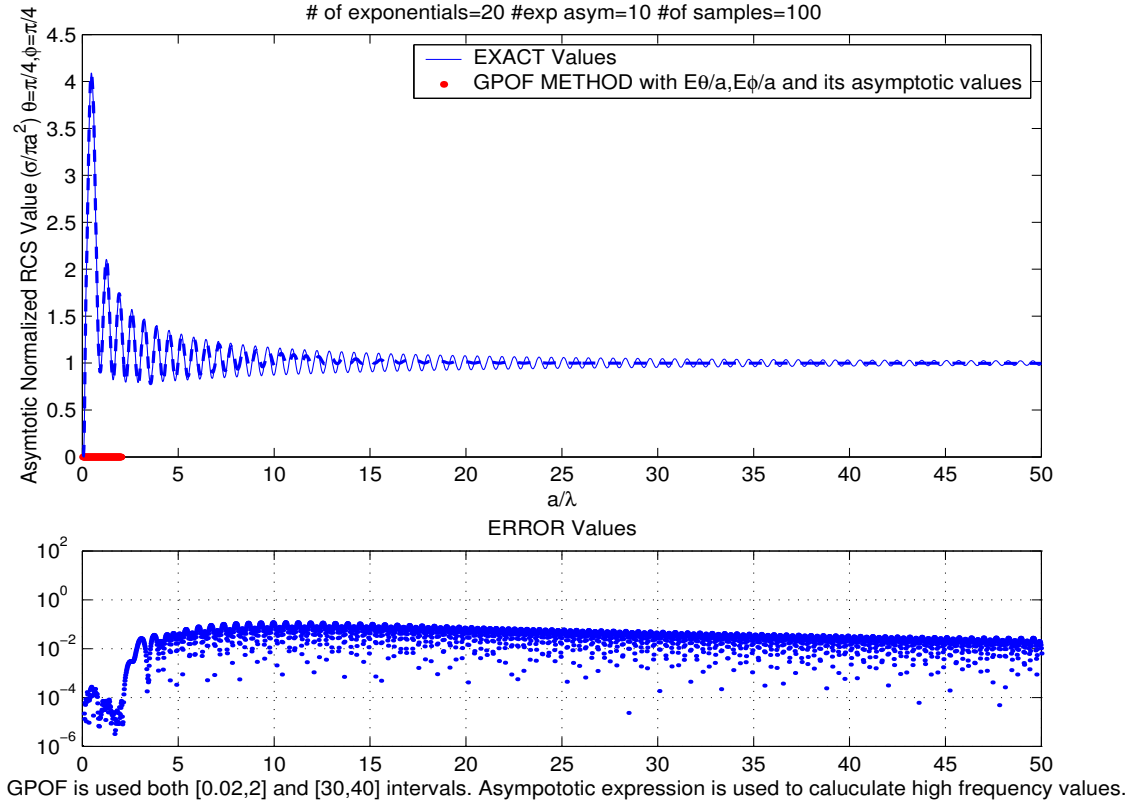


Figure 5.9: The integration of Asymptotic values with the Matrix-Pencil Method in equations (5.5a) and (5.5b) [11].

$$E_{\theta}^s = \frac{1}{2} \frac{\cos \phi a}{r} e^{-j\beta(r-2 \cos \theta/2)} \quad (5.5a)$$

$$E_{\phi}^s = \frac{1}{2} \frac{\sin \phi a}{r} e^{-j\beta(r-2 \cos \theta/2)} \quad (5.5b)$$

In this section, a method is investigated to integrate the knowledge of asymptotic RCS values to the Matrix-Pencil algorithm. Notice that these two asymptotic equations are so elementary with respect to the analytical expressions (2.23b), (2.23c). Due to simplicity, we can easily compute high frequency values in extensive intervals in the vicinity of 10^{-2} . Based on this information, a Matrix-Pencil algorithm is modified to include the asymptotic data. In Fig. 5.9, Matrix-Pencil estimations demonstrated in conjunction with the asymptotic values. The integration of asymptotic data, prevents to yield Matrix-Pencil algorithm unwanted negative damping factors (α_i). To investigate the limits of algorithm, we have used exact data (ideal conditions) instead of asymptotic values in Fig. 5.10. Notice that the error values are decreased between $a/\lambda = 5$ and $a/\lambda = 10$.

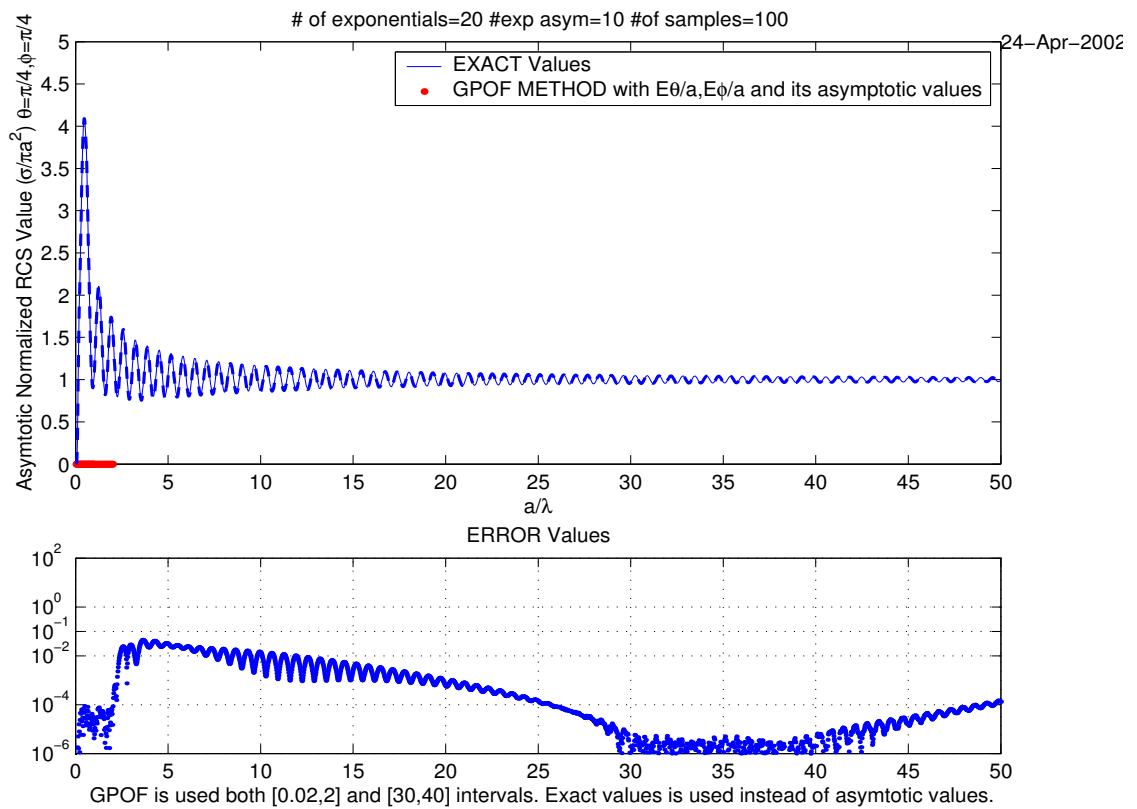


Figure 5.10: The integration of imaginary Asymptotic values with the Matrix-Pencil Method

5.4 Applications of the Matrix-Pencil Method to Surface Currents

In this section, the estimation of induced currents on the PEC sphere is demonstrated. Exact current values can be calculated on the surface of the PEC sphere

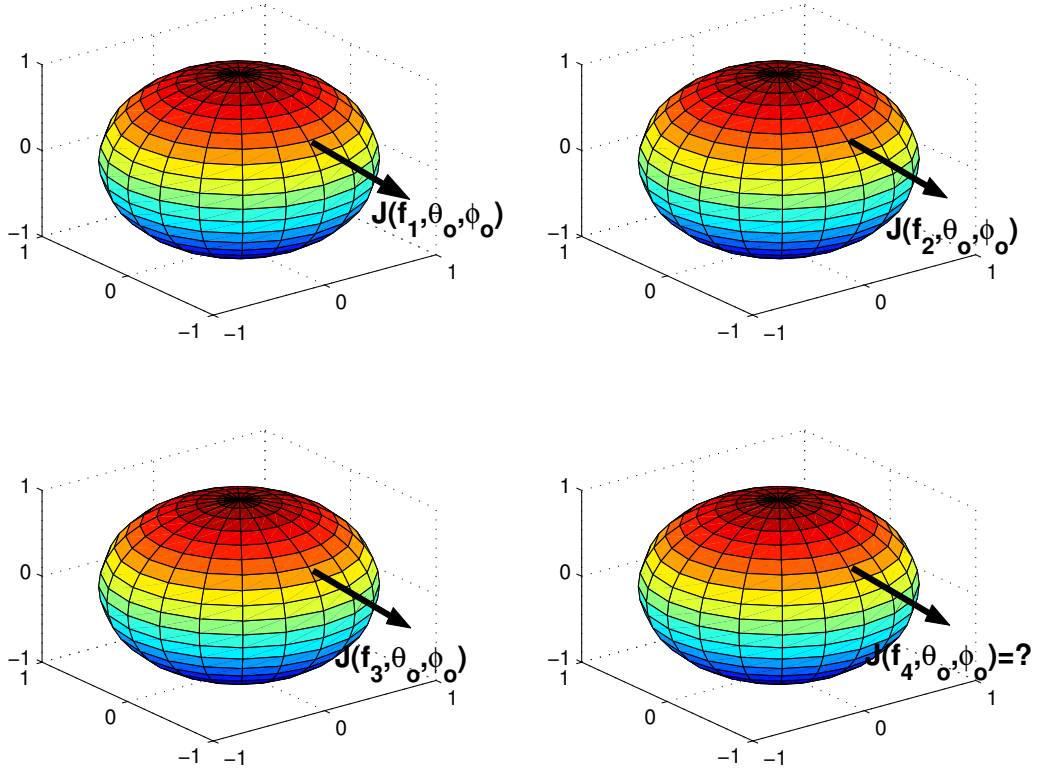


Figure 5.11: Prediction of current value $\mathbf{J}(\theta_0, \phi_0)$ at frequency f_4 by using the lower frequency values $[\mathbf{J}(f_1, \theta_0, \phi_0), \mathbf{J}(f_2, \theta_0, \phi_0), \mathbf{J}(f_3, \theta_0, \phi_0)]$

by using analytical expressions (2.36a) and (2.36b). The problem is to estimate high-frequency current values from its sampled data. It is illustrated in Fig. 5.11.

In Fig. 5.12, the modified Matrix-Pencil algorithm is used to predict the high-frequency values of the J_θ . The exponents and residues are generated according to the samples taken from $[0, 2]$ interval. The location of concerned J_θ is chosen as $(\theta = 45^\circ, \phi = 0^\circ)$. The modified algorithm available in Section 4.2.4 is used in the estimation of induced current values. Briefly this algorithm eliminates

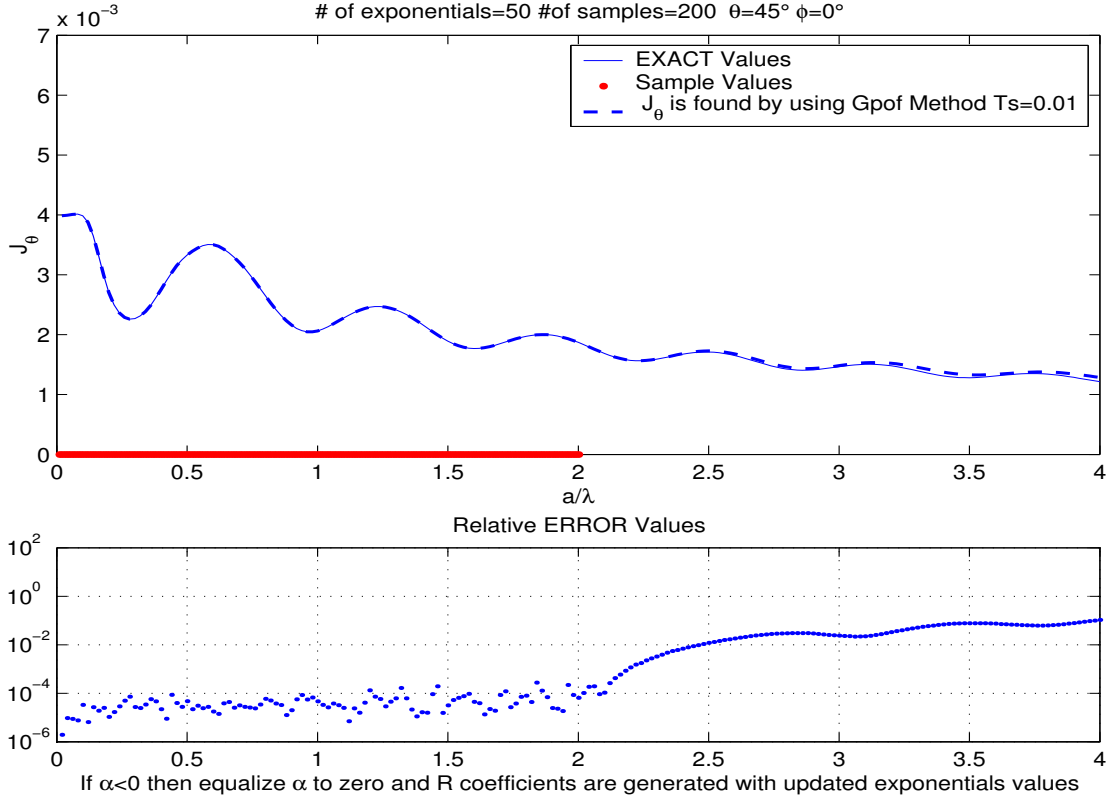


Figure 5.12: Applications of the Matrix-Pencil Method to Surface Current, the residues are generated with the eliminated set of exponentials ($\theta = 45^\circ$, $\phi = 0^\circ$) J_θ is sampled from $[0, 2]$, $M = 50$.

the growing exponentials. According to the new set of exponentials residues are generated with least squares problem. In Fig. 5.12, the bottom plot shows us the relative error instead of absolute error results. Relative error is defined as

$$\left| \frac{exact - approx}{exact} \right|$$

The high-frequency values can be predicted in the vicinity of 10^{-2} (relative error values) until $a/\lambda = 2.5$. We move around on the ϕ cut by increasing θ angle. Actually, the surface current components J_θ and J_ϕ have a small variety according to the ϕ direction. The value of the surface current depends on the ϕ angle sinusoidally. The main complexity of the surface currents concentrates in the θ angle direction. Due to this fact, only θ angle parameter is changed from $\theta = 45^\circ$ to $\theta = 90^\circ$ in the next Figure 5.13. When $\theta = 90^\circ$ exactly corresponds to the equator of the of the sphere. The estimated induced current values are better than the previous simulation of $J_\theta(45^\circ, 0^\circ)$ in Fig. 5.12. The difference between exact values and predicted results are obtained less than 10^{-2} boundary. From the bottom plot, relative error values can be seen in the Fig. 5.13.

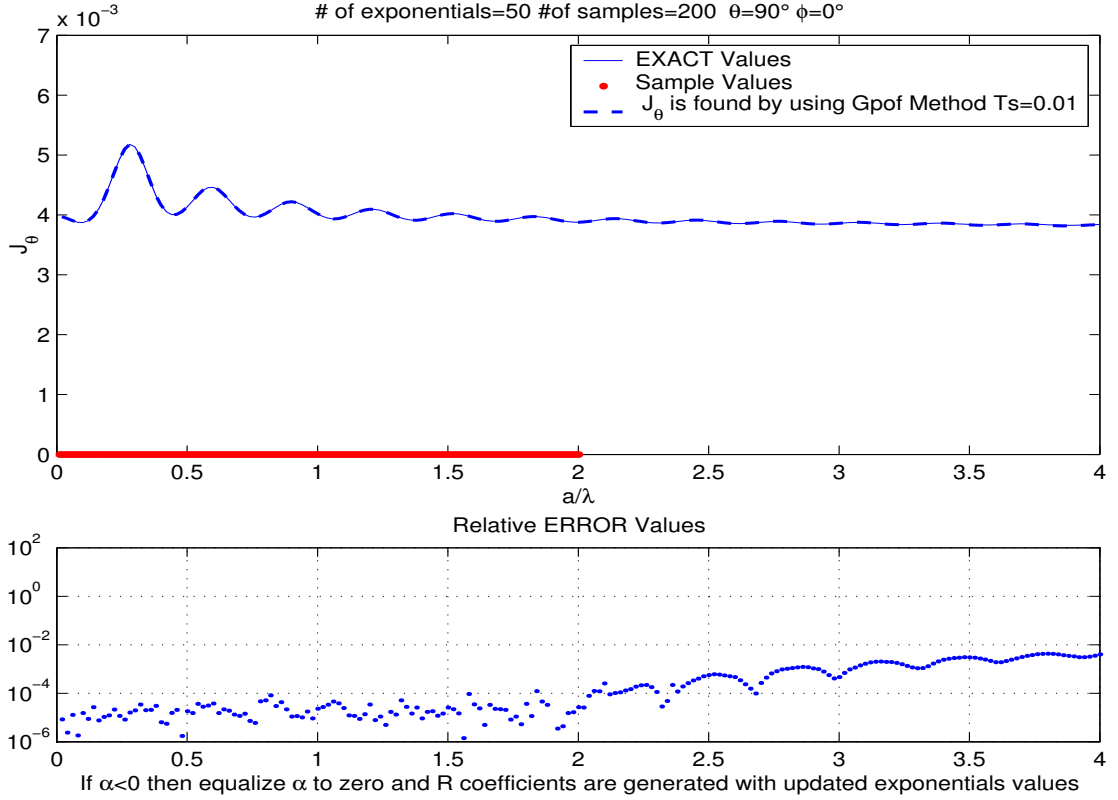


Figure 5.13: Applications of the Matrix-Pencil Method to Surface Current, the residues are generated with the eliminated set of exponentials ($\theta = 90^\circ$, $\phi = 0^\circ$) J_θ is sampled from $[0, 2]$, $M = 50$.

Finally, if we come near to the bottom of the sphere, extrapolation results become more accurate. When ($\theta = 180^\circ$, $\phi = 0^\circ$), the relative error results are obtained below the 10^{-2} boundary too. They can be seen at bottom plot in Figure 5.14.

After application of the modified Matrix-Pencil to J_θ component, we have tested this algorithm with J_ϕ component of surface current. The longitude of the J_ϕ of surface current is chosen as $\phi = 90^\circ$ cut where the J_ϕ takes its maximum values ($\sin 90^\circ$ takes its maximum value in the analytical expressions (2.36b)).

The latitude of the J_ϕ in Fig. 5.15 is set to $\theta = 45^\circ$. When we look at the bottom plot in Fig. 5.15, the relative error results is high with respect to the previous results. If we concentrate at the at the upper plot in Fig. 5.15, the predicted results follow the exact current values. Due to exact high frequency values small in magnitude, the calculation of relative error magnifies the deviation of the predicted values.

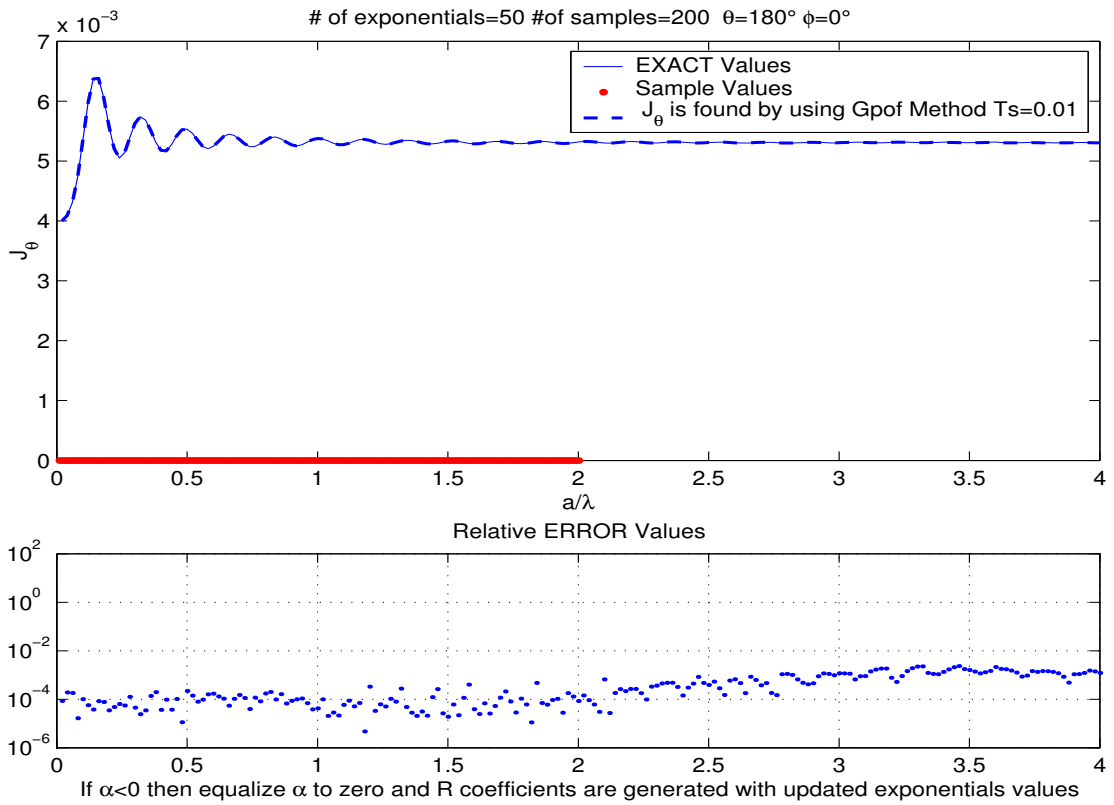


Figure 5.14: Applications of the Matrix-Pencil Method to Surface Current, the residues are generated with the eliminated set of exponentials ($\theta = 180^\circ$, $\phi = 0^\circ$)

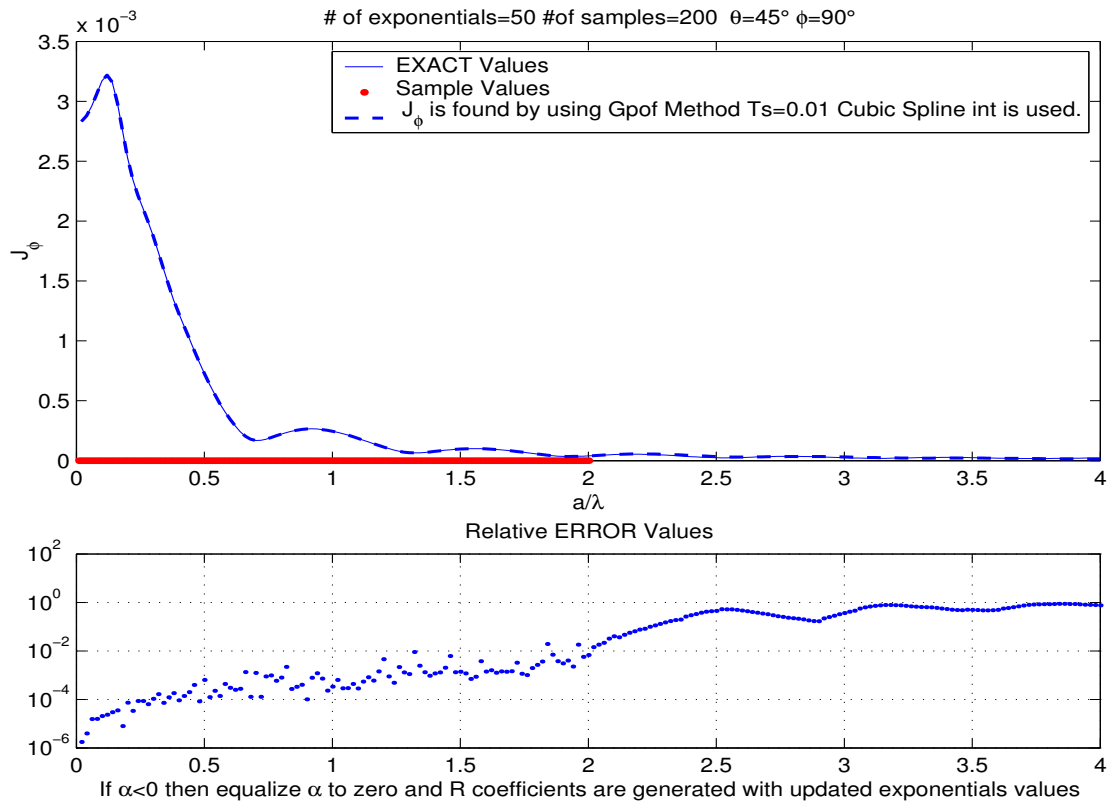


Figure 5.15: Applications of the Matrix-Pencil Method to Surface Current, the residues are generated with the eliminated set of exponentials ($\theta = 45^\circ$, $\phi = 90^\circ$) J_ϕ is sampled from $[0, 2]$, $M = 50$.

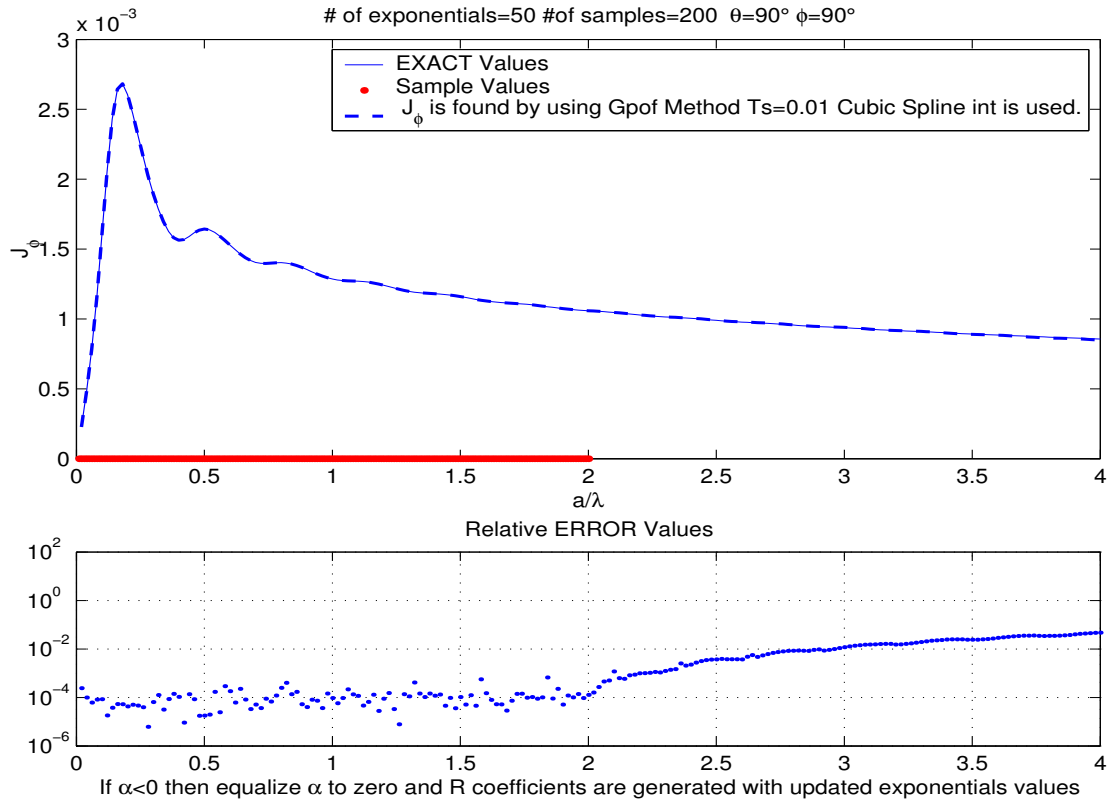


Figure 5.16: Applications of the Matrix-Pencil Method to Surface Current, the residues are generated with the eliminated set of exponentials ($\theta = 90^\circ$, $\phi = 90^\circ$) J_ϕ is sampled from $[0, 2]$, $M = 50$.

After that, we have tested the modified Matrix-Pencil algorithm, at the location ($\theta = 90^\circ, \phi = 90^\circ$). The results are shown in Fig. 5.16. The extrapolation values can be accepted until frequency $a/\lambda = 3$. When $\theta = 180^\circ$ at the bottom of the sphere, the magnitude of J_ϕ surface current is the same as J_θ component in Fig. 5.12. These two coordinates ($\theta = 90^\circ, \phi = 0^\circ$) and ($\theta = 90^\circ, \phi = 90^\circ$) denote the bottom of the sphere. Magnitude of the J_ϕ and J_θ must be the same to satisfy the uniqueness of the resultant \mathbf{J} surface current. The Fig. 5.12 can be considered also as the estimation of J_ϕ component.

5.5 Comparisons with Other Extrapolation Techniques

In this section, other extrapolation algorithms currently available in the literature are compared with results of the Matrix-Pencil method. One of them is an extrapolation technique [7] based on the ESPRIT superresolution algorithm. One of the terms defined in [7] to measure the performance of the extrapolation is the relative extrapolation bandwidth (REB). It is defined as the ratio between the number of points extrapolated and the number of points computed. The REB of the best results in [7] is equal to $\text{REB} = (53/8) = 6.3$. If we calculate the REB of the Figure 5.8, it is equal to $(500/61) = 8.2$. We see that in the Multi-Scale Matrix-Pencil method the relative extrapolation bandwidth is greater than the ESPRIT superresolution algorithm. Also, in [7] the average deviation of the extrapolated frequency response from the calculated response is 2.06 dBm (~ 0.04). In our estimations, the error results never exceeds the 10^{-2} boundary. This is also a success in the accuracy of the Multi-Scale Matrix-Pencil method.

The second comparison is done with [8], which uses the GPOF method in the extrapolation of the surface current. The relative error values in the extrapolation of the surface current components is equal to the 0.5. If we observe results of the estimations in the Figures 5.14 , the relative error values are less than 10^{-2} .

We have also used rational function model instead of exponential model for representation of the RCS values. To solve for the coefficients of the denominator and numerator, we have applied some appropriate algorithms from the signal processing area. These are the covariance and the autocorrelation methods [12]. Both of them are designed for the solution of the all-pole models and they generate stable model coefficients as a result. The estimation results of the autocorrelation and the covariance methods are similar to the desired RCS values, but we observe a subinterval shifting in the estimated results. Subinterval

shifting actually comes from the incompetence of the used zero-order numerator models.

The third algorithm applied to RCS values is the iterative pre-filtering (Steiglitz-McBride) method, which is an iterative technique to implement the direct method of signal modelling. If we set the suitable number of poles and zeros in the rational function, iterative algorithm yields good results in the estimations. However, it is hard to know the appropriate number of poles and zeros.

Chapter 6

Angular Extrapolation of the Induced Currents

In the previous chapter, the estimation of current values in the frequency dimension (a/λ) is demonstrated. In this chapter, we have modelled the same surface current values in the angular dimension.

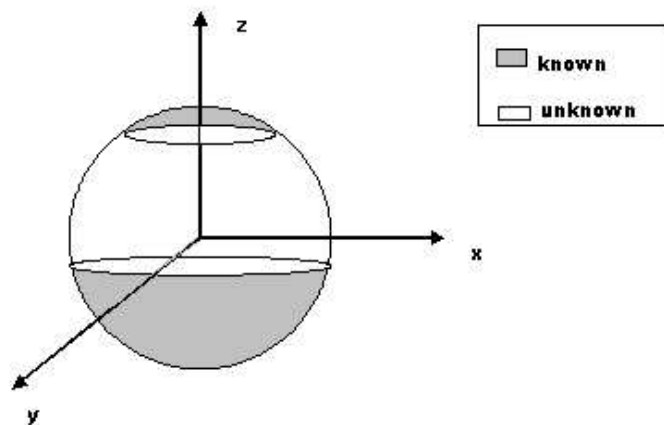


Figure 6.1: The location of the unknown current values on the surface of the sphere

Imagine that the current values are known on the black shaded parts of the

sphere in Fig. 6.1. We have investigated a method to estimate current values remaining part of the sphere. To predict J_θ , J_ϕ current values at the unknown part of the sphere, we set up a model with ‘‘Legendre polynomials’’. The Legendre polynomials $\left(\frac{P_i^1(\cos \theta)}{\sin \theta}\right)$ are used as basis functions of the constructed model;

$$J_\theta(\theta, \phi) = \sum_{i=1}^M K_i \cos \phi \left(\frac{P_i^1(\cos \theta)}{\sin \theta} \right) \quad (6.1a)$$

In the summation $\cos \phi$ term is independent of index i , so $\cos \phi$ may be written out of the summation operator. By the same manner, for J_ϕ a suitable model can be written similar to J_θ ;

$$J_\theta(\theta, \phi) = \cos \phi \sum_{i=1}^M K_i \frac{P_i^1(\cos \theta)}{\sin \theta} \quad (6.2a)$$

$$J_\phi(\theta, \phi) = \sin \phi \sum_{i=1}^M K_i \frac{P_i^1(\cos \theta)}{\sin \theta} \quad (6.2b)$$

The coefficients, K_i 's are solved from least-squares problem at appendix A.4. The least-squares solution of Eq. (6.3) gives us the K_i coefficients;

$$\begin{bmatrix} J_\theta(\theta_1) \\ J_\theta(\theta_2) \\ \vdots \\ J_\theta(\theta_N) \end{bmatrix} = \begin{bmatrix} \frac{P_1^1(\cos \theta_1)}{\sin \theta_1} & \frac{P_2^1(\cos \theta_1)}{\sin \theta_1} & \dots & \frac{P_M^1(\cos \theta_1)}{\sin \theta_1} \\ \frac{P_1^1(\cos \theta_2)}{\sin \theta_2} & \frac{P_2^1(\cos \theta_2)}{\sin \theta_2} & \dots & \frac{P_M^1(\cos \theta_2)}{\sin \theta_2} \\ \vdots & \vdots & \vdots & \vdots \\ \frac{P_1^1(\cos \theta_N)}{\sin \theta_N} & \frac{P_2^1(\cos \theta_N)}{\sin \theta_N} & \dots & \frac{P_M^1(\cos \theta_N)}{\sin \theta_N} \end{bmatrix} \begin{bmatrix} K_1 \\ K_2 \\ \vdots \\ K_M \end{bmatrix} \quad (6.3)$$

where N data samples are taken when $\phi = 0^\circ$, $\cos \phi = 1$.

The induced current values are sampled in the θ direction. The location of the sampled data points are shown in Fig. 6.2 with thick black dots. Only using the data samples at $\phi = 0^\circ$ cut, we can estimate J_θ component whole surface of the sphere.

Employing data samples which are taken from the thick line shown in Fig. 6.2, we can produce J_θ component at every point in the boundary of the rectangular area or all over the surface of the sphere shown in Fig. 6.1.

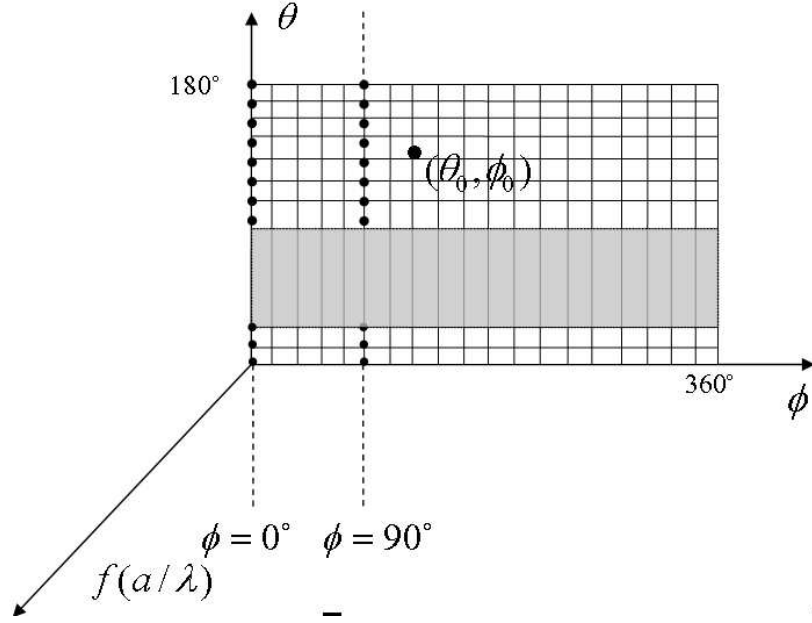


Figure 6.2: The open form of sphere surface lays along a flat plane. The variables which totally represents the sphere surface, θ, ϕ are taken as vertical and horizontal axis, respectively.

Also, we can estimate J_ϕ component of the surface current with slight differences in the application of the same algorithm. In this case, the induced current values are sampled from the cut which maximizes the $J_\phi(\phi = 90^\circ)$ component on the surface of the sphere.

J_θ component of induced current is estimated with using data samples which are taken from the region ($0^\circ \leq \theta \leq 6^\circ, 69^\circ \leq \theta \leq 180^\circ$). Fig. 6.3 shows us the application of this algorithm. The predicted results are below the 10^{-6} boundary which are shown at the bottom plot of the Fig. 6.3. Moreover, the interpolated result are better than the predicted results which are less than 10^{-12} .

In the solution of the K_i coefficients, to construct the least-squares problem in Eq. (6.3), the parameters M (the number of K_i coefficients) is chosen as 23 at $a/\lambda = 2$. The results are plotted in Fig. 6.3 with its relative error values. Also, we have applied the same algorithm at $a/\lambda = 4$, with the number of K_i coefficients $M = 36$. The results of algorithm is shown in Fig. 6.4 with its relative error plot. The efficiency of the results can be decided by looking at the relative error values.

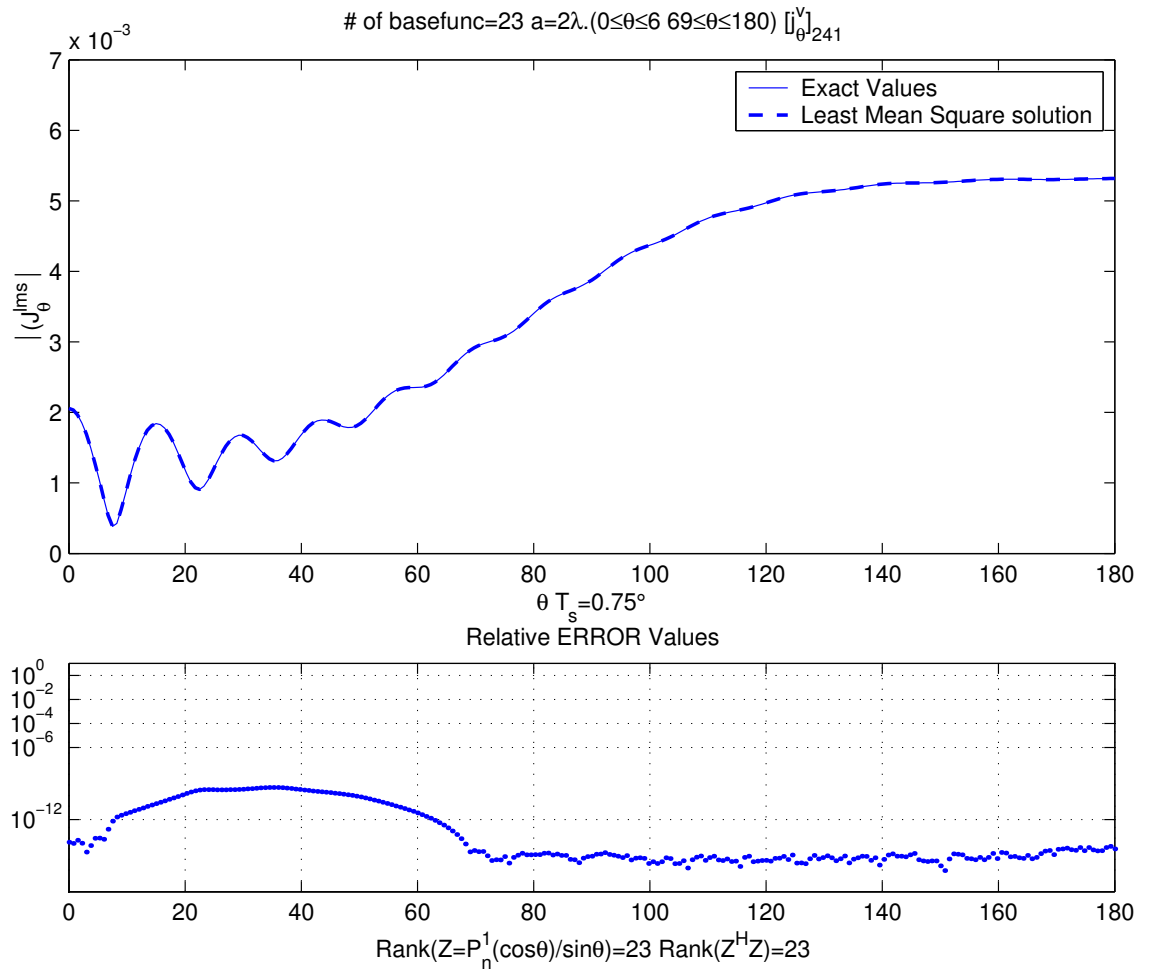


Figure 6.3: The Legendre-basis algorithm is applied to J_θ component of surface current when $a/\lambda = 2$, samples are taken from ($0^\circ \leq \theta \leq 6^\circ$, $69^\circ \leq \theta \leq 180^\circ$) number of coefficients $M = 23$

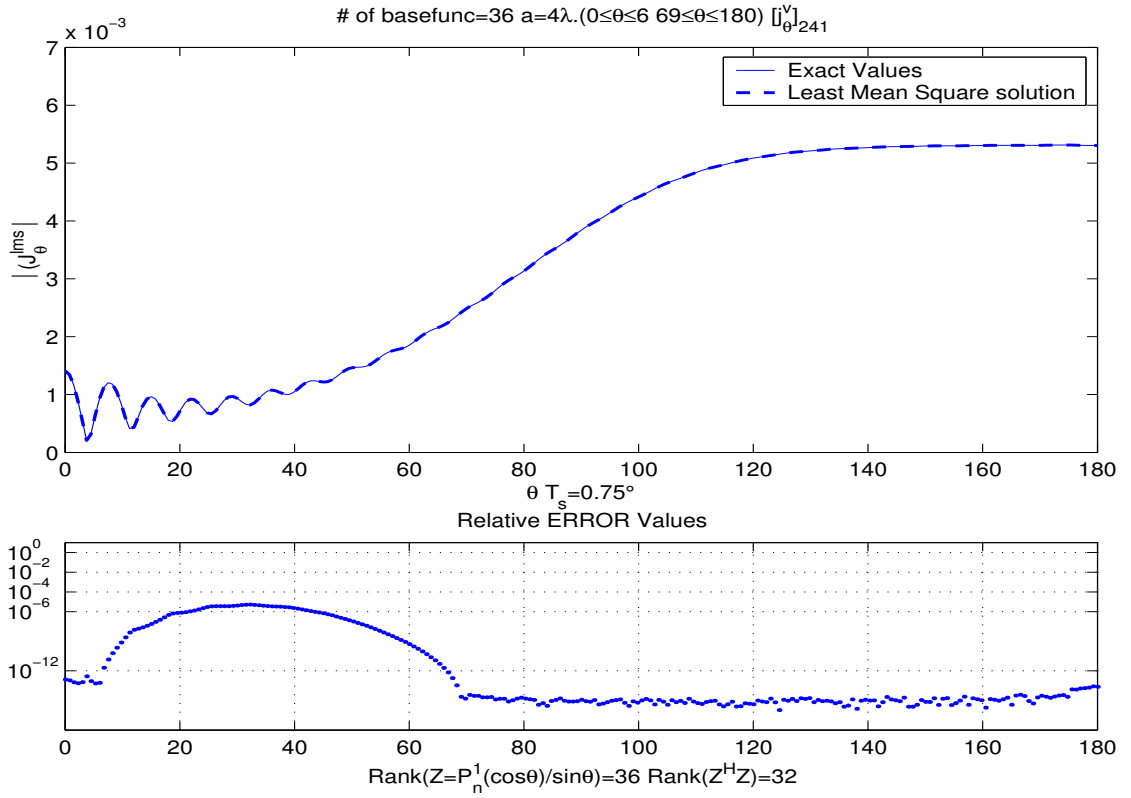


Figure 6.4: The Legendre-basis algorithm is applied to J_θ component of surface current when $a/\lambda = 4$, samples are taken from ($0^\circ \leq \theta \leq 6^\circ$, $69^\circ \leq \theta \leq 180^\circ$) number of coefficients $M = 36$

The other component (J_ϕ) of the surface current is also estimated at $a/\lambda = 2$ with $M = 23$. The samples are taken from the region ($0^\circ \leq \theta \leq 6^\circ$, $69^\circ \leq \theta \leq 180^\circ$), only the difference of the sampled ϕ cut is changed from 0° to 90° .

The results are shown in Fig. 6.5 with its relative error results. The Legendre-Base algorithm yields results below the 10^{-6} line boundary in the bottom plot in Fig. 6.5. The difference between the exact and estimated results can not be understand by the naked eye. Also, at $a/\lambda = 4$, J_ϕ values are solved from the Legendre-basis algorithm in Fig. 6.6. Also, the efficiency of the algorithm can be observed from the figure.

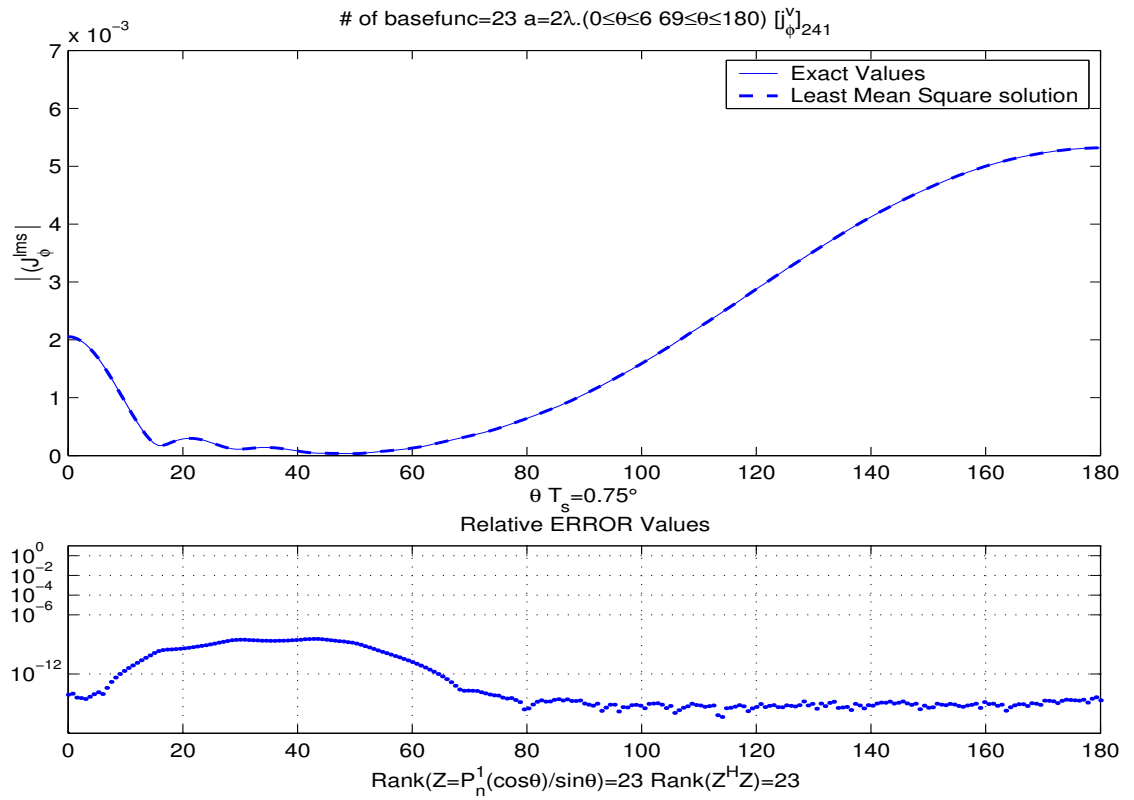


Figure 6.5: The Legendre-basis algorithm is applied to J_ϕ component of surface current when $a/\lambda = 2$, samples are taken from $(0^\circ \leq \theta \leq 6^\circ, 69^\circ \leq \theta \leq 180^\circ)$ number of coefficients $M = 23$

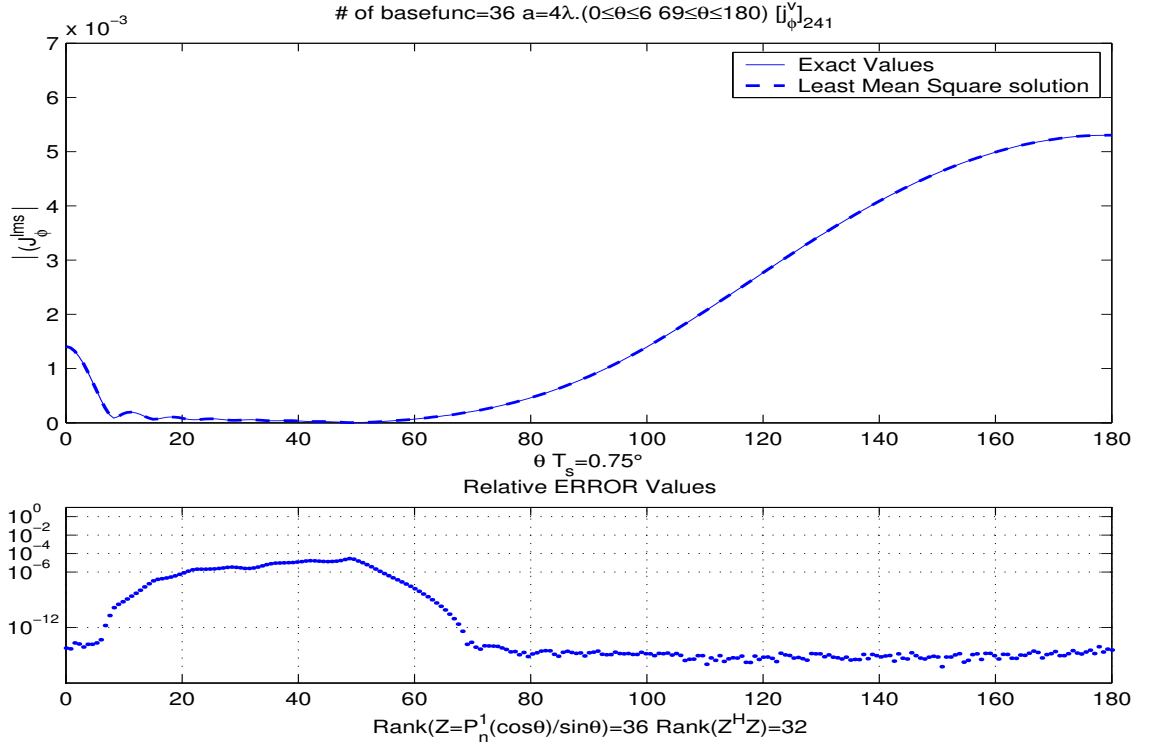


Figure 6.6: The Legendre-basis algorithm is applied to J_ϕ component of surface current when $a/\lambda = 2$, samples are taken from $(0^\circ \leq \theta \leq 6^\circ, 69^\circ \leq \theta \leq 180^\circ)$ number of coefficients $M = 36$

6.1 Calculation of RCS with the Integration of the Surface Currents

In this section, the calculation of electric field components with the integration of the surface currents on the surface of the PEC sphere is described. Before the derivation of the vector moment components of PEC sphere, calculation of the far-zone fields of arbitrary electric currents sources subject is explained as an introduction of the section.

Far-zone conditions are

i. $r \gg r'$

ii. $r \gg \lambda$

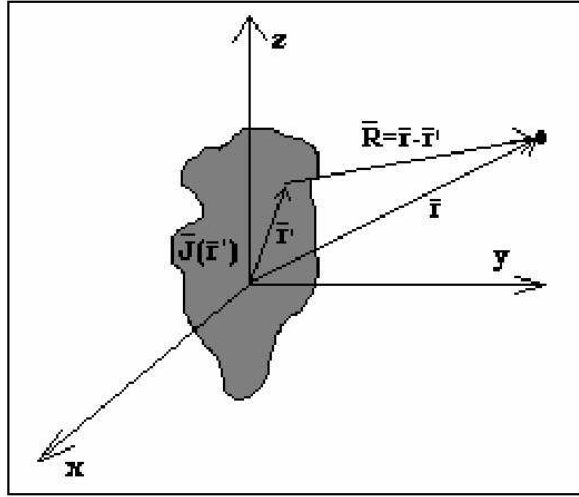


Figure 6.7: An Arbitrary Electric Current Source

$$\begin{aligned}
 R &= |\bar{\mathbf{r}} - \bar{\mathbf{r}}'| = \sqrt{(\bar{\mathbf{r}} - \bar{\mathbf{r}}') \cdot (\bar{\mathbf{r}} - \bar{\mathbf{r}}')} \\
 &= \sqrt{r^2 + (r')^2 - 2\bar{\mathbf{r}} \cdot \bar{\mathbf{r}}'} \cong r \sqrt{1 - \frac{2\hat{\mathbf{r}} \cdot \bar{\mathbf{r}}'}{r}} \\
 &\cong r - \hat{\mathbf{r}} \cdot \bar{\mathbf{r}}'
 \end{aligned}$$

Using $e^{j\omega t}$ convention Vector Magnetic Potential \mathbf{A} can be written in terms of the surface currents,

$$\begin{aligned}
 \bar{\mathbf{A}}(\bar{\mathbf{r}}) &= \int_V dv' \bar{\mathbf{J}}(\bar{\mathbf{r}}') \frac{\exp(-jk|\bar{\mathbf{r}} - \bar{\mathbf{r}}'|)}{4\pi|\bar{\mathbf{r}} - \bar{\mathbf{r}}'|} \cong \int_V dv' \bar{\mathbf{J}}(\bar{\mathbf{r}}') \frac{\exp(-jk(r - \hat{\mathbf{r}} \cdot \bar{\mathbf{r}}'))}{4\pi r} \quad (6.4) \\
 &= \underbrace{\frac{e^{-jkr}}{4\pi r}}_{g(r)} \int_V dv' \bar{\mathbf{J}}(\bar{\mathbf{r}}') \frac{\exp(-jk\hat{\mathbf{r}} \cdot \bar{\mathbf{r}}')}{4\pi r} \quad (6.5)
 \end{aligned}$$

In the approximation of $|\bar{\mathbf{r}} - \bar{\mathbf{r}}'|$, we neglect the $\hat{\mathbf{r}} \cdot \bar{\mathbf{r}}'$ component in the denominator. The term $jk\hat{\mathbf{r}} \cdot \bar{\mathbf{r}}'$ is kept in the exponent in Eq. (6.4), because its contribution to the phase variation can be significant when it is the order of, or larger than, π . We define a vector current moment,

$$\vec{f}(\theta, \phi) = \int_V dv' \bar{\mathbf{J}}(\bar{\mathbf{r}}') \exp(jk\hat{\mathbf{r}} \cdot \bar{\mathbf{r}}')$$

Magnetic Field intensity can be found by taking the curl of the Vector Magnetic Potential,

$$\bar{\mathbf{H}}(\bar{r}) = \nabla \times \bar{\mathbf{A}}(\bar{r}) = \nabla \times (g(r)\bar{f}(\theta, \phi)) = \nabla g(r) \times \bar{f}(\theta, \phi) + g(r)(\nabla \times \bar{f}(\theta, \phi))$$

The terms in the magnetic field intensity $\bar{\mathbf{H}}$;

$$\nabla g(r) = \hat{a}_r \frac{\partial}{\partial r} \left(\frac{\exp(-jkr)}{4\pi r} \right) = -\hat{a}_r \frac{k^2}{4\pi} \left[\frac{j}{kr} + \frac{1}{(kr)^2} \right] \exp(-jkr)$$

Note that $kr = 2\pi r/\lambda \gg 1$ then,

$$\nabla g(r) \cong -\hat{r} \frac{k^2}{4\pi} \left[\frac{j}{kr} \right] \exp(-jkr) = -jk\hat{r}g(r) \propto \frac{1}{r}$$

$$\nabla \times \bar{f}(\theta, \phi) = \frac{1}{r^2 \sin \theta} \begin{vmatrix} \hat{r} & r\hat{\theta} & r \sin \theta \hat{\phi} \\ \frac{\partial}{\partial r} & \frac{\partial}{\partial \theta} & \frac{\partial}{\partial \phi} \\ f_r & r f_\theta & r \sin \theta f_\phi \end{vmatrix} \propto \frac{1}{r}$$

$$(\nabla g(r)) \times \bar{f}(\theta, \phi) \propto \frac{1}{r}$$

and

$$g(r)(\nabla \times \bar{f}(\theta, \phi)) \propto \frac{1}{r^2}$$

since

$$\bar{\mathbf{H}}(\bar{r}) \cong \nabla g(r) \times \bar{f}(\theta, \phi) = -jk g(r) \left[\hat{\phi} f_\theta - \hat{\theta} f_\phi \right].$$

We can also find a short way of calculating far-zone electric field intensity,

$$\begin{aligned} \bar{\mathbf{E}}(\bar{r}) &= \frac{1}{j\omega\epsilon} \nabla \times \mathbf{H}(\bar{r}) = \frac{-jk}{j\omega\epsilon} \nabla \times [g(r)\hat{r} \times \bar{f}(\theta, \phi)] \\ &= \frac{-jk}{j\omega\epsilon} \left\{ \nabla g(r) \times (\hat{r} \times \bar{f}(\theta, \phi)) + g(r) [\nabla \times (\hat{r} \times \bar{f}(\theta, \phi))] \right\} \\ &= \frac{-k}{\omega\epsilon} \frac{k}{j} g(r) \left[-\hat{\theta} f_\theta - \hat{\phi} f_\phi \right] = -jk \left(\frac{k}{\omega\epsilon} \right) \left[\hat{\theta} f_\theta + \hat{\phi} f_\phi \right] g(r) \end{aligned}$$

then

$$\bar{\mathbf{E}}(\bar{r}) = -jk\eta \left[\hat{\theta} f_\theta + \hat{\phi} f_\phi \right] g(r) \quad (6.6)$$

Actually *Vector Current Moment* is a volume integral;

$$\vec{f}(\theta, \phi) = \int_V dv' \vec{\mathbf{J}}(\vec{r}') e^{jk\hat{r} \cdot \vec{r}'}$$

Note that for far-field solutions, the main problem is completed by evaluating the *Vector Current Moment* in Eq. 6.6. There are some numerical methods to evaluate the volume volume integral of *Vector Current Moment*. One of them uses Fourier Transform. To take the Fourier Transform, we need to convert surface current $\mathbf{J}(\theta, \phi)$ to its x , y and z components such as $\mathbf{J}(x, y, z) = \hat{x}J_x(x, y, z) + \hat{y}J_y(x, y, z) + \hat{z}J_z(x, y, z)$. In this case we increase the number of dimensions $2(\theta, \phi)$ to $3(x, y, z)$. Furthermore, we have already calculated surface current according to (θ, ϕ) angles in Figs. 6.3-6.6. To reduce these conversion operation and Fourier Transform, we have evaluated a surface integral for Vector Current Moment,

$$\vec{f}(\theta, \phi) = \oiint_{s(r=a)} ds' \vec{\mathbf{J}}(\vec{r}') e^{jk\hat{r} \cdot \vec{r}'}$$

where

$$ds' = a^2 \sin \theta' d\theta' d\phi'.$$

The surface integral is evaluated according to the parameters θ' and ϕ' . On the contrary, the θ and ϕ parameters denote the location of concerned electric field intensity. (' superscript denotes the source parameters).

$$\vec{f}(\theta, \phi) = \int_0^{2\pi} \int_0^\pi \vec{\mathbf{J}}(\vec{r}') e^{jk\hat{r} \cdot \vec{r}'} a^2 \sin \theta' d\theta' d\phi'$$

Actually,

$$\vec{\mathbf{J}}(\vec{r}') \Big|_{r=a} = \vec{\mathbf{J}}(\theta', \phi') = \hat{\theta}' J_\theta(\theta', \phi') + \hat{\phi}' J_\phi(\theta', \phi')$$

where

$$\begin{aligned} \hat{\theta}' &= \hat{x} \cos \theta' \cos \phi' + \hat{y} \cos \theta' \sin \phi' - \hat{z} \sin \theta' \\ \hat{\phi}' &= -\hat{x} \sin \phi' + \hat{y} \cos \phi' \end{aligned}$$

To derive the f_θ and f_ϕ components from in Eq. (6.6), we apply dot product to vector current moment with $\hat{\theta}$ and $\hat{\phi}$ vectors respectively. Then,

$$f_\theta = \hat{\theta} \cdot \vec{f}(\theta, \phi)$$

$$f_\phi = \hat{\phi} \cdot \vec{f}(\theta, \phi)$$

since

$$\vec{f}(\theta, \phi) = \int_0^{2\pi} \int_0^\pi [\hat{\theta}' J_\theta + \hat{\phi}' J_\phi] e^{jk\hat{r} \cdot \hat{r}'} a^2 \sin \theta' d\theta' d\phi'.$$

The result of dot product yields scalar f_θ and f_ϕ quantities.

$$f_\theta = \int_0^{2\pi} \int_0^\pi [\hat{\theta} \cdot \hat{\theta}' J_\theta + \hat{\theta} \cdot \hat{\phi}' J_\phi] e^{jk\hat{r} \cdot \hat{r}'} ds' \quad (6.7a)$$

$$f_\phi = \int_0^{2\pi} \int_0^\pi [\hat{\phi} \cdot \hat{\theta}' J_\theta + \hat{\phi} \cdot \hat{\phi}' J_\phi] e^{jk\hat{r} \cdot \hat{r}'} ds' \quad (6.7b)$$

where

$$\hat{\theta} \cdot \hat{\theta}' = \cos \theta \cos \phi \cos \theta' \cos \phi' + \cos \theta \sin \phi \cos \theta' \sin \phi' + \sin \theta \sin \theta'$$

$$\hat{\theta} \cdot \hat{\phi}' = -\cos \theta \cos \phi \sin \phi' + \cos \theta \sin \phi \cos \phi'$$

$$\hat{\phi} \cdot \hat{\theta}' = -\sin \phi \cos \theta' \cos \phi' + \cos \phi \cos \theta' \sin \phi'$$

$$\hat{\phi} \cdot \hat{\phi}' = \sin \phi \sin \phi' + \cos \phi \cos \phi'$$

also

$$\hat{r} \cdot \hat{r}' = a(\sin \theta \cos \phi \sin \theta' \cos \phi' + \sin \theta \sin \phi \sin \theta' \sin \phi' + \cos \theta' \cos \theta').$$

We have divided the surface of the sphere equally spaced intervals in Fig. 6.8. J_θ and J_ϕ currents at these intersection points, the far-zone electric field intensity can be determined by the integration of vector current moment. The integrations of the scalar f_θ and f_ϕ components are computed with *Composite Simpson's Double integral* algorithm [14] in appendix A.5.

The bistatic RCS values at different look angles can be calculated by the integration of the surface currents on the sphere. Actually, the integration of the surface currents gives us a flexibility to calculate the scattered electric field intensity at an arbitrary look angle. After evaluation electric fields, according to

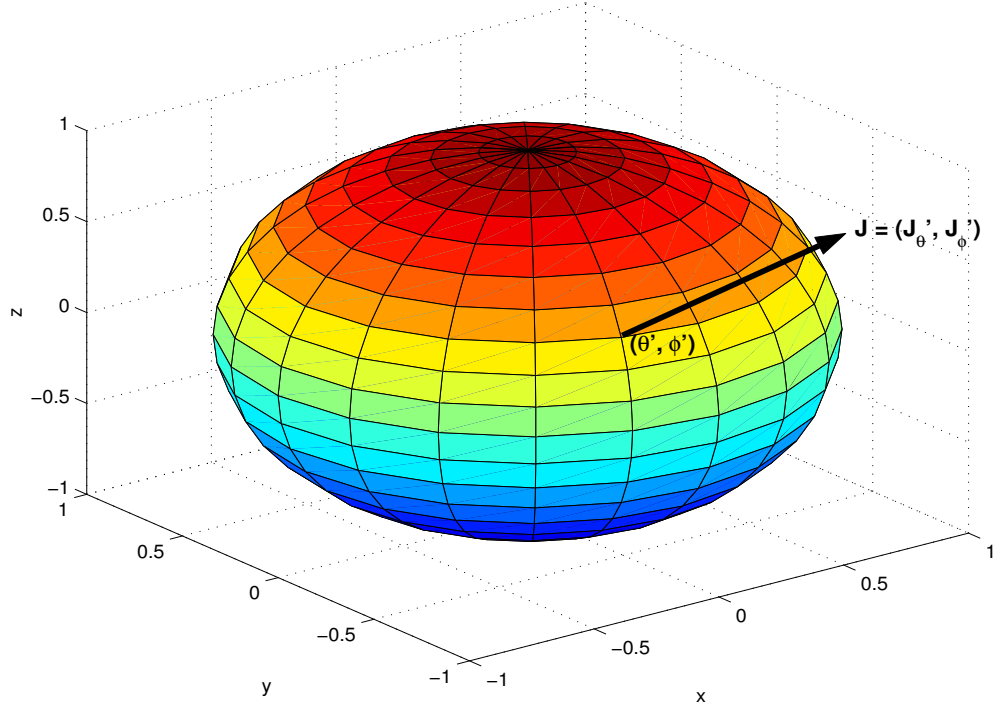


Figure 6.8: The location of the some intersection points on the PEC sphere

the equation (5.4), the bistatic RCS values can be calculated by using electric fields.

We have derived suitable integrants for the vector current moment of the PEC sphere. Before the integration of vector current moment, we have predicted big amount of surface current data with the help of Legendre-Basis algorithm. By using ($N = 157$) data samples, which are taken from the $\phi = 0^\circ$ cut between $0^\circ \leq \theta \leq 6^\circ$, $69^\circ \leq \theta \leq 180^\circ$, illustrated in the Fig. 6.9. The J_θ component of induced current is generated at 241×61 equally spaced points on the surface of the sphere. The resultant matrix $J_\theta = [j_\theta]_{241 \times 61}$ is constructed without using the analytical expression of J_θ in Eq. (2.36a).

Also, the same operation have been applied to the ϕ component of surface. The induced current components $J_\theta = [j_\theta]_{241 \times 61}$ and $J_\phi = [j_\phi]_{241 \times 61}$ are used in the integration of vector current moment with Composite Simpson's Double integral algorithm. After that, RCS values can be calculated at an arbitrary look angle easily. The efficiency of this algorithm comes from its flexibility.

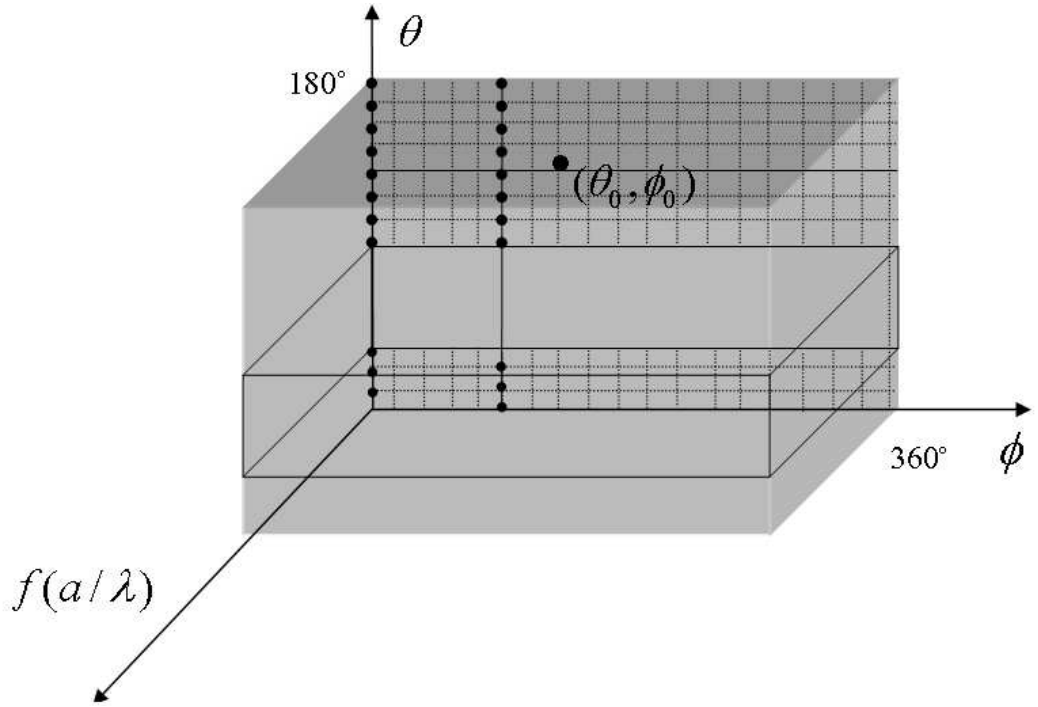


Figure 6.9: 3-D illustration of Current Estimation on the Surface of the sphere surface, θ, ϕ are taken as vertical and horizontal axis, respectively.

The calculation of RCS can be easily performed by using $J_\theta = [j_\theta]_{241 \times 61}$ and $J_\phi = [j_\phi]_{241 \times 61}$ the induced current matrices only substituting the concerned angle (θ_0, ϕ_0) in Eq. (6.7). After substitution of (θ_0, ϕ_0) as (π, π) , the results are presented in Fig. 6.10. Notice that error values at the bottom plot of this figure are very low. The results can be obtained lower than the 10^{-6} boundary until $a/\lambda = 2$. And if we increase the frequency (a/λ) until 4, we have have still obtained RCS estimations lower than the 10^{-4} boundary.

We can easily calculate the bistatic RCS values by using the same set of generated surface current matrices. In Fig. 6.11, RCS values are plotted when the look angle $(\theta = \pi/3, \phi = \pi/6)$. In the concerned figure (θ, ϕ) values are arbitrary two angles. We can choose θ between 0° and 180° , also ϕ between 0° and 360° intervals. Notice that the error results are still kept under the 10^{-4} value.

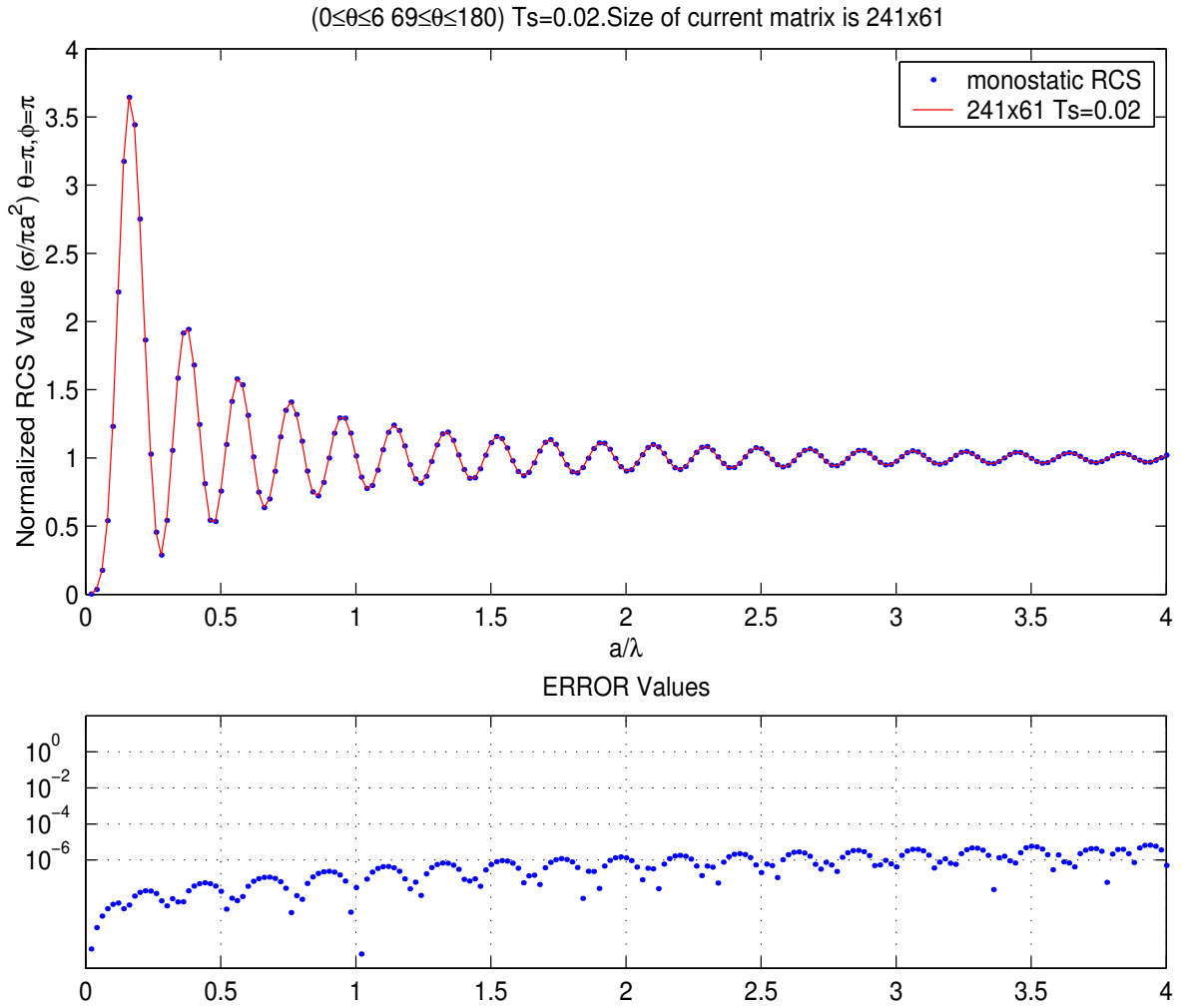


Figure 6.10: The monostatic ($\theta = \pi, \phi = \pi$) RCS calculations of the PEC sphere is illustrated. Before the integration of current values Legendre-basis algorithm is applied to J_θ and J_ϕ components of surface current by using the samples values which are taken ($0^\circ \leq \theta \leq 6^\circ, 69^\circ \leq \theta \leq 180^\circ$) at $\phi = 0$ and $\phi = 90^\circ$ cuts. The resolution of the plotted RCS figure is equal to 0.02.

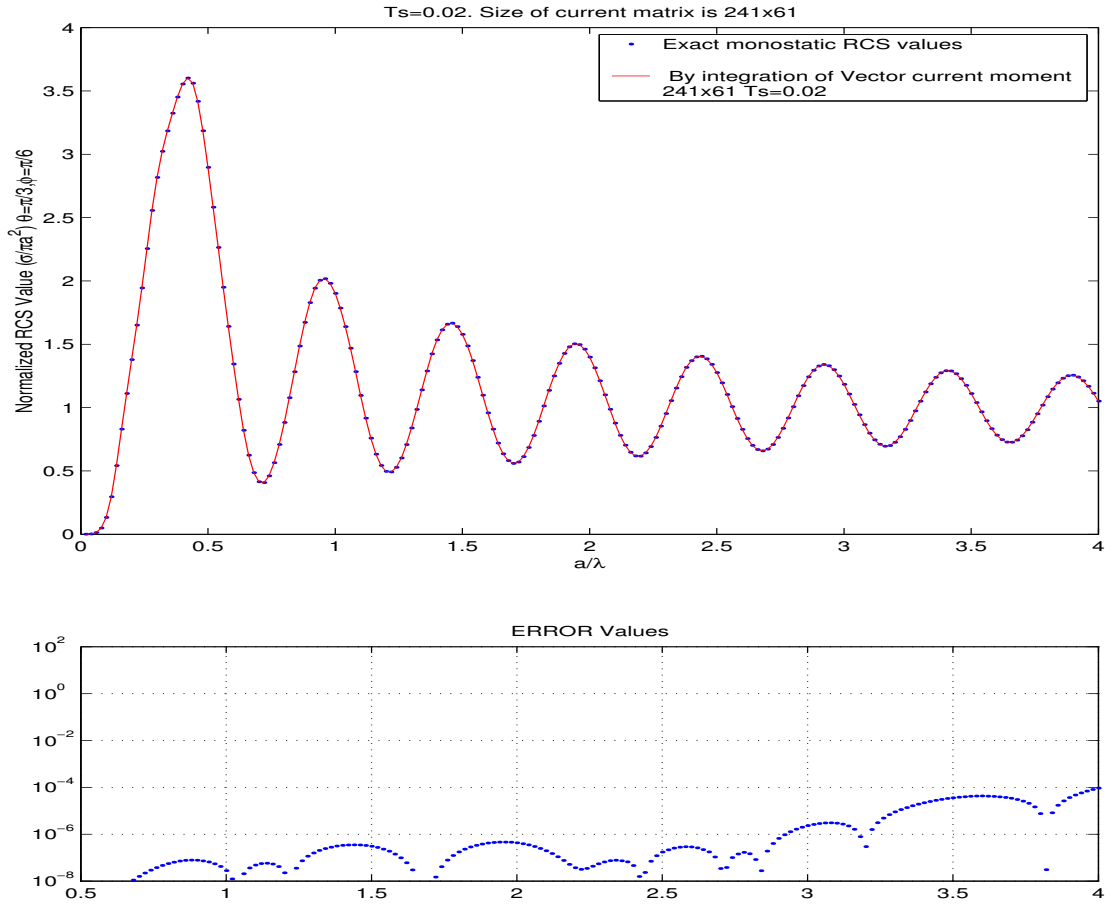


Figure 6.11: The bistatic RCS calculations when the look angle ($\theta = \pi/3, \phi = \pi/6$) is illustrated. Before the integration of current values Legendre-basis algorithm is applied to J_θ and J_ϕ components of surface current by using the samples values which are taken ($0^\circ \leq \theta \leq 6^\circ, 69^\circ \leq \theta \leq 180^\circ$) at $\phi = 0$ and $\phi = 90^\circ$ cuts. The resolution of the plotted RCS figure is equal to 0.02.

Chapter 7

Conclusions

In this thesis, Prony's and Matrix-Pencil methods are investigated to extract the parameters of exponential model. These methods are applied to a reference scatterer (such as the PEC sphere) to estimate frequency values. We can conclude that the Matrix-Pencil method is a quite efficient and accurate method with respect to the Prony's Method. The superiority of Matrix-Pencil method is demonstrated. Also the Matrix-Pencil method is modified to increase the accuracy in the frequency extrapolation.

According to this aim, the elimination of the growing exponentials and the generation of residues with new set of exponentials are demonstrated. These modifications yield accurate and stable estimations of the RCS in the frequency dimension. Furthermore, these modified algorithms can be reliable in the frequency extrapolation of induced currents. The results are presented at the end of chapter 4.

In chapter 5, a new algorithm is developed based on the theory of Matrix-Pencil method. This algorithm supports the estimations with two different scaled samples. That is why, we have called the Multi-Scale Matrix-Pencil method. This method can predict successfully the higher frequency RCS values with very modest sampled data and few exponentials. Also, the electric field components are

employed the Matrix-Pencil method in the RCS calculations. The effectiveness of the extrapolation technique has been presented with the monostatic RCS estimations at high-frequencies. Good agreement between the Multi-Scale Matrix-Pencil and the exact solutions over the wide frequency band is observed.

In chapter 6, we have proposed an efficient model to represent the induced currents on the surface of the PEC sphere. The coefficients of Legendre-Based functions are solved from the least squares problem. This model enables angular extrapolation of the induced currents all over the surface of the sphere from a few densely sampled data. Furthermore, calculation of bistatic RCS values by integrating the accurate set of induced current data is demonstrated.

Appendix A

Appendix

A.1 Singular Value Decomposition

The SVD is closely associated with the eigenvalue-eigenvector factorization of a symmetric matrix: $A = Q\Lambda Q^T$. There the eigenvalues are in the diagonal matrix Λ , and the eigenvector matrix Q is *orthogonal*: $Q^T Q = I$ because eigenvectors of a symmetric matrix can be chosen orthonormal. For most matrices that is not true, and for rectangular matrices it is ridiculous. But if we allow the Q on the left and the Q^T on the right to be *any two orthogonal matrices*—not necessarily transposes of each other—the factorization becomes possible again. Furthermore the diagonal (but rectangular) matrix in the middle can be made nonnegative. It will be denoted by Σ , and its positive entries (also called sigma) will be $\sigma_1, \dots, \sigma_r$. They are the *singular values* [4] of A . They fill the first r places on the main diagonal of Σ —and r is the rank of A .

The key to working with rectangular matrices is, almost always, to consider AA^T and $A^T A$.

Singular Value Decomposition: Any m by n matrix A can be factored into

$$A = Q_1 \Sigma Q_2^T = (\text{orthogonal})(\text{diagonal})(\text{orthogonal}).$$

The columns of Q_1 (m by n) are eigenvectors of AA^T , and the columns of Q_2 (m by n) are eigenvectors of $A^T A$. The r singular values on the diagonal of Σ (m by n) are the square roots of the non zero eigenvalues of both AA^T and $A^T A$. Suppose the singular value decomposition of A is $A = Q_1 \Sigma Q_2^T$. Then the pseudo-inverse of A is I . The singular values $\sigma_1, \dots, \sigma_r$, are on the diagonal of Σ (m by n), and the reciprocals $1/\sigma_1, \dots, 1/\sigma_r$ are on the diagonal of Σ^+ (m by n). The pseudo-inverse of A^+ is $A^{++} = A$.

A.2 Legendre Polynomials

There are many bad ways to evaluate associated Legendre polynomials numerically [10]. For example, there are explicit expressions, such as

$$P_l^m(x) = \frac{(-1)^m(l+m)!}{2^m m!(l-m)!} (1-x^2)^{m/2} \left[1 - \frac{(l-m)(m+l+1)}{1!(m+1)} \left(\frac{1-x}{2}\right) + \frac{(l-m)(l-m-1)(m+l+1)(m+l+2)}{2!(m+1)(m+2)} \left(\frac{1-x}{2}\right)^2 - \dots \right] \quad (\text{A.1})$$

The recurrence relations [10] is used for Legendre Polynomials

$$(l-m)P_l^m = x(2l-1)P_{l-1}^m - (l+m-1)P_{l-2}^m \quad (\text{A.2})$$

It is useful because there is a closed-form expression for the starting value,

$$P_m^m = (-1)^m (2m-1)!! (1-x^2)^{m/2} \quad (\text{A.3})$$

(The notation $n!!$ denotes the product of all odd integers less than or equal to n .) Using Eq. (A.2) with $l = m+1$, and setting $P_{m-1}^m = 0$, we find

$$P_{m+1}^m = x(2m+1)P_m^m \quad (\text{A.4})$$

Equation (A.2) can be handled by following steps *i* – *iii*.

- i.* $P_m^m(x)$ is evaluated from Eq. (A.3)
- ii.* $P_{m+1}^m(x)$ is found by using Eq. (A.4)
- iii.* By using $P_{m+1}^m(x), P_m^m(x)$, the values $P_{m+2}^m(x), \dots, P_{l-1}^m(x), P_l^m(x)$ are calculated one by one from Eq. (A.2).

We have two form of Legendre polynomials used in the calculation of current \mathbf{J} and electric field \mathbf{E}^s values.

$$\sin \theta P_n^1(\cos \theta), \frac{P_n^1(\cos \theta)}{\sin \theta}$$

The associated Legendre polynomials $P_n^m(x)$ of the first kind related to the Legendre functions $P_n(x)$.

$$P_n^m(x) = (-1)^m (1-x^2)^{m/2} \frac{\partial^m P_n(x)}{\partial x^m} \quad (\text{A.5})$$

from Eq. (A.5),

$$\begin{aligned} \frac{P_n^1(\cos \theta)}{\sin \theta} &= \frac{\frac{d}{d\theta} P_n(\cos \theta)}{\sin \theta} \\ &= - \frac{dP_n(\cos \theta)}{d(\cos \theta)} \Big|_{x=\cos \theta} = - \frac{dP_n(x)}{dx} \end{aligned}$$

The Legendre polynomials can be also obtained more conveniently by using *Rodrigue's formula*,

$$P_n^m(x) = \frac{1}{2^n n!} \frac{d^n}{dx^n} (x^2 - 1)^n \quad (\text{A.6})$$

by using *Rodrigue's formula* (A.6)

$$\frac{P_n^1(\cos \theta)}{\sin \theta} \Big|_{\theta=\pi} = (-1)^n \frac{n(n+1)}{2}$$

when $\theta = \pi$ and

$$\frac{P_n^1(\cos \theta)}{\sin \theta} \Big|_{\theta=0} = - \frac{n(n+1)}{2}$$

when $\theta = 0$. Also $\sin \theta P_n^1(\cos \theta)$ can be written in terms of

$$\frac{P_n^1(\cos \theta)}{\sin \theta}$$

to reduce the computational cost

$$\begin{aligned} \sin \theta P_n^1(\cos \theta) &= \sin \theta \frac{dP_n^1(\cos \theta)}{d \cos \theta} = - \frac{dP_n^1(\cos \theta)}{d\theta} \\ &= - \frac{d}{d\theta} \left(\frac{d}{d\theta} P_n^1(\cos \theta) \right) \end{aligned}$$

by using *Chain Rule* $x = \cos \theta$

$$\begin{aligned} &= - \frac{d}{d\theta} \left[\frac{dx}{d\theta} P_n'(x) \right] \\ &= - \left[\frac{d^2 x}{d\theta^2} P_n'(x) + \left(\frac{dx}{d\theta} \right)^2 P_n''(x) \right] \\ \sin \theta P_n^1(\cos \theta) &= - \left[\cos \theta \left(\frac{P_n^1(\cos \theta)}{\sin \theta} \right) + P_n^2(\cos \theta) \right]. \end{aligned}$$

A.3 Derivative Operator of Spherical Bessel and Hankel Functions

The set of spherical Bessel and Hankel functions which appear in the solutions of electromagnetic problems is that denoted by \hat{Z}_n , where \hat{Z}_n can be used to represent \hat{J}_n , $\hat{H}_n^{(1)}$ or $\hat{H}_n^{(2)}$. The derivative operator of these functions are as follows,

$$\hat{Z}'_n(x) = \frac{d}{dx} \hat{Z}_n(x) = \left(\frac{\pi}{2}\right)^{1/2} \left[\frac{-n}{\sqrt{x}} Z_{n+1/2}(x) + \sqrt{x} Z_{n-1/2}(x) \right]. \quad (\text{A.7})$$

A.4 Projections and Least Square Solution

If there are more equations than unknowns and, in general, no solution exist. In this case, the equations are *inconsistent* and the solutions said to be *overdetermined*. The geometry of this problem is illustrated in Fig. A.1 for the case of three equations in two unknowns. Since an arbitrary vector \mathbf{b} cannot be represented in terms of a linear combination of the columns of $\mathbf{A} = [a_i]_{n \times m}$ as given in Eq. (A.8), the goal is to find coefficients x_i that produce the best approximation to \mathbf{b} ,

$$\mathbf{A}x = \mathbf{b} \quad (\text{A.8})$$

$$\hat{\mathbf{b}} = \sum_{i=1}^m x_i \mathbf{a}_i \quad (\text{A.9})$$

This approach that is commonly used in this situation is to find *the least squares solution*, i.e., the vector \mathbf{x} that minimizes the norm of the error

$$\|\mathbf{e}\|^2 = \|\mathbf{b} - \mathbf{A}x\| \quad (\text{A.10})$$

As illustrated in Fig. A.1, the least square solution has the property that the error,

$$\mathbf{e} = \mathbf{b} - \mathbf{A}x$$

is orthogonal to each of the vectors that are used in the approximation for \mathbf{b} , i.e., the column vectors of \mathbf{A} . This orthogonality implies that

$$\mathbf{A}^H \mathbf{e} = 0 \quad (\text{A.11})$$

or,

$$\mathbf{A}^H \mathbf{A}x = \mathbf{A}^H \mathbf{b}$$

which are known as the normal equations. If the columns of \mathbf{A} are linearly independent (\mathbf{A} has a full rank), then the matrix $\mathbf{A}^H \mathbf{A}$ is invertible and the least squares solution is

$$\mathbf{x}_0 = (\mathbf{A}^H \mathbf{A})^{-1} \mathbf{A}^H \mathbf{b}$$

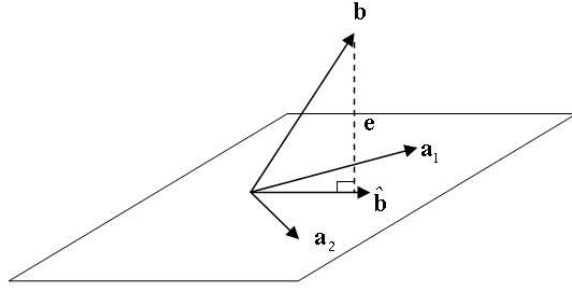


Figure A.1: Geometrical illustration of the least squares solution to an overdetermined set of linear equations. the best approximation to \mathbf{b} is formed when the error \mathbf{e} is orthogonal to to the vectors \mathbf{a}_1 and \mathbf{a}_2

or,

$$\mathbf{x}_0 = \mathbf{A}^+ \mathbf{b}$$

where the matrix

$$\mathbf{A}^+ = (\mathbf{A}^H \mathbf{A})^{-1} \mathbf{A}^H$$

is the pseudo-inverse of the matrix \mathbf{A} for the overdetermined problem. Furthermore, the best approximation $\hat{\mathbf{b}}$ to \mathbf{b} is given by the projection of the vector \mathbf{b} on to the subspace spanned by the vectors \mathbf{a}_i ,

$$\hat{\mathbf{b}} = \mathbf{A} \mathbf{x}_0 = \mathbf{A} (\mathbf{A}^H \mathbf{A})^{-1} \mathbf{A}^H \mathbf{b}$$

or

$$\hat{\mathbf{b}} = \mathbf{P}_A \mathbf{b}$$

where

$$\mathbf{P}_A = \mathbf{A} (\mathbf{A}^H \mathbf{A})^{-1} \mathbf{A}^H$$

is called the projection matrix. Finally, expanding the square in Eq. (A.10) and using the *orthogonality condition* given in Eq. (A.11) it follows that the minimum least squares error is

$$\min \|\mathbf{e}\|^2 = \mathbf{b}^H \mathbf{e} = \mathbf{b}^H \mathbf{b} - \mathbf{b}^H \mathbf{A} \mathbf{x}_0.$$

A.5 Composite Simpson's Double Integral

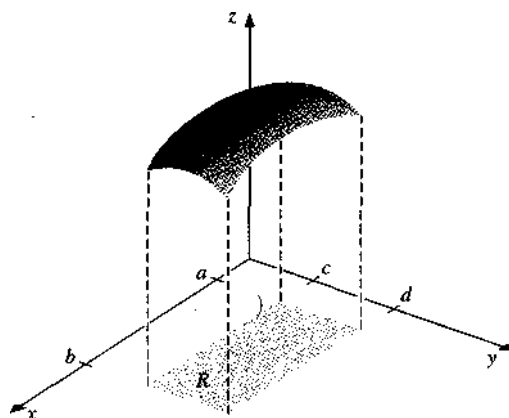
Consider the double integral,

$$\iint_R f(x, y) dA =$$

where R is a rectangular region in the plane;

$$R = \{(x, y) | a \leq x \leq b, c \leq y \leq d\}$$

for some constants a, b, c , and d . (See Figure A.5) To illustrate the approximation technique, we employ the Composite Simpson's rule, although any other composite formula could be used in its place. To apply the Composite Simp-



son's rule, we divide the region R by partitioning both $[a, b]$ and $[c, d]$ into an even number of subintervals. To simplify the notation we choose integers n and m and partition $[a, b]$ and $[c, d]$ with the evenly spaced mesh points x_0, x_1, \dots, x_{2n} and y_0, y_1, \dots, y_{2m} , respectively. These subdivisions determine step sizes $h = (b - a)/2n$ and $k = (d - c)/2m$. Writing the double integral as the iterated integral,

$$\iint_R f(x, y) dA = \int_a^b \left(\int_c^d f(x, y) dy \right) dx$$

we first use the Composite Simpson's rule to evaluate

$$\int_c^d f(x, y) dy,$$

treating x as a constant. Let $y_j = c + jk$ for each $j = 0, 1, \dots, 2m$. Then

$$\int_c^d f(x, y) dy = \frac{k}{3} \left[f(x, y_0) + 2 \sum_{j=1}^{m-1} f(x, y_{2j}) + 4 \sum_{j=1}^m f(x, y_{2j-1}) + f(x, y_{2m}) \right] - \frac{(d-c)k^4}{180} \frac{\partial^4 f(x, \mu)}{\partial y^4}$$

for some μ , in (c, d) . Thus,

$$\begin{aligned} \int_a^b \int_c^d f(x, y) dy dx &= \frac{k}{3} \left[\int_a^b f(x, y_0) dx + 2 \sum_{j=1}^{m-1} \int_a^b f(x, y_{2j}) dx \right. \\ &\quad \left. + 4 \sum_{j=1}^m \int_a^b f(x, y_{2j-1}) dx + \int_a^b f(x, y_{2m}) dx \right] \\ &\quad - \frac{(d-c)k^4}{180} \int_a^b \frac{\partial^4 f(x, \mu)}{\partial y^4} dx. \end{aligned}$$

The Composite Simpson's rule is now employed on the integrals in this equation.

Let $x = a + ih$ for each $i = 0, 1, \dots, 2n$. Then for each; $j = 0, 1, \dots, 2m$, we have

$$\int_a^b f(x, y_j) dx = \frac{h}{3} \left[f(x_0, y_j) + 2 \sum_{i=1}^{n-1} f(x_{2i}, y_j) + 4 \sum_{i=1}^n f(x_{2i-1}, y_j) + f(x_{2n}, y_j) \right] - \frac{(b-a)h^4}{180} \frac{\partial^4 f(\xi_i, y_j)}{\partial x^4}$$

$$\begin{aligned} \int_a^b \int_c^d f(x, y) dy dx &\approx \frac{hk}{9} \left\{ \left[f(x_0, y_0) + 2 \sum_{i=1}^{n-1} f(x_{2i}, y_0) + 4 \sum_{i=1}^n f(x_{2i-1}, y_0) + f(x_{2n}, y_0) \right] \right. \\ &\quad + 2 \left[\sum_{j=1}^m f(x_0, y_{2j}) + 2 \sum_{j=1}^{m-1} \sum_{i=1}^{n-1} f(x_{2i}, y_{2j}) \right. \\ &\quad \left. \left. + 4 \sum_{j=1}^{m-1} \sum_{i=1}^n f(x_{2i-1}, y_{2j}) + \sum_{j=1}^{m-1} f(x_{2n}, y_{2j}) \right] \right. \\ &\quad + 4 \left[\sum_{j=1}^m f(x_0, y_{2j-1}) + 2 \sum_{j=1}^m \sum_{i=1}^{n-1} f(x_{2i}, y_{2j-1}) \right. \\ &\quad \left. \left. + 4 \sum_{j=1}^m \sum_{i=1}^n f(x_{2i-1}, y_{2j-1}) + \sum_{j=1}^m f(x_{2n}, y_{2j-1}) \right] \right. \\ &\quad + \left[f(x_0, y_{2m}) + 2 \sum_{i=1}^{n-1} f(x_{2i}, y_{2m}) \right. \\ &\quad \left. \left. + \sum_{i=1}^n f(x_{2i-1}, y_{2m}) + \text{left.} f(x_{2n}, y_{2m}) \right] \right\} \end{aligned}$$

The error term E is given by

$$E = \frac{k(b-a)h^4}{540} \left[\frac{\partial^4 f(\xi_0, y_0)}{\partial x^4} + 2 \sum_{j=1}^{m-1} \frac{\partial^4 f(\xi_{2j}, y_{2j})}{\partial x^4} + 4 \sum_{j=1}^m \frac{\partial^4 f(\xi_{2j-1}, y_{2j-1})}{\partial x^4} + \frac{\partial^4 f(\xi_{2m}, y_{2m})}{\partial x^4} \right] + \frac{(d-c)k^4}{180} \int_a^b \frac{\partial^4 f(x, \mu)}{\partial y^4} dx.$$

Bibliography

- [1] Balanis C.A., *Advanced Engineering Electromagnetics*, John Wiley & Sons, New York, 1989.
- [2] Abramowitz, M., and Stegun, *Handbook of Mathematical Functions* Dover Publications, New York, 1965)
- [3] Sarkar, T.K., and Hua Y., "Generalized Pencil-of-Function Method for Extracting Poles of an EM System from Its Transient Response," *IEEE Antennas and Propagation Magazine*, Vol. 37, No.2, pp. 2, February 1989.
- [4] Strang G., 1986, *Linear Algebra and its Applications*, Harcourt Brace Company Int. Ed. New York.
- [5] Marple S. Lawrence, *Digital Spectral Analysis with Applications*, Prentice-Hall, New Jersey, 1987
- [6] Sarkar, T.K., and Pereira O., "Using the Matrix Pencil Method to Estimate the Parameters of a Sum of Complex Exponentials," *IEEE Antennas and Propagation Magazine*, Vol. 37, No.1, pp. 48-55, February 1995.
- [7] Ling, H., and Wang Y., "Radar Signature Prediction Using Moment Method Codes via a Frequency Extrapolation Technique," *IEEE Transaction on Antennas and Propagation*, Vol. 47, No.6, pp. 1008-1015, June 1999.
- [8] Mittra, R., and Altman Z., "Combining an Extrapolation Technique with the Method of Moments for solving Large Scattering Problems Involving

- Bodies of Revolution,” *IEEE Transaction on Antennas and Propagation*, Vol. 44, No.4, pp. 548-553, April 1996.
- [9] Miller, E., “Model-Based Parameter Estimation in Electromagnetics,” *IEEE Antennas and Propagation Magazine*, Vol. 40, No.1, pp. 42-52, February 1998.
- [10] Press, William H. *Numerical Recipes in Fortran 77 and 90:: the art of scientific computing* Cambridge University Press, Cambridge, 1996
- [11] Bowman, J. J. *Electromagnetic and acoustic scattering by simple shapes* Hemisphere Pub. Corp., New York, 1987
- [12] Hayes, M. H. *Statistical Digital Signal Processing and Modeling* John Wiley & Sons, New York, 1996
- [13] Harrington, Roger F. *Time-harmonic electromagnetic fields* McGraw-Hill, New York, 1961
- [14] Burden, Richard L. *Numerical Analysis* PWS Publishing Company, Boston, 1993